



**American Science  
and Engineering, Inc.**

955 Massachusetts Avenue  
Cambridge, Massachusetts 02139  
(617) 868-1600

31 OCTOBER 1973

ASE-3394

FINAL REPORT

CONTRACT NASW-2346

**CONTINUING DATA ANALYSIS  
OF THE AS&E  
GRAZING INCIDENCE  
X-RAY TELESCOPE EXPERIMENT  
ON THE OSO-4 SATELLITE**

REPORT PERIOD: 14 JANUARY 1972 - 31 OCTOBER 1973

PREPARED BY:

G. VAIANA R. HAGGERTY S. KAHLER  
A. KRIEGER M. LANDINI A. TIMOTHY  
D. WEBB

PREPARED FOR:

NATIONAL AERONAUTICS  
AND SPACE ADMINISTRATION  
WASHINGTON, D.C. 20546

(NASA-CR-139685) CONTINUING DATA ANALYSIS  
OF THE AS/E GRAZING INCIDENCE X-RAY  
TELESCOPE EXPERIMENT ON THE OSO-4  
(American Science and Engineering, Inc.)  
171 p HC \$11.75  
CSCI 03B G3/29 15882  
Unclas  
N74-33250

ASE-3394

FINAL REPORT

CONTRACT NASW-2346

CONTINUING DATA ANALYSIS OF  
THE AS&E GRAZING INCIDENCE X-RAY  
TELESCOPE EXPERIMENT ON THE OSO-4  
SATELLITE

Prepared by:

G. Vaiana, R. Haggerty, S. Kahler, A. Krieger  
M. Landini, A. Timothy, D. Webb  
American Science and Engineering  
955 Massachusetts Avenue  
Cambridge, Massachusetts 02139

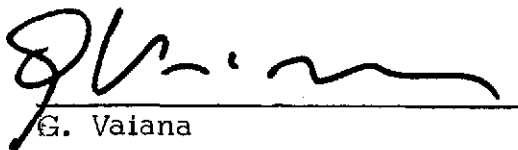
Prepared for:

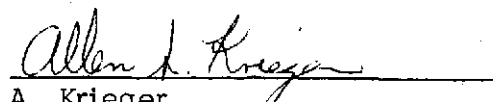
National Aeronautics and Space Administration  
Washington, D.C. 20546

31 October 1973

Report Period: 14 January 1972 - 31 October 1973

Approved:

  
G. Vaiana  
Director - Research  
Principal Investigator

  
A. Krieger  
Project Scientist

## Contents

	<u>Page</u>
1.0 INTRODUCTION	1-1
2.0 FORMULATION OF X-RAY ACTIVE REGION MODELS AND COMPARISON WITH EXPERIMENTAL VALUES	2-1
3.0 ATLAS OF SOLAR X-RAY PHOTOGRAPHS	3-1
4.0 CORRELATION OF X-RAY OBSERVATIONS WITH THE SOLAR WIND	4-1

## References

- Appendix A: Vaiana, G. S., Krieger, A. S. and Timothy A. F.:  
1973, "Identification and Analysis of Structures in the Corona  
From X-ray Photography" To be published in Solar Physics
- Appendix B: Vaiana, G. S., Haggerty, R., Krieger, A. S., Van Speybroeck, L.,  
and Webb, D.: 1973, "An Atlas of Solar X-ray Photographs"  
AS&E Technical Report in Preparation.
- Appendix C: Krieger, A. S., Timothy, A. F. and Roelof, E. C.: 1973, "A  
Coronal Hole and Its Identification as the Source of a High  
Velocity Solar Wind Stream" Solar Physics, 29, 505.

## 1.0 INTRODUCTION

This document is the Final Report for NASA Contract NASW-2346 whose title is "Continued Analysis of Data from the AS&E Grazing Incidence X-ray Telescope on the OSO-4 Satellite". The original period of performance on the contract was from 14 January to 31 December 1972. However, the period of performance was extended to 31 October 1973. Including the performance period extension, five Quarterly Reports on the contract were required. Four have been submitted: ASE Reports Nos. 2959, 3032, 3116 and 3221. Information pertinent to work done during the period of performance for the fifth Quarterly Report from 1 January to 31 March 1973 is included in this report.

The analysis performed under this contract included correcting and extending the calculation of the theoretical solar X-ray spectrum produced during earlier OSO-4 analysis contracts, formulating models of active regions, and comparing these models with observed quantities from our sounding rocket photographs and from the observed OSO-4 X-ray region time histories.

The solar X-ray astronomy program at AS&E is a general effort to study the solar corona with high resolution telescopes, using the observing platforms provided by rockets and satellites. The OSO-4 X-ray telescope experiment provided our first long-term evolutionary studies of the solar X-ray corona, an ability which is unique to satellite observations. The experience and knowledge gained from OSO-4 and our continuing sounding rocket program has provided a basis for AS&E's successful X-ray spectrographic telescope experiment now



operating aboard Skylab.

A substantial effort continues at AS&E to develop data reduction and analysis techniques that will enable both morphological information and quantitative density and temperature measurements to be extracted from the OSO-4 spectroheliograms and our X-ray photographs. Details of this program have been discussed in the Quarterly Reports on this contract, in the Final Report on Contract NASW-2070 (for the OSO-4 experiment) and in the Final Report on Contract NASW-2240 (for the sounding rocket analysis).

Much of the work on Contract NASW-2346 has been a continuation of the development of these reduction and analysis techniques. This work included the detailed testing and correction of the theoretical solar X-ray spectrum model of Tucker and Koren (1971), refinement of computer programs used in aligning and overlaying our X-ray images with those taken at other wavelengths, and detailed analysis of the deconvolution of our telescopes' point response functions.

As a result of the development of the above techniques, the continuing influx of new X-ray data and developing theories on coronal structures, studies under this contract were initiated on various subjects concerning the development and maintenance of the structures seen in our X-ray photographs and the OSO-4 data. These included X-ray flare studies as follows: 1) collecting and comparing flare data in the literature with our X-ray data; 2) detailed analysis of the flare seen on our 8 June 1968 rocket images; 3) determination of the OSO-4 detector response to known flare events; and 4) a study of sympathetic flares (flares triggered by events in interconnected solar regions) on our 7 March 1970 rocket images and the OSO-4 data.

Also included were studies of comparisons of prominences and filaments as seen in X-rays. These are coronal features which are best seen in longer wavelengths, especially H $\alpha$ . Coronal holes, areas of low coronal density, were also studied in detail, especially on our 24 November 1970 rocket images.

The study of the extensive coronal hole on 24 November led to correlation of the position of the hole with the source of a high velocity stream in the solar wind. Two papers were presented at scientific meetings on this subject and a paper was published in Solar Physics. This work is summarized in Section 4 and appears in Appendix C of this report.

During this period work was performed on the formulation of models of active regions as evidenced in our X-ray data. Parameters of these models are then compared with observed quantities to check their validity and then to refine them. A paper describing this work has been accepted for publication in Solar Physics and appears as Appendix A. It is discussed in Section 2.

Finally, work under this contract included production of an atlas of all significant X-ray photographs from the five successful rocket flights of our original rocket payload. The photographs and explanatory tables for each flight that will appear in the atlas are in Appendix B. A discussion of the atlas is contained in Section 3.

## 2.0 FORMULATION OF X-RAY ACTIVE REGION MODELS AND COMPARISON WITH EXPERIMENTAL VALUES

Until the inception of this contract, most theoretical work on the solar X-ray corona had involved details of the quiet corona. Only very simple models had been applied to active regions and flares, and these failed to predict details of the distribution of temperature, density and the controlling magnetic field.

Initial work on active region modeling at AS&E involved using scale heights of active regions measured from our photographs to derive the temperature distribution within the region. This range of temperatures was then used with the Tucker-Koren model spectrum to yield a set of emission measures and, hence, the density distribution. Early work during this contract was directed towards the study of the complex, bipolar magnetic field structure constraining the plasma within active regions and interconnecting active regions. Production of detailed mathematical models to describe this structure was started.

The original intent of the work to be done on this contract was to extend and correct the Tucker-Koren model, develop more detailed models of coronal active region structure and verify them through comparison with the rocket photographic results and finally to use these models to interpret the OSO-4 X-ray data. The intent was modified somewhat as we developed the analysis techniques and learned more about the solar corona.

Consequently, this work has evolved in two main phases. The first phase involved an in-depth study of solar X-ray coronal models involving both AS&E personnel and visiting collaborators. The knowledge gained in this work was applied to correcting and extending the Tucker-Koren model. Concurrently

analysis techniques were being developed and applied to the OSO-4 and rocket results as outlined in the Introduction.

During the second phase, our understanding of modeling techniques is being applied to the detailed development of active region models.

The first phase of this work has been completed. Much work on the second phase has been accomplished during the period of this contract, but it is evident that such a study is really on-going and cannot be completed within the lifetime of a single contract. The results of the work to date are contained in a paper that has been accepted for publication in Solar Physics. It is entitled "Identification and Analysis of Structures in the Corona from X-ray Photography" by G. Vaiana, A. Krieger and A. Timothy, and appears as Appendix A of this report. Further results on the development of models of coronal active region structures will be presented in a paper which is in preparation.

### 3.0 ATLAS OF SOLAR X-RAY PHOTOGRAPHS

Near the beginning of this contract we made an evaluation of the availability of AS&E's solar X-ray data collected over the last several years. At that time work on the data reduction of the OSO-4 X-ray experiment had been completed and the prime data delivered to the National Space Science Data Center (NSSDC), where it is available for use by interested scientists (see Krieger, et.al., 1971). The results of our data analysis under Contract NASW-2070 on OSO-4 were published in a scientific paper (Krieger, et.al., 1972).

We felt that now that the OSO-4 data were available to the scientific community, it would be appropriate to reproduce the data from our sounding rocket program in a form easily available to interested scientists. Therefore, it was decided that an atlas of all the important X-ray photographs from the five successful rocket flights of our original payload would be produced in-house. This atlas contains high quality, half-tone reproductions of the photographs along with a descriptive text giving details of the detector components and of the most significant features on the photographs. Sufficient details are available to permit a scientist to use the photographs.

The atlas will be in the form of an AS&E report and will be made available on a request basis to solar physicists.

Appendix B contains copies of the photographs to be used in the atlas along with descriptive tables for each flight.

#### 4.0 CORRELATION OF X-RAY OBSERVATIONS WITH THE SOLAR WIND

Appendix C contains a paper entitled "A Coronal Hole and Its Identification as the Source of a High Velocity Solar Wind Stream" by A. Krieger, A. Timothy and E. Roelof, which was published in Solar Physics (Krieger, et.al., 1973). Work on this paper was supported in part by this contract.

This paper developed as a result of comparing solar X-ray structures from our photographs with solar wind high velocity streams. Theoretical computations have indicated that areas characterized by radial magnetic fields on the sun are likely to be the sources of solar wind high velocity streams. Comparisons were made between the X-ray rocket images of 24 November 1970 and Pioneer and Vela solar wind data for that date, and it was concluded that the large coronal hole seen on that date was probably the source of a high velocity stream seen in the solar wind data.

## REFERENCES

Davis, Barrett, Compagno, Haggerty, Krieger, Leiblein, Manko, Perrenod, Sherman, Timothy, Ting and Webb: 1972, Final Report for High Resolution Study of the Solar X-ray Corona from Aerobee Rocket 4.285CS: Design and Construction of an Aerobee 170 Payload, ASE-3000.

Krieger, A., Tucker, W., Vaiana, G., and Webb, D.: 1971, Final Report for Final Data Reduction and Analysis of the AS&E OSO-IV Grazing Incidence X-ray Telescope Experiment, ASE-2736.

Krieger, A., Paolini, F., Vaiana, G. and Webb, D.: 1972, Sol. Phys., 22, 150.

Krieger, A.S., Timothy, A.F. and Roelof, E.C.: 1973, Sol. Phys., 29, 505.

Tucker, W. and Koren, M.: 1971, Ap. J., 168, 283.

Vaiana, G.S., Haggerty, R., Krieger, A.S., Van Speybroeck, L. and Webb, D.: 1973, An Atlas of Solar X-ray Photographs, AS&E Technical Report; in preparation.

Vaiana, G.S., Krieger, A.S. and Timothy, A.F.: 1973 To be published in Solar Physics.

## APPENDIX A



ASE-3327

IDENTIFICATION AND ANALYSIS OF STRUCTURES IN THE CORONA  
FROM X-RAY PHOTOGRAPHY

G.S. VAIANA, A.S. KRIEGER, A.F. TIMOTHY  
American Science and Engineering, Cambridge, Massachusetts U.S.A.

To be published in SOLAR PHYSICS

Received: July 21, 1973

# IDENTIFICATION AND ANALYSIS OF STRUCTURES IN THE CORONA FROM X-RAY PHOTOGRAPHY\*

G.S. VAIANA, A.S. KRIEGER and A.F. TIMOTHY  
American Science and Engineering, Cambridge, Mass. U.S.A.

Received: July 21, 1973

## Abstract

This paper summarizes the results of a program of rocket observations of the solar corona with grazing incidence X-ray telescopes. A series of five flights of a Kanigen-surfaced telescope with a few arc seconds resolution, together with the first flight of a newer telescope have resulted in the identification of six classes of coronal structures observable in the X-ray photographs. These are: active regions, active region interconnections, large loop structures associated with unipolar magnetic regions, coronal holes, coronal bright points, and the structures surrounding filament cavities. Two solar flares have been observed. The methods involved in deriving coronal temperature and density information from X-ray photographs are described and the analysis of a bright active region (McMath plage 11035) observed at the west limb on November 24, 1970 is presented as an example of these techniques.

---

\*This paper originated in an invited talk presented by one of us (G.V.) at the COSPAR Symposium on High Resolution Astronomical Observations from Space, Seattle, Washington, June 29, 1971. In addition, it includes material presented at the three NASA OSO workshops, as well as more recent work.

## 1. INTRODUCTION

The solar corona has a temperature in excess of one million degrees. Radiation from such a plasma consists predominantly of resonance radiation from highly ionized elements and of continuum radiation produced by free-free processes and recombination processes. Since the resonance lines of hydrogen-like and helium-like ions from carbon and all heavier elements occur below  $60 \text{ \AA}$  the characteristic radiation from the corona lies in the soft X-ray region of the spectrum. Thus, the corona may be studied at these wavelengths without risk of interference by background radiation from the underlying chromosphere and photosphere. Measurements of solar soft X-ray emission must however be made from rockets or satellites in order to avoid absorption of the radiation by the earth's atmosphere.

During the past decade the Solar Physics Group at American Science and Engineering has carried out a program of development of soft X-ray imaging techniques in order to study the structure of the solar corona. Early observations (pre 1968), carried out by our group (Giacconi et. al. , 1965; Reidy et. al. , 1968) were restricted to approximately one arc minute in spatial resolution due both to limitations in grazing incidence telescope technology and to the rocket fine pointing control systems available at that time. Even with such coarse resolution, however, it was possible to distinguish active regions, to observe the limb brightening of the general corona and to detect faint traces of large scale structures on the disk (see Figures 1a and b). In 1968, however, a breakthrough occurred with the development, at AS&E, of a grazing incidence telescope with resolution capability in the arc second range. Simultaneously, NASA produced a solar fine pointing control system for rocket observations with a peak to peak jitter of the order of two arc seconds. Thus, the structure of the corona could

finally be observed and the physical conditions existing within the observed features could be meaningfully determined.

Since that time a further six successful, high resolution, X-ray telescope sounding rocket payloads have been flown by our group (Figure 1c-h), each involving additional improvements in technique. Individual experiments were designed with specific observations in mind, such as the study of active region structure, flare dynamics, or the determination of the morphology of the quiet coronal features. However, in every case some new feature has been observed which was not anticipated. For example, the existence of X-ray emitting large scale coronal structures was detected in the June 8, 1968 flare observation (Vaiana et. al., 1968). Bright points, active region interconnections and structures associated with large scale unipolar magnetic fields were seen first in the April 8, 1969 flight (Vaiana et. al., 1970) and more clearly still in the 1970 flights (Krieger, et. al., 1971a). Filament cavities (Timothy et. al., 1972) were spectacularly evident in the two 1970 flights which also gave the AS&E group its first views of coronal holes (Krieger et. al., 1972; Krieger et. al., 1973). Finally, in the most recent rocket flight, with a new low scatter, quartz mirror (Davis et. al., 1973a) coronal loops have been seen surrounding a developing active region (Davis et. al., 1973b). Table 1 lists the rocket flights which have been conducted. The complete results of the five flights between June 1968 and November 1970 are now available in the form of an atlas of photographs (Vaiana et. al., 1973).

As may be seen from Figure 1, the image quality of solar X-ray photographs has improved very rapidly over the past ten years. It would therefore seem appropriate to pause and review the experimental techniques employed and the characteristics of the coronal features observed before moving on to the higher resolution studies planned for the new telescope and the time dependent observations which are now possible with the launch of the AS&E X-ray telescope on Skylab.

## 2. INSTRUMENTATION

The earliest images in X-ray astronomy were obtained with pin-hole cameras. The first historical photograph was obtained by the NRL group in 1960 (Blake et. al. , 1963). This photograph ushered in this new field of research. It demonstrated that one could use X-ray photography for the study of the structures of the high temperature plasma constituting the solar corona. At the same time, it showed the limitations of the techniques existing at the time. One of the major limitations was the drift in roll about the pointing axis of the attitude control system. This limitation was soon overcome by the development of three axis stabilization, first used by the group at the University of Leicester (Pounds and Russell, 1966) and quickly followed by others. The Leicester group used and optimized the pinhole camera technique, but the method suffers from a basic limitation. There is a conflict between light gathering power and angular resolution. Attempts to improve the spatial resolution, by the use of zone plates, were made by several groups (for example Einigshammer et. al. , 1967) but resulted in only modest success. Zone plates suffer from chromatic aberration which limits their usefulness in studying a broad wave band emitter like the sun. It is also extremely difficult to construct zone plates which combine large collecting area and moderate focal length with high resolving power.

In 1960, Giacconi and Rossi had suggested the use of paraboloid mirrors operating at grazing incidence, to increase the light gathering power of experiments designed to search for cosmic X-ray sources and ultimately to obtain X-ray images. It should be remembered that this was two years before they and their co-workers discovered the first unexpected bright X-ray source in the constellation of Scorpio.

As a result of this suggestion and the stimulus provided by the growing interest in X-ray astronomy a program to study and develop grazing incidence optics for X-ray observations was undertaken by American Science and Engineering under the sponsorship of NASA. This program benefitted from the comprehensive theoretical study of grazing incidence optical systems carried out by Wolter (1952) during an attempt to design practical systems suitable for X-ray microscopy. It appeared natural to first apply this technique to the study of solar X-ray emission. Following the successful construction of the first telescope, a program was proposed to NASA- Goddard Space Flight Center and a collaborative effort involving both groups resulted in the development of an imaging system for use on solar pointed sounding rockets. Several flights resulted in solar X-ray images with resolution of the order of an arc minute.

By the beginning of 1968 several rocket flights, conducted independently by both the GSFC group and the AS&E group, had established that grazing incident optics were already superior in sensitivity and resolution to the pin-hole camera and zone plate techniques (Giacconi et. al. , 1965; Underwood and Muney, 1967). A method of analysis based on the spectral transmission of several X-ray filters had also been formulated which was capable of distinguishing between temperature and density enhancements in the corona (Reidy et. al. , 1968).

The first successful rocket flight of the high resolution X-ray telescope mirror developed by AS&E took place on June 8, 1968 (Vaiana et. al. , 1968) and there have been four subsequent flights of this mirror all of which have been successful. The original payload has now been superseded by one carrying a new, low scatter quartz mirror and a collimated crystal spectrometer. Full details of this new instrument are presented by Davis et. al. (1973a).

The basic instrumentation of the 1968 - 1970 payloads, in addition to the X-ray mirror, consists of several filters which select appropriate wavelength pass-bands and a 35mm camera mounted in the focal plane of the telescope which records both X-ray and visible light images. The payload also contains support electronics which provide power to control the filter wheel and camera, a programmer which selects filter wheel position and camera exposure time, the solar pointing control system, telemetry and other housekeeping functions. The X-ray telescope mirror flown between June 1968 and November 1970 is shown in Figure 2.

In order to obtain information about the physical parameters of the solar corona from the X-ray photographs it is necessary to calibrate the energy response of the film, the spectral transmission of the filters, and the point response function of the mirrors.

The point response function describes the variation with radius of the energy emitted by a point source and imaged in the focal plane. The experimentally determined function for the 1968-1970 Kanigen mirror is shown in Figure 3. The initial slope is steep but it rapidly levels off due to scattering. The full width at half maximum is two arc seconds but the width increases quickly to 20 and 120 arc seconds at 0.1 and 0.01 respectively of the maximum value.

The energy sensitivity of the film is determined by producing an X-ray step wedge containing 16 known exposures generated with Al  $K\alpha$  radiation (8.3 A). The intensities vary by a factor of 2 from one another so that the dynamic range in incident energy is nearly  $10^5$ . In general, this exceeds the range between grain noise and the saturation of the film. Since the range of surface brightness of X-ray emitting features is at least this large, several exposures of varying duration must be taken through each filter during a rocket flight.

Finally the spectral transmission of the filters is required. Two types of filters are used. The first, made from various thicknesses of beryllium, transmit only short wavelengths ( $< 20 \text{ \AA}$ ); the second type is made from aluminized organic materials, such as Parylene, Polypropylene, or Mylar, which transmit X-rays both at the short wavelengths and also beyond the carbon K edge ( $44 \text{ \AA}$ ).

In order to interpret the energies measured at the film plane in terms of coronal temperatures and emission measures it is necessary to know the spectral distribution of the incident soft X-ray emission. This has been achieved by use of a model spectrum, computed originally by Tucker and Koren (1971) and updated by Landini (private communication, 1972). The spectra computed for solar plasmas radiating at  $1.5 \times 10^6 \text{ K}$  and  $5.0 \times 10^6 \text{ K}$  are shown in Figure 4. They consist of a continuum component, produced predominantly by bremsstrahlung and radiative recombination, and a discrete line component. The wavelength distributions of the energy transmitted through two of the commonly used filters are shown in Figures 5 and 6 for the two incident spectra of Figure 4.

From these results it is possible to compute "Spectral Hardness Indices" which are defined as the ratio of the energies transmitted through two filters at all wavelengths; as a function of coronal temperature (see Figure 7). Using these curves, it should be possible to determine the effective temperature (integrated along the line of sight down to the solar surface) at any point on a pair of solar X-ray photographs.

### 3. MORPHOLOGICAL RESULTS

Two kinds of information can be recovered from the X-ray images. These are qualitative descriptions of the images which relate to the morphology and evolution of the physical systems present in the corona and quantitative



results which provide numerical values for the parameters of the solar plasma which will increase our basic knowledge of the magnetohydrodynamics of the corona. From measurements made in visible light at the limb we know that the corona is highly structured down to arc second resolution. Consequently, if we are to obtain significant information about the X-ray emitting structure we will need spatial resolution which is comparable to that obtained in the visible region. In this respect the resolution which has been attainable since 1968 places solar X-ray astronomy in the main stream of solar research.

Visual inspection of X-ray images, such as that shown in Figure 8a, provides information on the three dimensional structures which are present in the corona. Further comparison of such images with simultaneous measurements of the photospheric magnetic field (Figure 8b) immediately indicates the importance of the magnetic field in ordering the shapes of all coronal features. To date six distinct types of quiescent coronal structures have been tentatively identified from the rocket X-ray photographs. These are active regions, active region interconnections (arches), large scale quiet coronal structures (usually associated with unipolar magnetic regions), coronal holes, bright points, and the coronal structures enclosing filament cavities. The dynamics of two transient flare events have also been studied. It is currently unknown whether the active region threads (Davis, 1973b) seen during the March 8, 1973 flight came under the category of quiescent or transient structures.

#### a) Active Regions

Active Regions are, apart from solar flares, the most striking features observed in the X-ray photographs. It became evident at a very early stage

(Reidy et. al. , 1968) that the coronal appearance of active regions in X-ray photographs was not identical to their appearance at chromospheric wavelengths (e. g. H $\alpha$  or CaK). The high resolution photographs have led to a coherent concept of active region structure in the corona and its relationship to the magnetic field which has been summarized by Krieger et. al. (1971a). When active regions are observed at the limb of the sun (Figure 9) they appear as complex tubular arches or loops of enhanced density and temperature which rise to heights of more than  $10^5$  km above the photosphere (Vaiana et. al. , 1968). In Figure 10 an active region is shown where the loop is viewed at an angle and projected against the solar disk. When this picture is compared with the longitudinal magnetic field it is apparent that the loop connects regions of opposite magnetic polarity. This is a general result of active region observations. In the majority of the observations the intensity of the X-ray emission appears to reach a maximum above the vicinity of the neutral line of longitudinal magnetic field and in cases where the field gradient at the neutral line is large, or the neutral line configuration is complex, a bright core, whose width is unresolvable in our telescope, connects the regions of preceding and following polarity across the neutral line (Figure 10). The spectrum of such a core appears harder than that from the rest of the active region and consequently, if the emission has a thermal origin, it implies a higher temperature.

#### b) Coronal Structures and Unipolar Magnetic Regions

Comparison of a CaK photograph of the sun, taken on November 4, 1969, with the corresponding soft X-ray image (see Figure 11) shows that, in quiet regions the chromospheric supergranule structures are filled in at coronal altitudes by emitting material (Vaiana et. al. , 1970). In the case shown the emitting structures are seen to be associated with unipolar magnetic regions and a "ghost" region. In Figure 11 the filled in cells are conjectured to form

the foot points of large coronal structures which connect the two magnetic polarities. The temperature and density of such structures must be lower than that of the active regions because they are not seen in photographs taken through filters which pass only the shorter wavelengths. In the examples of Figure 11 gaps in the emission are observed over the positions of  $H\alpha$  filaments. These will be discussed under the topic of Filament Cavities.

Closed loops joining regions of opposite polarity photospheric field have been observed. A striking example of such a configuration was seen during the November 24, 1970 flight (see Figure 12). If these loops are in fact vertical their height is in excess of 100,000 km. This is borne out by  $H\alpha$  observations at the limb of the prominence whose remnants are seen to underlie the coronal structure. The filament disappeared several days prior to the rocket flight.

### c) Coronal Holes

In the November 24, 1970 soft X-ray observation (Figure 12) a clearly defined area of reduced coronal emission was observed (Krieger et. al. , 1972). A similar area was observed at the limb in the March 7, 1970 flight (Figures 1f and 23). Comparison of the November X-ray observations with images of the underlying  $H\alpha$  and CaK features and of the associated magnetic field distribution (see Figure 12) reveal several remarkable facts.

First little evidence can be seen of the structure in either the  $H\alpha$  or the CaK observations. Indeed, the network elements seen in the latter seem little different from those present in other quiet areas. The magnetic field configuration associated with the feature is however quite distinctive. In the center of the hole it is found that the photospheric field is weak. Surrounding this area are regions of stronger fields of the same polarity which , in turn, are bordered by similarly intense fields of opposite polarity. The closed structure associated with the filament remnant mentioned in the previous section forms the eastern border of the whole while an arcade of closed loops associated with a

"complex of activity" runs the length of the western border. The surrounding structures emphasize the open nature of the hole by appearing to diverge from it. Very little evidence of any coronal emission from the hole can be seen on the solar disk. However, the presence of faint limb brightening in the southwest indicates the presence of some coronal material in the hole. The geometry of the coronal structures associated with the March 7 hole appears very similar in the white light data (Figure 23).

A comparison of the X-ray photograph of November 24, 1970 with solar wind velocity data revealed that the coronal hole was probably the source of a recurrent high velocity stream in the solar wind (Krieger et. al. , 1973).

From the form of the coronal structures seen associated with the observed holes the conclusion must be drawn that coronal holes are the product of solar magnetic field configurations. The prerequisites for their formation are low photospheric field strengths and diverging coronal fields of a single polarity.

#### d) Active Region Interconnections

A further species of quiet coronal structure evident in the soft X-ray observations are active region interconnections. In addition to connecting loops within individual active regions, longer wavelength observations show that neighboring active regions are sometimes linked into "complexes of activity" by means of large scale arch structures (Van Speybroeck et. al. , 1970). Inspection of an active region complex, seen on March 7, 1970 (see Figure 8) reveals interconnections spanning about  $60^{\circ}$  in solar longitude and about  $90^{\circ}$  in latitude. Comparison between the X-ray image and the underlying longitudinal photospheric magnetic field measurement indicates that the interconnections link regions of opposite magnetic field polarity. Usually, the interconnection is to an adjacent active region. There is also evidence that when connections occur across the solar equator they preferentially link the preceding polarities of the two hemispheres. Van Speybroeck et. al. pointed out that these latter inter-

connections are exactly those called for by the Babcock (1961) model of the solar cycle. Hansen et. al. (1972) have recently noted a similar phenomenon in the K-coronameter data which they have named "trans-equatorial arches". It would appear that both the X-ray and white light observations show the same phenomenon.

#### e) Bright Points

In addition to the large scale structures of the corona, there are also small pointlike features of relatively bright soft X-ray emission which are not associated with active regions (Vaiana et. al., 1970) (see Figure 13). These features appear to coincide with some, but not all, of the brightest spots in the CaK network. Although several dozen bright points have been observed on the X-ray photographs, only a few of these features have been examined in detail. So far, all appear to be invariably associated with the occurrence of small regions of opposite polarity magnetic field in generally unipolar magnetic regions (Krieger et. al., 1971a). They are thus, in all probability, the X-ray manifestation of low lying closed bipolar magnetic structures outside the active regions.

In view of the characteristics of these regions it is tempting to propose that they are miniature active regions, or represent an early phase in the development of active regions. Two factors however combine to throw doubts on this interpretation. First, in many cases the points are seen to be outside generally accepted active region latitudes (bright points are visible in the south polar region in Figure 12). In addition, a study of small bipolar magnetic regions (K. Harvey and S. Martin, private communication) indicates that their lifetime is only of the order of a day. If the features studied by Harvey and Martin coincide with the X-ray coronal bright points, then the lifetimes of the bright points are short compared with 'standard' active region lifetimes and

they do not develop into active regions. The X-ray latitude distribution and (if verified at X-ray wavelengths) the magnetic lifetime distribution lead one to believe, therefore, that these bright points represent a different phenomenon.

#### f) Filament Cavities

In a previous section a brief comment was made to the effect that a cavity (observed as a reduction in coronal emission) is invariably observed to be above quiescent filaments. An excellent example of such a structure was observed on November 24, 1970 (see Figure 14).

The coronal configuration seen associated with the filament suggests that of the Kippenhahn and Schluter (1957) model of filament geometry. The temperature and density characteristics of the coronal features seen are apparently similar to those of the other quiet coronal structures. Ray-like projections, which are probably the feet of coronal loops are seen radiating approximately perpendicularly to the filament. These appear to be aligned with the loops in the filament itself. The emission from the material directly over the filament (if any) is too faint to determine whether, in this case, the coronal loops close above the filament. Certainly they are seen to close over particular portions of the filament. In this case, as well as that of a large filament observed in the March 7, 1970 data, the closures take place over areas where the  $H\alpha$  absorption is weak. This may, however, be coincidental.

Directly above the quiescent filament and above all other quiescent filaments so far observed, a distinct cavity is seen. This was found in the case of the filament shown in Figure 14 to have a projected area in X-rays which was three times that of the enclosed filament as observed in  $H\alpha$  (Timothy et. al., 1972). An analysis of the projection effects on the X-ray image, showed that the non-emitting cavity extended to a height of at least  $2 \times 10^4$  km above the top of the  $H\alpha$  filament. Observations at the limb showed the  $H\alpha$  feature to have a height of approximately  $5 \times 10^4$  km. Thus the coronal cavity was more than  $7 \times 10^4$  km in height.

The X-ray features associated with quiescent filaments (cavities over which apparently high closed structures may be observed) are in marked contrast to the low-lying bright loops observed over active filaments marking the neutral line of active regions. Davis et. al., (1973b) observed bright loops over active filaments which can be traced back through active regions, on the one hand, and cavities around quiescent filaments which are associated only with remnants and unipolar magnetic regions, on the other (see Figure 1h). It would thus appear that, if active and quiescent filaments mark different stages in the evolution of the neutral line of the photospheric field, then the coronal structures follow this evolution by progressing from low-lying dense loops which are bright X-ray emitters to very high tenuous structures which do not emit observable fluxes of soft X-rays at their tops. Perhaps the high arches proceeding between the unipolar magnetic regions associated with the remnant filament channel of Figure 12 represent an intermediate stage. This general evolution would be consistent with the K-coronameter observations of Hansen et. al. (1972).

Filament cavities associated with quiescent filaments should not be confused with coronal holes for which no dark filaments or even aligned fibril structure is observed in  $H\alpha$ . The former are apparently enclosed areas of low temperature or low density plasma while the latter are certainly open, low temperature regions.

#### g) Solar Flares

On two of the rocket flights, we have observed importance 1 flares in progress (Vaiana et. al., 1968; Krieger et. al., 1970). In Figure 15 the appearance of the flare observed on June 8, 1968 in 3 - 18 Å X-rays is compared with  $H\alpha$  and CaK observations and with a magnetogram of the flaring region. The similarity between the X-ray and  $H\alpha$  emission has been noted before (Vaiana

and Giacconi, 1969); the important difference was also noted, however, that the X-rays show a bright feature which bridges the magnetic neutral line of the flare. This structure emits more than 50% of the total energy of the flare in this waveband.

The second flare, observed on November 4, 1969, occurred close to the limb. Its appearance is more difficult to interpret because of foreshortening; for the same reason, the magnetic field data is not available. Although the X-ray appearance, in this case, shows little correlation with the on-band  $H\alpha$  there exists a similarity between the brightest portions of the two X-ray flares insofar as the emission in both cases is localized in narrow structures. In the November 4 flare (Figure 16) two cores can be identified, and these correspond to the brightest emission regions appearing in the  $H\alpha$  wings. At least 98% of the total energy in the 3 to 18 Å band originates from these bright spots (Krieger et. al., 1971a). In the flare of June 8, the surrounding X-ray plage contributed approximately 50% of the total emission (Vaiana and Giacconi, 1969).

It is probable that the similarity between the bright cores observed in the non-flaring active regions and the centers of emission in flares indicates a generic relationship. In both cases they are narrow linear structures associated with the neutral line of the longitudinal field at a position where the neutral line is complex. It is assumed that this region plays an important part in the flare process.

#### 4. QUANTITATIVE DATA REDUCTION AND ANALYSIS

The methods by which numerical parameters such as electron temperature and density as a function of position are deduced from the X-ray images are not very different from the methods used in the quantitative analysis of visible light images. Certain difficulties are introduced when



working in X-rays; the broad scattering wings of the X-ray telescope point response function must be taken into account and the wavelength dependence of the film's response to incident energy must be considered. The results that follow are preliminary in the sense that these factors are neglected. They do, however, serve to point out the techniques of quantitative interpretation of solar X-ray images, and to demonstrate the existence of temperature and density structure in X-ray emitting coronal active regions.

The X-ray images were digitized by an Optronics P1000 scanning microdensitometer with an aperture of 25 micrometers (4 arc seconds). Photographic density was converted to incident energy by comparison with a sensitometric step wedge, exposed to  $8.3 \text{ \AA}$  aluminum  $K\alpha$  X-rays, and developed and scanned along with the flight film.

The quantity measured in any X-ray exposure through a given filter is the energy deposited on the film per unit area at a given point ( $I_{\text{filter}}$ ). This quantity is related to the physical parameters of the given region by the equation:

$$I_{\text{filter}} = \frac{A}{4\pi f^2} \int_0^{\infty} N_e^2 dl \int_{\lambda_1}^{\lambda_2} p(\lambda, T(l)) \eta_{\text{filter}}(\lambda) d\lambda \quad (1)$$

where the first integral is taken along the line of sight, and

$A$	= geometrical collecting area of telescope
$f$	= focal length of telescope
$N_e$	= electron density
$l$	= distance along the line of sight
$\eta_{\text{filter}}(\lambda)$	= filter transmission and telescope reflectivity at $\lambda$
$\lambda_1$ and $\lambda_2$	= the wavelengths where $\eta(\lambda)$ becomes effectively zero
$p(\lambda, T)$	= power emitted at wavelength $\lambda$ by unit emission measure at temperature $T$

The quantity  $F_{\text{filter}}(T) = \int_{\lambda_1}^{\lambda_2} p(\lambda, T) \eta(\lambda) d\lambda$  is currently determined from the modified version of the theoretical calculations of Tucker and Koren (1971) to determine  $p(\lambda, T)$  and from laboratory calibrations to determine  $\eta(\lambda)$ .

Since the term  $\frac{A}{4\pi f^2} N_e^2$  is constant for all filters, the Spectral Hardness Index, the ratio of the intensity passed by two filters:

$R_{12}(T) = \frac{I_1}{I_2} = \frac{F_1(T)}{F_2(T)}$  is a measure of the effective temperature of a region along the line of sight. If the filters are appropriately chosen  $R(T)$  is a monotonic function in the temperature range of interest. The effective emission measure along the line of sight is then given by the relation,

$$\left[ \int N_e^2 dl \right]_{\text{effective}} = \frac{I_{\text{filter}}}{F_{\text{filter}}(T)} \frac{4\pi f^2}{A} \quad (2)$$

The above derivation assumes coalignment between images. In order to transform all images from a single rocket flight into a common coordinate system, the coordinates of up to nine common features (the exact number depends on the exposure) are determined from contour plots of the photographic density distribution. The necessary rotation and translation parameters are then computed by a least squares fitting procedure.

#### a) Analysis of Active Regions

In order to demonstrate this analysis technique it has been applied to a bright region (McMath 11035) which was situated on the west limb of the sun on November 24, 1970. Figure 17 shows the appearance of the region of interest in exposures in two X-ray passbands. It is evident that the region is characterized by a bright core of short wavelength emission (implying higher temperature) and a structured extended region surrounding this core. The re-

sult of the first step in the analysis, a contour map of the energy deposited in the film plane in the 3 - 35, 44 - 51 Å waveband is shown in Figure 18. In order to investigate the physical characteristics within the region, intensity cross sections are computed for two wavebands along a line perpendicular to the limb (Figure 19a and b).

As mentioned in the previous section, X-ray photographs of active regions observed on the disk (for example (Figure 10) show that active regions consist of bright low lying cores and higher well-defined loop and large-scale arch structures. Accordingly, the intensity scan data has been interpreted in two ways.

In the lower two plots of Figure 19, a "slab model" has been assumed in which the temperature along the line of sight is considered constant. This is analogous to assuming that all the emission along a given line of sight comes from a restricted region (e.g., an isothermal loop). Accordingly, the spectral hardness ratio  $R(T)$  (related to effective temperature) and the effective emission measure  $N_e^2 dl$  corresponding to that temperature are plotted as functions of position.

An alternative approach would be to assume spherical symmetry for the active region. This would be analogous to the assumption that the X-radiation is all emitted from a contained arch feature without significant fine structure. If the structure of the active region along the line of sight is identical to the structure perpendicular to the line of sight, a mathematical inversion of the intensity traces may be performed. The temperature and density can then be derived as functions of radial position. Figures 20 and 21 show the results of the inversion procedure applied to the two scans of Figure 19a and 19b.

Although neither of the two models chosen corresponds to the real structure of the active region, the results are indicative of the range of conditions to be found. The region appears to consist of a low-lying "core" loop of high temperature and high density material surrounded by a less structured

"halo", probably composed of structures which are not resolved in the microdensitometer scans. It would appear, from these results, that the bright "core" loop is primarily a temperature phenomenon and that the decrease in density between the "core" loop and the "halo" is less abrupt. The decrease of temperature with height in the "halo" arch structure is slow, however, and the X-ray emission declines with the emission integral.

Several sources of ambiguity in this analysis must be mentioned. The conclusions are dependent on the correct assignment and interpretation of the Spectral Hardness Index. The relationship between Spectral Hardness Index and temperature is non-linear. Thus, a shift in either the experimental spectral hardness measurements or the theoretical calculations of  $R(T)$  could change the character of the results significantly. Improper assignment of spectral hardness ratios could result from a variety of causes (e.g., spectral variation in the film sensitivity or telescope scattering function, improper evaluation of the film fog level, etc.). Incorrect evaluation of the relationship between spectral hardness and temperature could result from an incorrect analysis of the solar X-ray spectrum. An effort has been made to use the best data available to resolve all of these ambiguities.

A more fundamental difficulty which arises, however, is the fact that the emission from a small quantity of very hot material along the line of sight can be masked by the emission from a much larger quantity of cooler material. For example, a conspicuous X-ray feature was observed behind the northeast limb in the November 24, 1970 photographs. This was identified as the active region McMath 11060. An analysis (Krieger et al., 1971b) of a conspicuous arch structure visible in this region indicated that the structure was essentially isothermal at a temperature of  $2.5 \times 10^6$  K ( $\pm 2 \times 10^5$  K) with a peak emission integral of  $1.1 \times 10^{30} \text{ cm}^{-5}$  ( $\pm 10^{29} \text{ cm}^{-5}$ ). However, a hot "core" comprising up to 10% of the total plasma along the line of sight at

$3.5 \times 10^6$  K or 4% at  $4 \times 10^6$  K, would not have produced a statistically significant increase in the Spectral Hardness Index of the brightest point in the active region. This difficulty can be overcome by finding a self-consistent solution to a combination of exposures taken with many filters passing different portions of the soft X-ray waveband, or by a combination of imaging techniques (for structure perpendicular to the line of sight) with high resolution spectroscopy (for thermal distributions along the line of sight).

#### b) Analysis of Large Scale Structures

In principle, plasma conditions in the quiet corona can be determined by the same methods used in the analysis of the active regions. In practice, the exposure durations attainable from sounding rockets prohibited the assignment of accurate spectral hardness ratios to cool ( $< 2 \times 10^6$  K) features prior to the development of the low-scatter, high efficiency, X-ray telescope rocket payload discussed by Davis, et. al., (1973a). However, in certain special cases the temperature of the corona can be determined from the X-ray photographs by means of a different technique (Krieger et. al., 1973). When long exposures are obtained through thin filters a distinct limb brightening is visible at the quiet limb (see Figure 8 for an example of this phenomenon). Microdensitometer scans through such areas are often found to be well fitted by simple exponential functions of the form:

$$I(h) = I(0) \exp(-h/h_1) \quad (3)$$

where  $I$  is, once more, the X-ray energy deposited on the film per unit area and  $h$  is the height above the limb.

If the intensity distributions at the limb, which are represented by equation (3) are interpreted as radiation from an isothermal region with spherical symmetry about the limb and density  $N(h) = N_0 \exp(-h/H)$  (where  $N_0$  is the density at the base of the corona and  $H$  is the density scale height) then

the emission integral becomes:

$$\int N_e^2(h) dl \approx N_0^2 \exp(-2h/H) \sqrt{\pi R_\odot H} (1+h/2R_\odot) \quad (4)$$

(the radial variation of the gravitational potential over the height range of the observations is neglected). Therefore  $h_l \approx H/2$ . If in addition, it is assumed that the plasma is in hydrostatic equilibrium under the influence of gravity only, the temperature of the emitting material can be derived from the scale height using the barometric relation  $H = kT \mu / mg_\odot$ , where  $\mu$  is the mean molecular weight (0.62) and  $g_\odot$  is the acceleration of gravity at the solar surface.

As an example of this technique radial scans were made through the limb of the November 24, 1970 image. Two scans, one passing through an area of typical limb brightening, which is probably a closed region according to the discussion of Van Speybroeck et. al., (1970), and the other passing through the coronal hole, are shown in Figure 22.

Fitting an expression of the form of equation (3) to the data, it was found that of five closed structures scanned, four had scale heights lying in the range  $6.62 \times 10^4 \text{ km} < h_l < 8.24 \times 10^4 \text{ km}$ . On the other hand, the scale height of the hole material was  $(3.27 \pm .12) \times 10^4 \text{ km}$ . Thus, it is apparent that the intensity scale height  $h_l$  in the hole is approximately half that in the typical closed structure.

Numerical evaluation of the measured scale heights leads to barometric "temperatures" of  $1.3 \times 10^6 \text{ K}$  in the hole region and  $3.1 \times 10^6 \text{ K}$  in the typical closed structure. However, the fact that the longest exposures through thin beryllium filters (passband 3 - 18 Å) taken during this flight showed only faint traces of the closed coronal structures or limb brightening implies that the temperature of the quiet coronal plasma was lower than that generally associated with active regions ( $2 - 3 \times 10^6 \text{ K}$ ).

The explanation of this apparent discrepancy can be found in the morphological results of the previous section. In general it has been established that X-ray emitting coronal structures indicate the presence of transverse fields (i. e. , closed structures). In such a situation however the assumption made in this analysis, that the coronal plasma is in radial hydrostatic equilibrium, is invalid (although hydrostatic equilibrium along the field lines is allowed). Thus only in the case of radial magnetic fields, such as those in the coronal hole region, can the scale height be directly related to the temperature. Moreover, if the temperature and the field geometry of the closed structures can be derived by independent measurements, the scale height can be used to determine the strength of the transverse field.

However, the temperature derived for the coronal hole region is probably valid.\* If one assumes that the scale heights measured at the limb also define the range of values for the similar closed structures observed on the disk, the comparisons of intensity measurements made near the sun center through the thin organic filter can be used to derive the conditions at the base of the corona. Krieger et. al. , (1973) found a temperature of  $1.5 \times 10^6$  K at a density of  $2.7 \times 10^9 \text{ cm}^{-3}$ .

## 5. SUMMARY AND CONCLUSION

The attainment of a spatial resolution capability of the order of several arc seconds in the AS&E soft X-ray observations has enabled a wide variety of coronal features to be recognized and their morphology studied. Quantitative data reduction and analysis techniques are also being developed to permit the physical characteristics of these features to be studied.

Since many of the coronal structures identified in the X-ray photo-

---

\* Any plasma acceleration due to coronal expansion will reduce the scale height at a given temperature relative to a static corona, but this effect should be negligible in the first few scale heights.

graphs differ significantly in appearance from their counterparts at other levels in the solar atmosphere, it is valuable to summarize their observed characteristics in the form of a table (Table II).

Comparison of the different types of X-ray emitting features with the underlying magnetic field structures, or H $\alpha$  and CaK features has been possible for most of the past AS&E rocket flights. Thus, in general, the correspondences between features seen at photospheric and chromospheric levels and those seen in the low corona are well known.

In the case of the outer coronal observations, however, the situation is less well defined. One flight, that of March 7, 1970, occurred at the time of a solar eclipse. Accordingly, the soft X-ray data were compared with the white light radial density gradient filter photograph of the corona of Newkirk and Lacey (1970). Figure 23 is a superposition of the soft X-ray photograph and the white light photograph. The detailed correspondence between inner and outer coronal structures on these photographs was discussed by Van Speybroeck et. al., (1970). In the absence of additional eclipse data an attempt has been made to equate outer coronal structures with low coronal features on the basis of the published properties of the former (Hansen et. al., 1972; Dunn, 1970).

The availability of higher resolution X-ray images in the near future will doubtless result in the discovery of other characteristic coronal features.

With the exception of the two flare observations no studies of the temporal variations of coronal features have been possible with the existing soft X-ray images. The observations have however triggered many questions concerning the temporal variations of the structures seen. The development of an active region, from its appearance as an emerging flux loop to its gradual disintegration into wide spread unipolar areas presents a fascinating study. The possibility of observable coronal field geometry changes being



seen to accompany flare events, or radio bursts will also lead to interesting investigations; as will the life history of coronal bright points. The development of coronal holes, their evolution as a function of time, and their relationship to the solar wind also presents an interesting problem. These questions, as well as many others requiring variable time resolution data cannot be answered by sounding rocket observations. Hopefully, they will, however, be answered through analysis of the data returned from the AS&E soft X-ray telescope launched on the Apollo Telescope Mount (ATM).

Quantitative analysis of soft X-ray image data is still in its infancy. However, a number of refinements have recently been made in the techniques used to measure the surface reflectivity and scattering properties of X-ray telescopes and in the techniques of calibration of X-ray films. The result is that the determination of coronal temperatures and densities from the soft X-ray images is becoming more precise. The inclusion of collimated crystal spectrometers in the new telescope payload will also advance the quantitative study of coronal conditions from X-ray images by providing simultaneous high resolution soft X-ray spectra of the coronal features observed.

## ACKNOWLEDGEMENTS

A great many people contributed to the success of the five year program of sounding rocket observations whose results are summarized in this paper. The leadership of Riccardo Giacconi and the advice and encouragement of Bruno Rossi throughout the program are gratefully acknowledged by the authors. J. Davis, W. Reidy, L. Van Speybroeck and T. Zehnpfennig all made major contributions to the success of various rocket flights.

The design and construction and field support of the rocket payload were the responsibility of the engineering and technical staff at A.S. &E.; A. De Caprio and H. Manko took leading roles in this effort. R. Haggerty was responsible for the photographic aspects of the program. D. Webb, R. Simon and W. Hamilton provided valuable assistance in the areas of payload calibration and data analysis.

The rocket flights were conducted by the Sounding Rocket Branch of the NASA Goddard Space Flight Center at the facilities at White Sands Missile Range. Most of the flights used SPARCS pointing control systems developed at NASA Ames Research Center under the supervision of E. Gabris.

The rocket program was funded by NASA. The support and encouragement of H. Glaser, G. Oertel, and J. Weldon of NASA Office of Space Sciences are acknowledged. The research resulting in this paper was supported by NASA under Contract Number NASW-2346.

It is a pleasure for one of the authors (GV) to thank the staff of the Istituto di Fisica and the Science Faculty of the University of Palermo (Italy) for the opportunity offered in connection with his teaching appointment there and for the stimulating atmosphere conducive to the elaboration of some of the material included in this work.

Table 1  
Summary of Sounding Rocket Flights (1968 - 1973)

<u>Date</u>	<u>Time (UT)</u>	<u>Filters*</u>	<u>Film</u>
8 June 1968	1740-1745	10. 2 $\mu$ m Be 51 $\mu$ m Be 3. 8 $\mu$ m Mylar+0. 2 $\mu$ m Al 2. 5 $\mu$ m Fe (steel)	Panatomic-X untopcoated Panatomic-X untopcoated 103-0 Ilford Special
8 April 1969	1700-1716	10. 2 $\mu$ m Be 1. 0 $\mu$ m Parylene C+0. 3 $\mu$ m Al 3. 8 $\mu$ m Mylar+0. 3 $\mu$ m Al 0. 15 $\mu$ m Al	Panatomic-X untopcoated Panatomic-X Microfile
4 November 1969	2027-2033	10. 2 $\mu$ m Be 44. 1 $\mu$ m Be 3. 5 $\mu$ m Parylene N+0. 2 $\mu$ m Al	Kodak type 3400
7 March 1970	1853-1859	10. 2 $\mu$ m Be 0. 85 $\mu$ m Parylene N+0. 25 $\mu$ m Al 3. 8 $\mu$ m Mylar+0. 2 $\mu$ m Al 3. 2 $\mu$ m Teflon+1. 1 $\mu$ m Parylene N+ 0. 2 $\mu$ m Al	Kodak SO-114
24 November 1970	2045-2051	10. 2 $\mu$ m Be 44. 1 $\mu$ m Be 0. 85 $\mu$ m Parylene N+0. 25 $\mu$ m Al 5. 7 $\mu$ m Parylene N+0. 32 $\mu$ m Al	Kodak SO-114
8 March 1973 <sup>+</sup>	1800-1806	10. 2 $\mu$ m Be 44. 1 $\mu$ m Be 1. 0 $\mu$ m Polypropylene+0. 3 $\mu$ m Al	Kodak SO-212

\* In addition to the filters listed, all flights except those of 8 June 1968 and 4 November 1969 carried a fixed heat rejection prefilter in the optical path. This filter consisted of 0. 13 $\mu$  m Al attached to a 78% transparent Ni mesh.

<sup>+</sup> A new payload with a low-scatter, quartz X-ray telescope and 2 collimated crystal spectrometer was used for this flight (Davis et. al. , 1973a).

Table II - Characteristics of X-ray Structures

X-ray structures				Corresponding features at other wavelengths		
type	Appearance	Spectral Hardness	Magnetic Field (Photosphere)	H $\alpha$ (Chromosphere)	CaK (Chromosphere)	White Light (Corona)
X-ray Active Regions	Bright loops crossing neutral line- Very Bright, Low core	Hard spectrum (high temperature) very hard spectrum	Strong bipolar fields	Plage	Plage	Coronal Enhancements
Active Region Interconnections	Large scale arches connecting active regions-may connect preceding polarities across equator*	softer than active regions	Complex of activity	Not observed	Not observed	Trans-equatorial* arches Intermediate Helmets
Large scale coronal structures	Large scale loops and arches connecting active regions-of opposite polarity	Softer spectrum than active region interconnections	Unipolar magnetic regions and "ghosts" at footpoints of coronal structures	active region remnants	enhanced network	Intermediate Helmets Helmet streamers
Coronal Bright Points	Small bright features which appear randomly distributed on the disk in long exposures through thin filters	Softer spectrum than active region interconnections	Small region of Bipolar field	Occasionally, a bright patch is seen	Doubled, bright spots in network, but most bright spots in CaK are <u>not</u> coronal bright points	?
Filament Structures	Non-emitting cavity surrounded by closed loop structures	Softer spectrum than active region interconnections	Bipolar fields bordering filament	Dark filament or aligned fibril structure (Filament Channel)	Enhanced network bordering filament	Helmet structures
Coronal Holes	Large non-emitting area bordered by diverging structure - Very low scale height at limb	low scale height . implies probably softer spectrum than large scale coronal structures	weak, unipolar fields (diverging in corona)	no distinctive feature	No distinctive feature	Low density coronal hole
Soft X-ray flares	Extremely bright core of few arc seconds width at a point on the neutral line. May or may not be accompanied by enhanced emission from active region	Extremely hard	Strong bipolar fields	flare	flare	?

\*Most active region interconnections do not cross the equator rather they proceed from one active region to another adjacent one. Those which cross the equator are probably identifiable as trans-equatorial arches. The others probably manifest themselves as intermediate helmets in the K-coronameter data.

### Figure Captions

Figure 1 - A representative set of solar X-ray photographs demonstrating the progress of the X-ray imaging technique. (a) The first X-ray image of the sun made with a grazing incidence telescope (October 15, 1963). (b) An image obtained on March 17, 1965 by an electroformed Nickel X-ray telescope with resolution of about 30 seconds of arc. (c) An X-ray image from the first successful flight of the series discussed in this paper (June 8, 1968). An importance 1B solar flare is close to the center of the disk. (d) An image obtained April 8, 1969. Numerous X-ray bright points are visible on the original negative. The cross-hatched appearance of the coronal structures was caused by the placement of the heat-rejection pre-filter. (e) An image obtained November 4, 1969. An importance 1B flare is evident on the east limb. (f) An X-ray photograph obtained shortly after fourth contact of the solar eclipse of March 7, 1970. (g) An X-ray image obtained November 24, 1970. (h) An X-ray image obtained from the first successful flight of a new X-ray telescope of higher efficiency (March 8, 1973).

Figure 2 - The Kanigen-coated Beryllium X-ray telescope mirror used for rocket observations of the sun between 1968 and 1970 in its mount. The view is from the hyperboloid (back) end of the mirror. A visible light aspect lens used on the early flights is mounted to the center plate of the telescope.

Figure 3 - The point response function of the X-ray telescope shown in Figure 2. The ordinate is in experimental units which do not reflect the absolute calibration of the telescope throughput. The dots

represent measurements made by microdensitometry of photographic images of a pinhole . The triangles represent the result of inversion of proportional counter slit scan data.

Figure 4 - The theoretical solar emission spectrum from 3 to 60 Å plotted for the temperatures  $1.6 \times 10^6$  K (upper) and  $5 \times 10^6$  K (lower). For convenience in computation (see text), the ordinate is the power (in units of  $\text{ergs}/\text{cm}^2 \text{ sec}$ ) emitted by unit emission measure in a 0.2 Å wavelength interval.

Figure 5 - The spectra of Figure 4 after filtering through a thin aluminized organic filter. At  $1.6 \times 10^6$  K a significant fraction of the energy passing the filter is in the OVII lines at 21.6 - 22 Å. At  $5 \times 10^6$  K, a number of lines contribute significantly, primarily from Fe XVI and Fe XVII.

Figure 6 - The spectra of Figure 4 filtered by a thin beryllium filter. At  $1.6 \times 10^6$  K, the Ne IX (13.4 Å) line is the most important contributor with significant energy passed from Fe XV, XVI, and XVII. At  $5 \times 10^6$  K, the lines of Fe XVII contribute as well as Mg XI (9.2 Å) and Si XIII (6.6 - 6.8 Å).

Figure 7 - Spectral Hardness ratios for the two filters of Figures 5 and 6, together with a thicker beryllium filter. Spectral hardness is defined as the ratio of the total energies passed by two filters at a given temperature.

Figure 8 - A comparison between the appearance of the sun in soft X-rays and the photospheric magnetic field. Left: an X-ray exposure through a thin aluminized organic filter taken March 7, 1970 shortly after fourth contact of the solar eclipse. The limb of the moon is visible to the southeast of the limb of the sun. Right: A map of the longitudinal component of the photospheric magnetic field as observed by Livingston, Harvey and Slaughter (Kitt Peak National Observatory).

Figure 9 - The appearance of active region structures in X-rays at the limb. Top: X-ray photographs in the  $3 - 17 \text{ \AA}$  passband of active region associated coronal features. Left: A group of active regions near the limb. At least three arches connecting different portions of the group can be distinguished. Right: A loop structure associated with an active region very close to the limb. The coronal loop extends to an altitude of at least 150,000 km. Bottom:  $H\alpha$  photographs of the corresponding portions of the disk taken two hours before the rocket flight (June 8, 1968) by NOAA Boulder Observatory.

Figure 10 - The appearance of active region structures in projection on the disk. Top left: A group of active regions observed November 4, 1969 in the  $3 - 23 \text{ \AA}$ ,  $44 - 56 \text{ \AA}$  soft X-ray wavebands. Top right: The same regions observed in  $H\alpha$  (courtesy of Sacramento Peak Observatory). Bottom left: CaK (courtesy of Sacramento Peak Observatory). Bottom right: Longitudinal component of the photospheric magnetic field (courtesy of Mt. Wilson Observatory).

Figure 11 - The appearance of a unipolar magnetic region in (from top to bottom): 3 - 23 Å, 44 - 64 Å X-rays; photospheric magnetic field (courtesy of Mt. Wilson Observatory); H $\alpha$  and CaK. The H $\alpha$  and CaK photographs were provided by the Sacramento Peak Observatory.

Figure 12 - The southern portion of the solar disk on November 24, 1970. The X-ray photograph shows both high loop structure overlying the remnants of a filament which had disappeared several days before and a large coronal hole near the central meridian. The appearance of the coronal hole and surrounding in (a) 3 - 35 Å and 44 - 51 Å X-rays; (b) photospheric magnetic field on November 25, 1970, with the approximate position of the November 24th disk marked (courtesy of Kitt Peak National Observatory); (c) CaK spectroheliogram (courtesy of Sacramento Peak Observatory); (d) H $\alpha$  spectroheliogram (courtesy of Sacramento Peak Observatory).

Figure 13 - An X-ray 'bright point' in the quiescent corona and the underlying structures in CaK (courtesy of Sacramento Peak Observatory) and the photospheric magnetic field (Kitt Peak National Observatory).

Figure 14 - A quiescent filament in the northern hemisphere observed on November 24, 1970 in (top) 3 - 35 Å, 44 - 51 Å X-rays and (bottom) H $\alpha$  (Sacramento Peak Observatory).

Figure 15 - Appearance of the solar flare of June 8, 1968 (1742 UT) in X-rays, H $\alpha$  and CaK and the magnetic configuration at the time of the flare. Top left: 3 - 18 Å X-rays. Top right: H $\alpha$  (courtesy of NOAA



Boulder Observatory). Bottom left: CaK (courtesy of McMath-Hulbert Observatory). Bottom right: Photospheric longitudinal field (courtesy of J. Harvey, Kitt Peak National Observatory).

Figure 16 - The appearance of the solar flare of November 4, 1969 in  $H\alpha$  and X-rays. Top to bottom: Red wing  $H\alpha$ ,  $H\alpha$  on band, Blue wing, 3-12 Å X-rays. The photographs were taken at about 2030 UT. The  $H\alpha$  photographs were provided by H. Zirin, California Institute of Technology. The bracket below the photographs is one arc minute in length.

Figure 17 - X-ray images of the coronal active region above McMath plage 11035. Top: Photograph through a thin organic filter passing the bands 3 - 35 Å and 44 - 51 Å. Middle: Photograph through a thin beryllium filter passing the band 3 - 18 Å. Bottom: Photograph through a thicker beryllium filter (3 - 12 Å).

Figure 18 - A contour map of the energy deposited in the film plane made from the upper photograph of Figure 17. The isophotes represented linear energy intervals. The dashed lines labeled N-S and E-W are tangential and radial to the limb respectively through the point of maximum brightness.

Figure 19 - The radial scan line through the peak of region 11035. (a) X-ray intensity through the thin organic filter. (b) X-ray intensity through the beryllium filter. (c) Spectral hardness at each point along the scan line. The small peaks at 1 and 2 arc minutes from the brightest point are probably statistical fluctuations, but the peak

in spectral hardness at the brightest point is statistically significant.

(d) The emission integral along the line of sight computed from the spectral hardness data and the intensities through the organic filter according to the formula of equation (2).

Figure 20 - Electron temperature as a function of position for region 11035 computed by inverting the data of Figure 19 (a) and (b) under the assumption of spherical symmetry. The temperature decreases only slightly beyond 20 arc-seconds from the center of the region.

Figure 21 - Electron density as a function of position for region 11035.

Figure 22 - Graph of X-ray intensity as a function of radial position for the coronal hole and for a typical closed region. (November 24, 1970, 3 - 25  $\text{\AA}$  and 44 - 51  $\text{\AA}$  bandpass). The error brackets on the points represent the second to least significant bit of the microdensitometer. The data is quantitized at the lowest levels. For each plot the intensity scale height  $h_I$  is determined from a least squares fit to the data.

Figure 23 - A composite print of the solar corona on March 7, 1970 composed of an X-ray exposure in the 3 - 36  $\text{\AA}$ , 44 - 64  $\text{\AA}$  wavebands and the radial density gradient filter white light exposure of Newkirk and Lacey (1970). There is a one-to-one correspondence between the position of the bases of white light coronal structures and regions of enhanced limb brightening in the X-ray image.

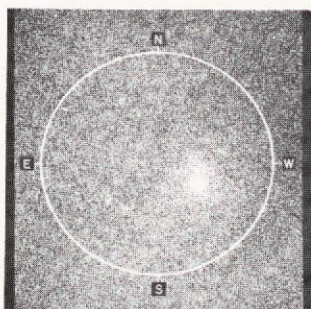
## REFERENCES

- Babcock, H.W.: 1961, *Astrophys. J.* 133, 572.
- Blake, R.L., Chubb, T.A., Friedman, H., and Unzicker, A.E.: 1963, *Astrophys. J.* 137, 3.
- Davis, J.M., Krieger, A.S., Vaiana, G.S. and Van Speybroeck, L.: 1973a, In preparation.
- Davis, J.M., Krieger, A.S., Timothy, A.F. and Vaiana, G.S.: 1973b, In preparation.
- Dunn, R.B.: 1971, in C. J. Macris (ed.), 'Physics of the Solar Corona', 114.
- Einighammer, H.J., Elwert, G., and Mayer, U.: 1967, *Space Research* VII, 1336.
- Giacconi, R. and Rossi, B.: 1960, *J. Geophys. Res.* 65, 773.
- Giacconi, R., Reidy, W.P., Zehnpfennig, T., Lindsay, J.C. and Muney, W.S.,: 1965, *Astrophys. J.* 142, 1274.
- Hansen, S.F., Hansen, R.T., and Garcia, C.J.: 1972, *Solar Physics*, 26, 202.
- Kippenhahn, R. and Schluter, A.: 1957, *Zs. Astrophys.*, 43, 36.
- Krieger, A.S., Vaiana, G., Van Speybroeck, L., Zehnpfennig, T. and Zombeck, M.: 1970, *Bull. Am Phys. Soc.* 15, 612.
- Krieger, A.S., Vaiana, G.S. and Van Speybroeck, L.P.: 1971a, in R. Howard (ed.) 'Solar Magnetic Fields', *IAU Symp.* 43, 397.
- Krieger, A.S., Timothy, A.F. and Vaiana, G.S.: 1971b, *Bull. Am. Astr. Soc.*, 3, 439.
- Krieger, A.S., Barrett, T., Timothy, A.F., Vaiana, G.S., and Van Speybroeck, L.: 1972, *Bull. Am. Astr. Soc.* 4, 386.
- Krieger, A.S., Timothy, A.F. and Roelof, E.C.: 1973, *Solar Phys.*, in press.
- Newkirk, G. and Lacey, L.: 1970, *Nature*, 226, 1098.
- Pounds, K.A. and Russell, P.C.: 1966 in R.L. Smith-Rose (ed.) 'Space Research VI', 32.

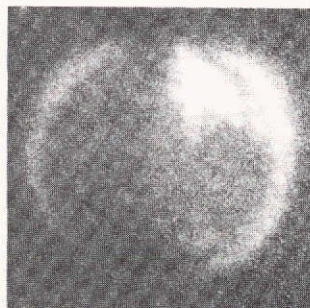
- Reidy, W.P., Vaiana, G.S., Zehnpfennig, T. and Giacconi, R.: 1968, *Astrophys. J.*, 151, 333.
- Timothy, A.F., Barrett, T., Krieger, A.S., Vaiana, G.S. and Van Speybroeck, L.: 1972, *Bull. Am. Astr. Soc.* 4, 393.
- Tucker, W.H. and Koren, M.: 1971, *Astrophys. J.*, 168, 283.
- Underwood, J.H. and Muney, W.S.: 1967, *Solar Phys.*, 1, 129.
- Vaiana, G.S., Reidy, W.P., Zehnpfennig, T., Van Speybroeck, L. and Giacconi, R.: 1968, *Science* 161, 564.
- Vaiana, G.S. and Giacconi, R.: 1969, in D.A. Tidman and D.G. Wentzel (eds.), 'Plasma Instabilities in Astrophysics', 91.
- Vaiana, G.S., Krieger, A.S., Van Speybroeck, L. and Zehnpfennig, T.: 1970, *Bull. Am. Phys. Soc.*, 15, 611.
- Vaiana, G.S., Haggerty, R., Krieger, A.S., Van Speybroeck, L., and Webb, D.: 1973 "An Atlas of Solar X-ray Photographs - March 15, 1968 to November 24, 1970" American Science and Engineering Technical Report.
- Van Speybroeck, L.P., Krieger, A.S. and Vaiana, G.S.: 1970, *Nature*, 227, 818.
- Wolter, H.: 1952, *Ann. Phys.* 10, 94.

REPRODUCIBILITY OF THE  
ORIGINAL PAGE IS POOR

a



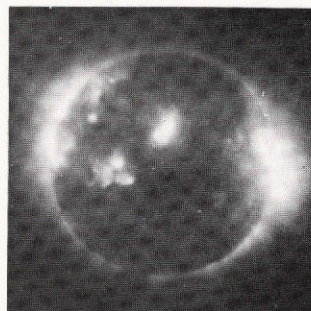
b



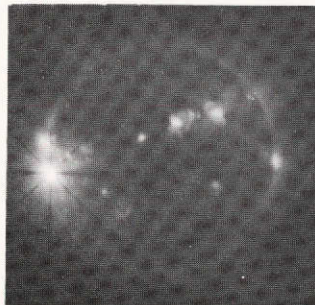
c



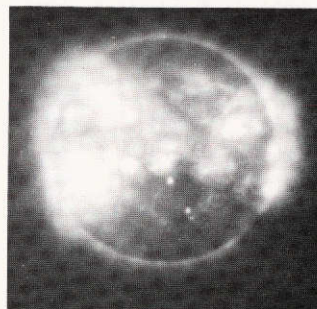
d



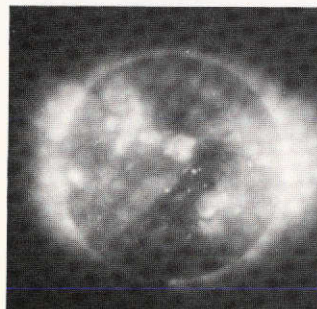
e



f



g



h



### Figure Captions

Figure 1 - A representative set of solar X-ray photographs demonstrating the progress of the X-ray imaging technique. (a) The first X-ray image of the sun made with a grazing incidence telescope (October 15, 1963). (b) An image obtained on March 17, 1965 by an electroformed Nickel X-ray telescope with resolution of about 30 seconds of arc. (c) An X-ray image from the first successful flight of the series discussed in this paper (June 8, 1968). An importance 1B solar flare is close to the center of the disk. (d) An image obtained April 8, 1969. Numerous X-ray bright points are visible on the original negative. The cross-hatched appearance of the coronal structures was caused by the placement of the heat-rejection pre-filter. (e) An image obtained November 4, 1969. An importance 1B flare is evident on the east limb. (f) An X-ray photograph obtained shortly after fourth contact of the solar eclipse of March 7, 1970. (g) An X-ray image obtained November 24, 1970. (h) An X-ray image obtained from the first successful flight of a new X-ray telescope of higher efficiency (March 8, 1973).



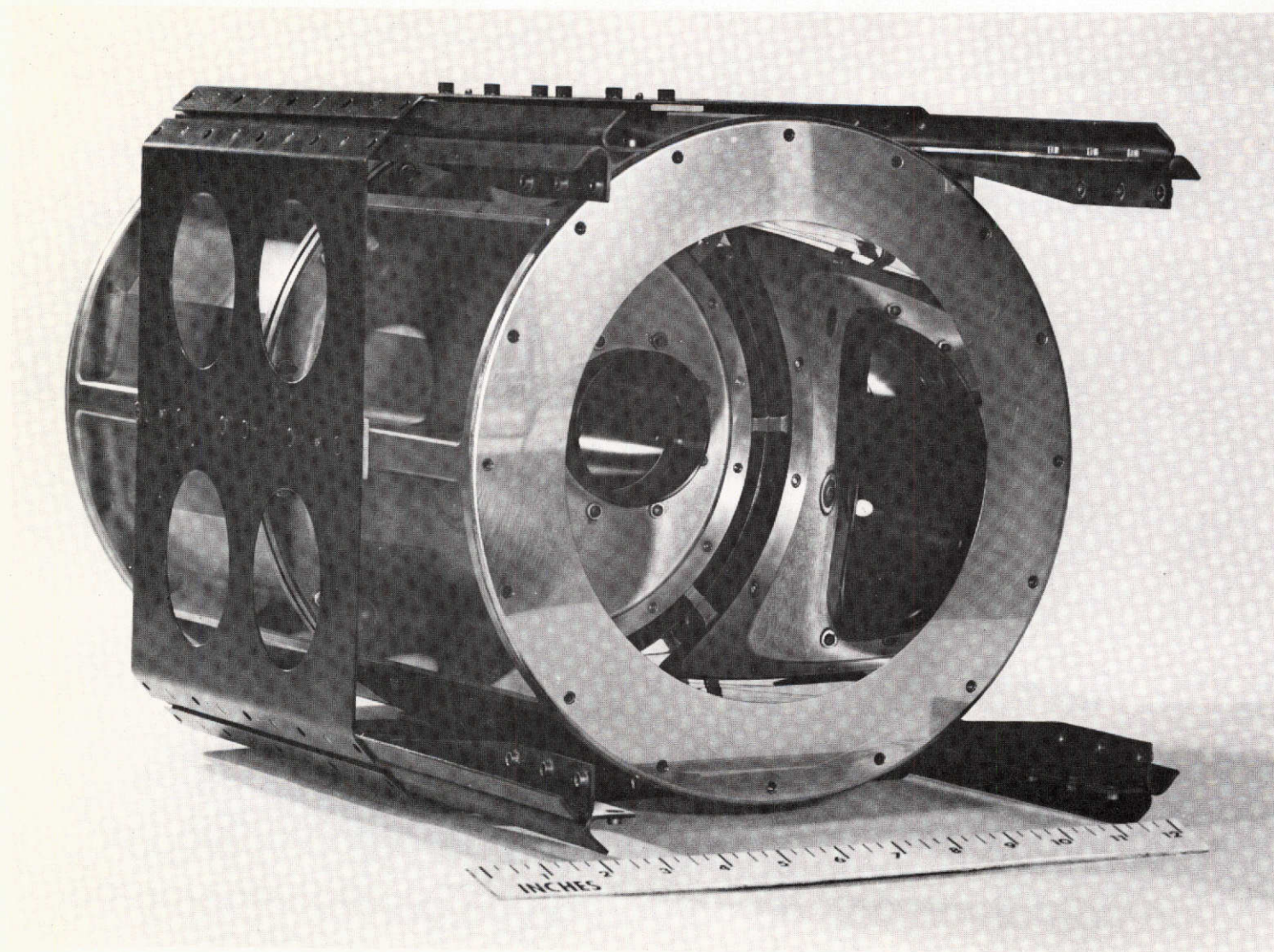


Figure 2 - The Kanigen-coated Beryllium X-ray telescope mirror used for rocket observations of the sun between 1968 and 1970 in its mount. The view is from the hyperboloid (back) end of the mirror. A visible light aspect lens used on the early flights is mounted to the center plate of the telescope.

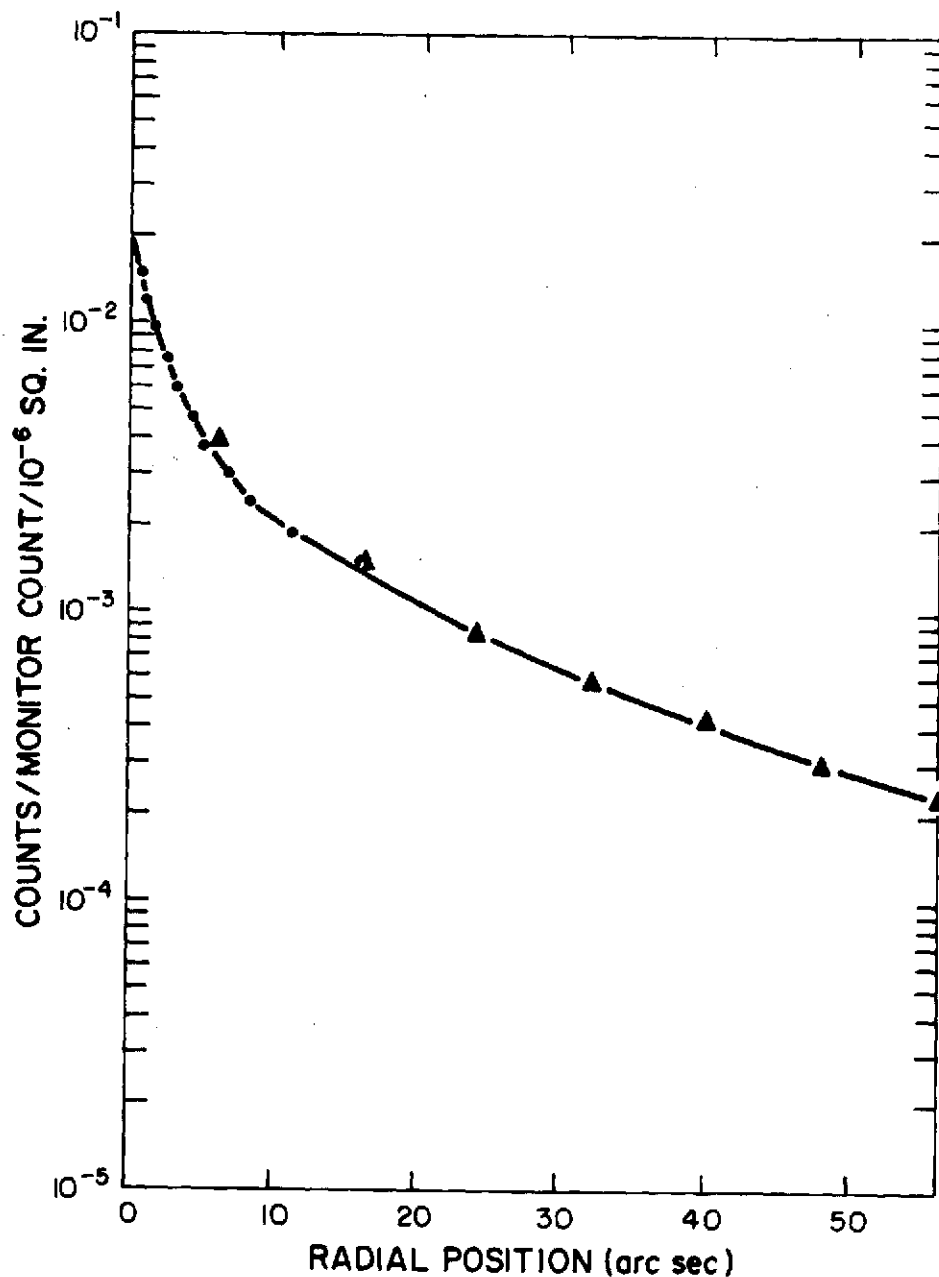


Figure 3 - The point response function of the X-ray telescope shown in Figure 2. The ordinate is in experimental units which do not reflect the absolute calibration of the telescope throughput. The dots represent measurements made by microdensitometry of photographic images of a pinhole. The triangles represent the result of inversion of proportional counter slit scan data.



REPRODUCIBILITY OF THE  
ORIGINAL PAGE IS POOR

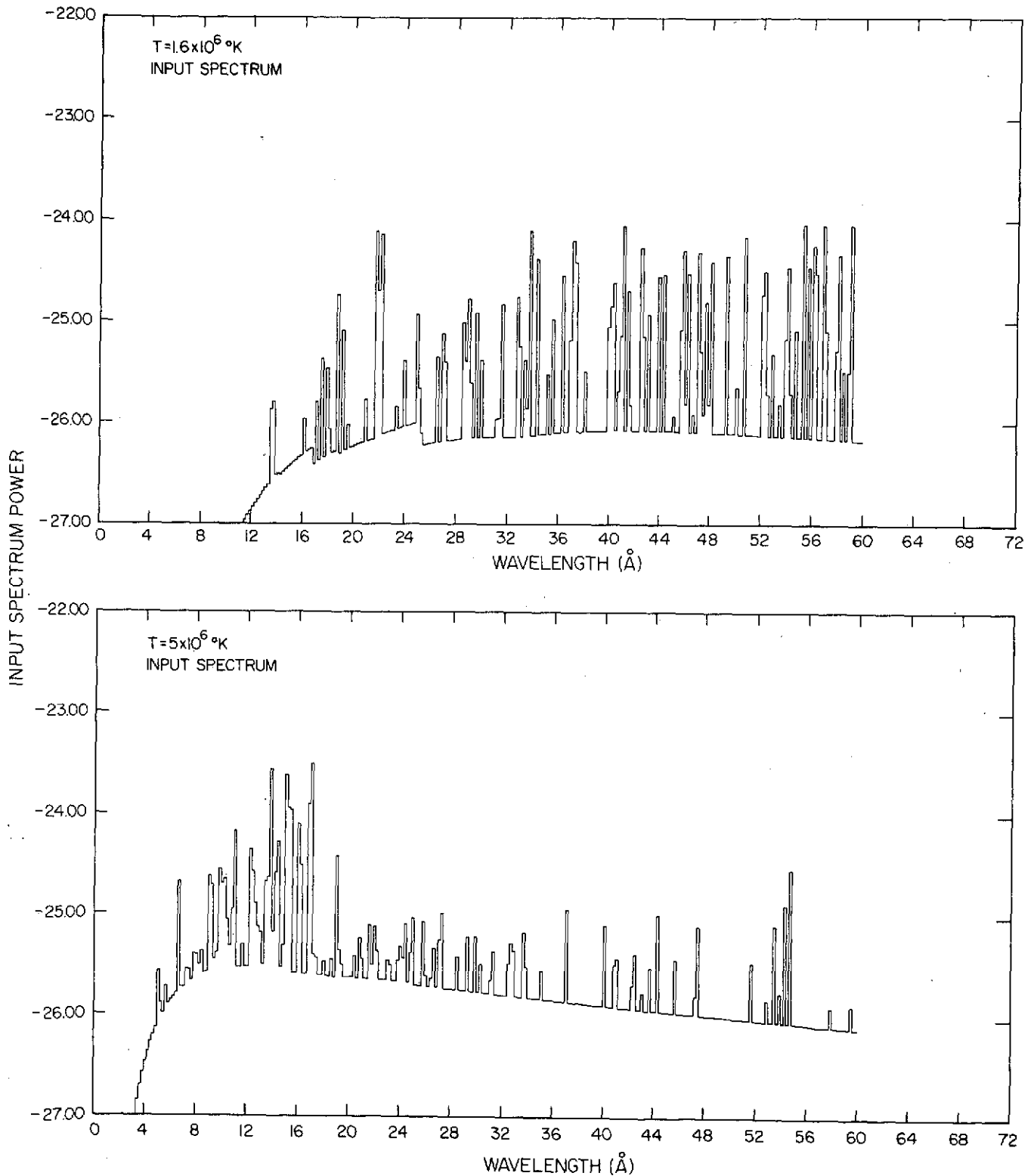


Figure 4 - The theoretical solar emission spectrum from 3 to 60 Å plotted for the temperatures  $1.6 \times 10^6$  K (upper) and  $5 \times 10^6$  K (lower). For convenience in computation (see text), the ordinate is the power (in units of ergs/cm<sup>2</sup> sec) emitted by unit emission measure in a 0.2 Å wavelength interval.

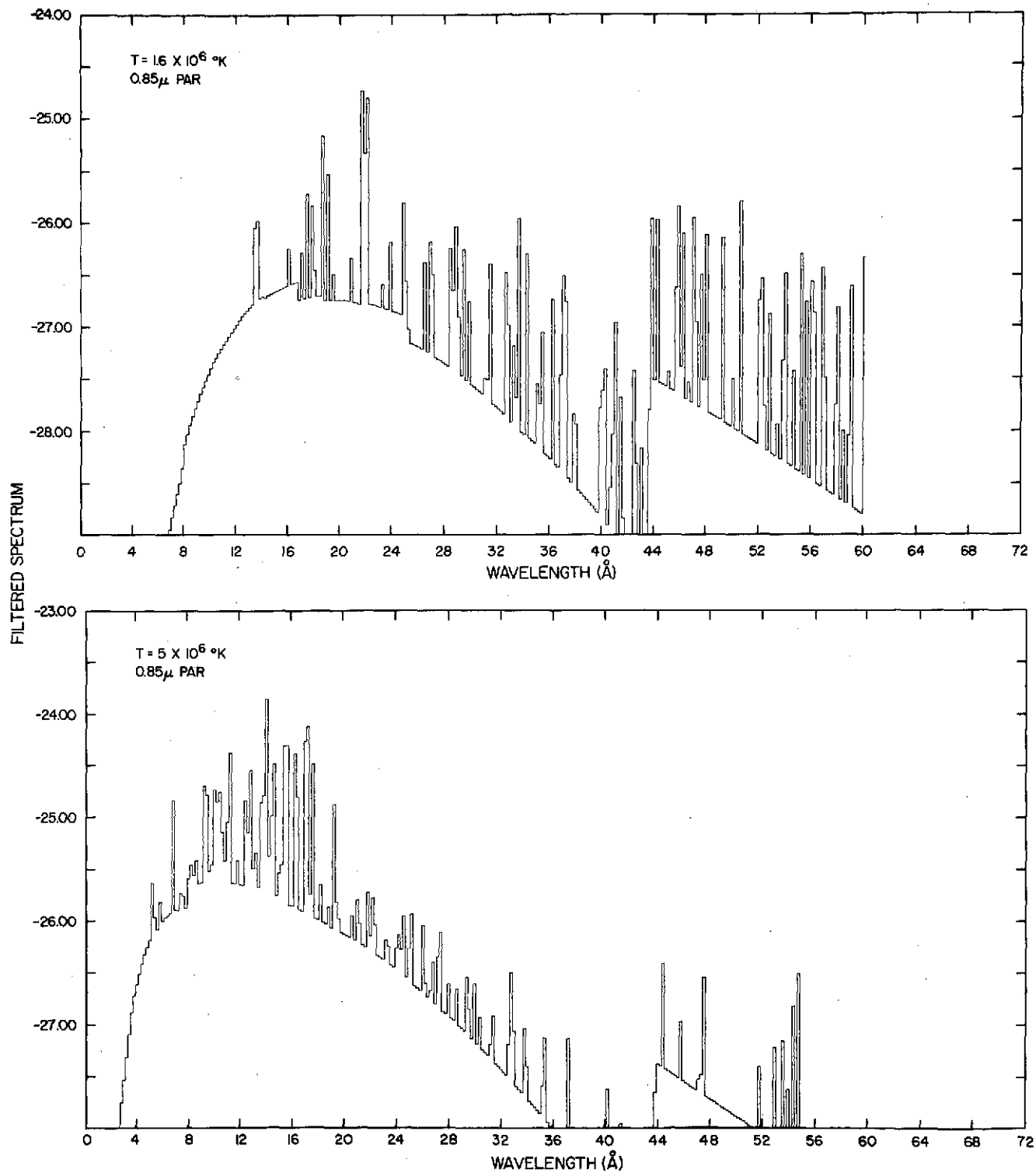


Figure 5 - The spectra of Figure 4 after filtering through a thin aluminized organic filter. At  $1.6 \times 10^6 \text{ K}$  a significant fraction of the energy passing the filter is in the OVII lines at  $21.6 - 22 \text{ Å}$ . At  $5 \times 10^6 \text{ K}$ , a number of lines contribute significantly, primarily from Fe XVI and Fe XVII.

REPRODUCIBILITY OF THE  
ORIGINAL PAGE IS POOR

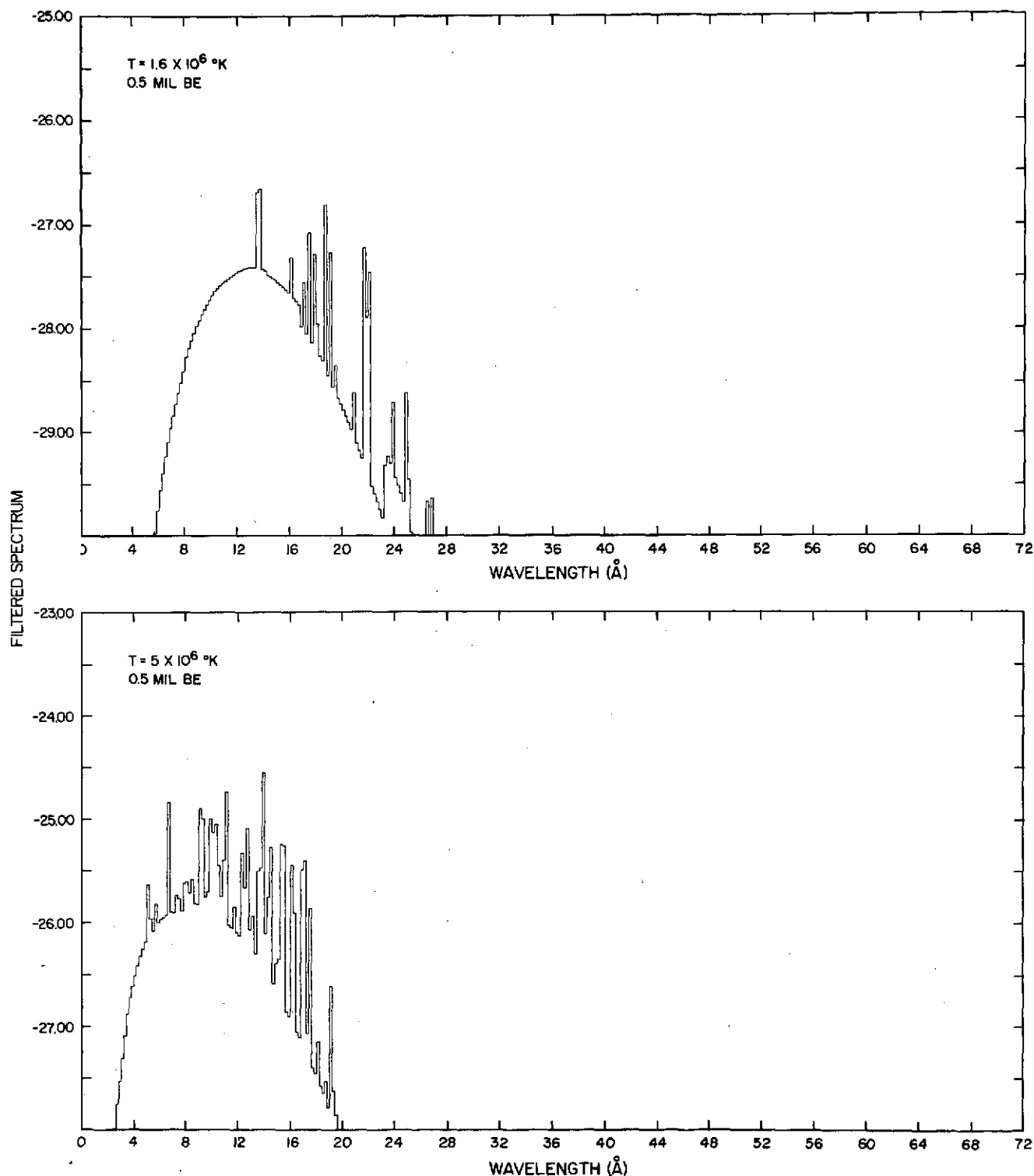


Figure 6 - The spectra of Figure 4 filtered by a thin beryllium filter. At  $1.6 \times 10^6 \text{ K}$  the Ne IX (13.4 Å) line is the most important contributor with significant energy passed from Fe XV, XVI, and XVII. At  $5 \times 10^6 \text{ K}$ , the lines of Fe XVII contribute as well as Mg XI (9.2 Å) and Si XIII (6.6 - 6.8 Å).

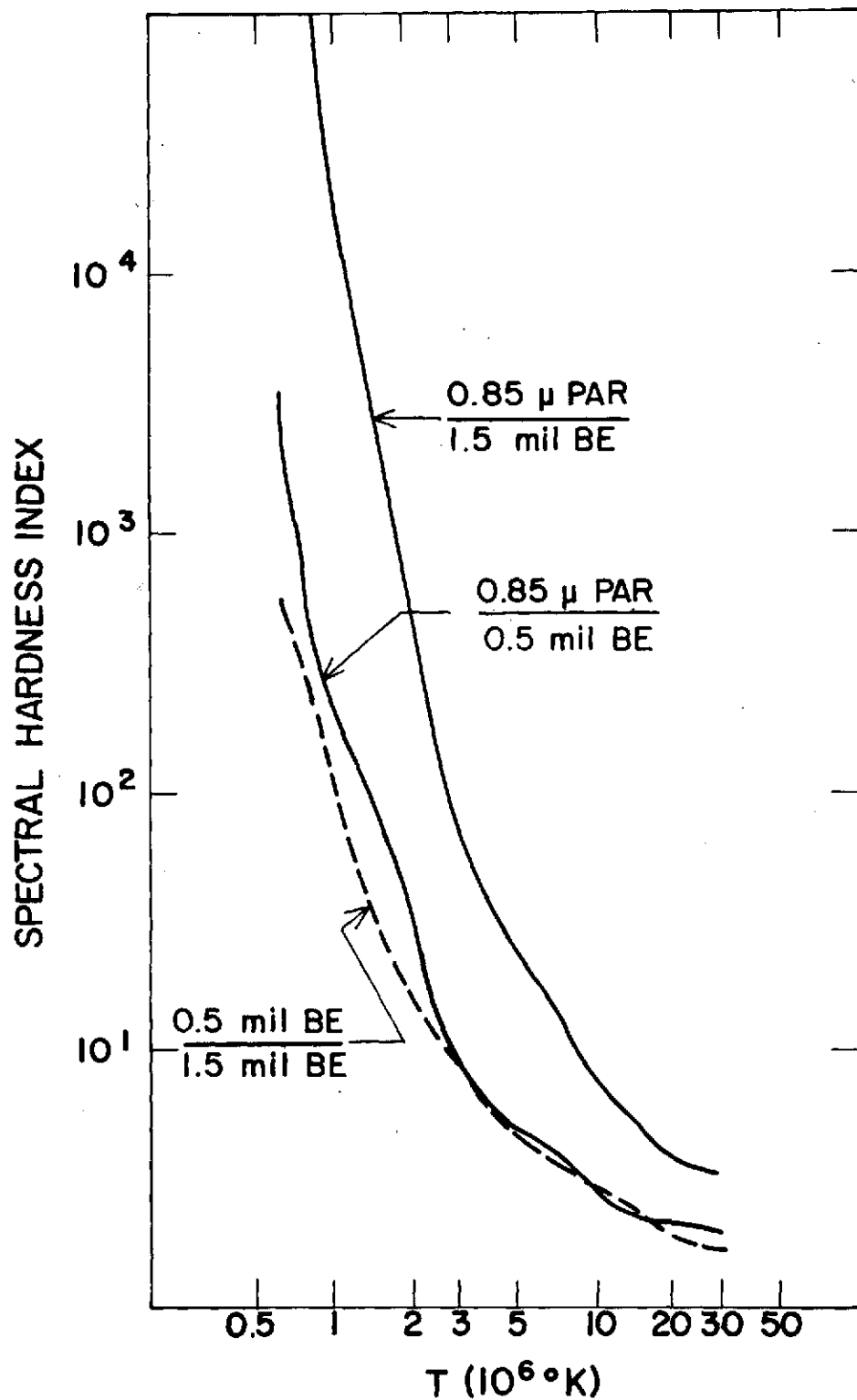


Figure 7 - Spectral Hardness ratios for the two filters of Figures 5 and 6 together with a thicker beryllium filter. Spectral hardness is defined as the ratio of the total energies passed by two filters at a given temperature.

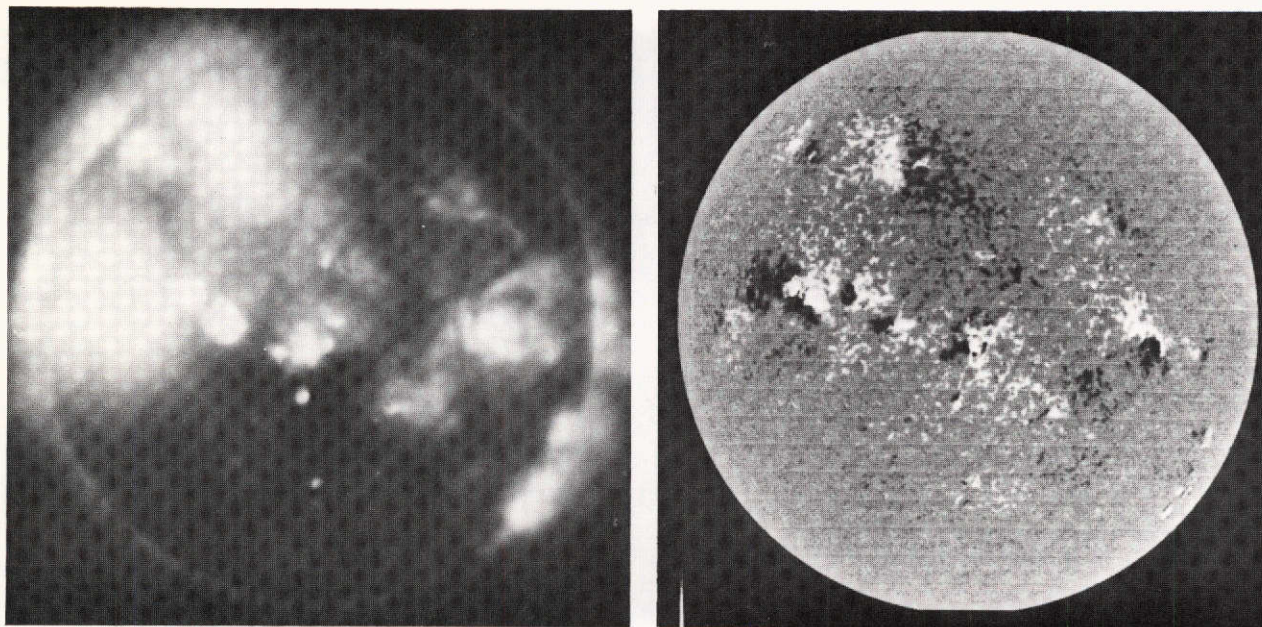


Figure 8 - A comparison between the appearance of the sun in soft X-rays and the photospheric magnetic field. Left: an X-ray exposure through a thin aluminized organic filter taken March 7, 1970 shortly after fourth contact of the solar eclipse. The limb of the moon is visible to the southeast of the limb of the sun. Right: A map of the longitudinal component of the photospheric magnetic field as observed by Livingston, Harvey and Slaughter (Kitt Peak National Observatory).



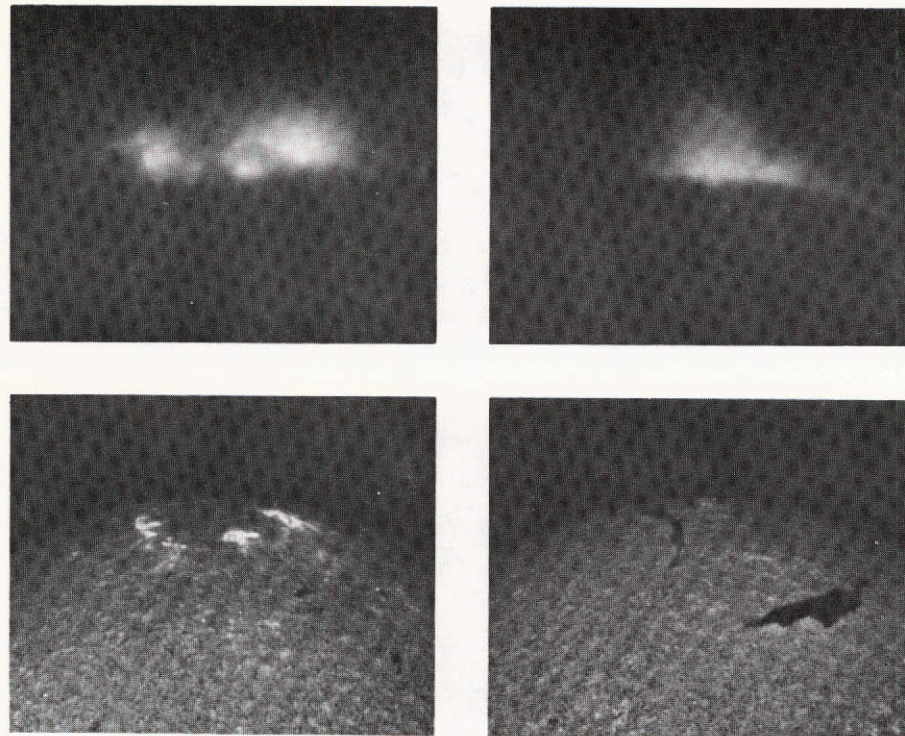


Figure 9 The appearance of active region structures in X-rays at the limb. Top: X-ray photographs in the 3 - 17 Å passband of active region associated coronal features. Left: A group of active regions near the limb. At least three arches connecting different portions of the group can be distinguished. Right: A loop structure associated with an active region very close to the limb. The coronal loop extends to an altitude of at least 150,000 km. Bottom: H $\alpha$  photographs of the corresponding portions of the disk taken two hours before the rocket flight (June 8, 1968) by NOAA Boulder Observatory.



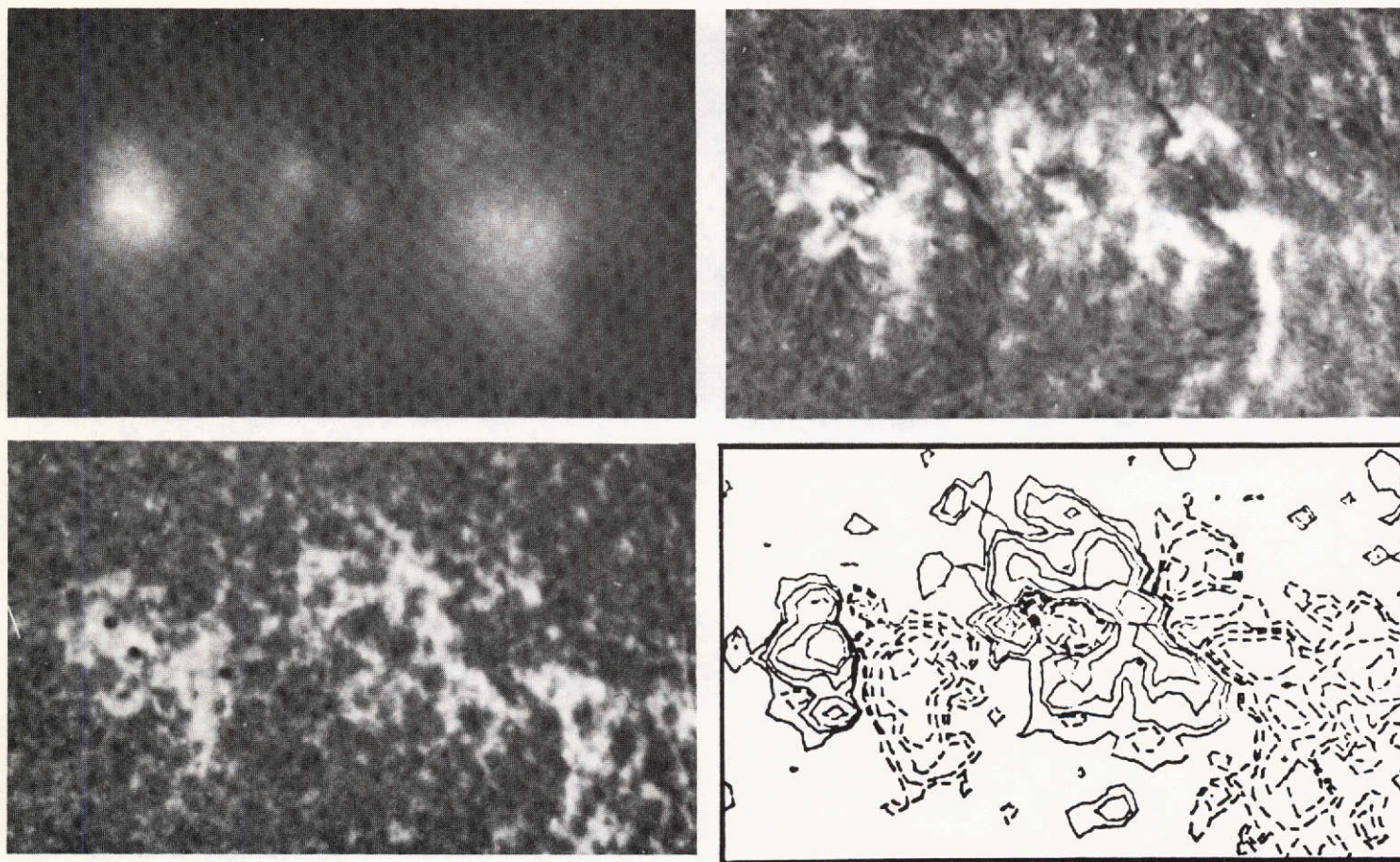


Figure 10 - The appearance of active region structures in projection on the disk. Top left: A group of active regions observed November 4, 1969 in the  $3 - 23 \text{ \AA}$ ,  $44 - 56 \text{ \AA}$  soft X-ray wavebands. Top right: The same regions observed in  $H\alpha$  (courtesy of Sacramento Peak Observatory). Bottom left: CaK (courtesy of Sacramento Peak Observatory). Bottom right: Longitudinal component of the photospheric magnetic field (courtesy of Mt. Wilson Observatory).



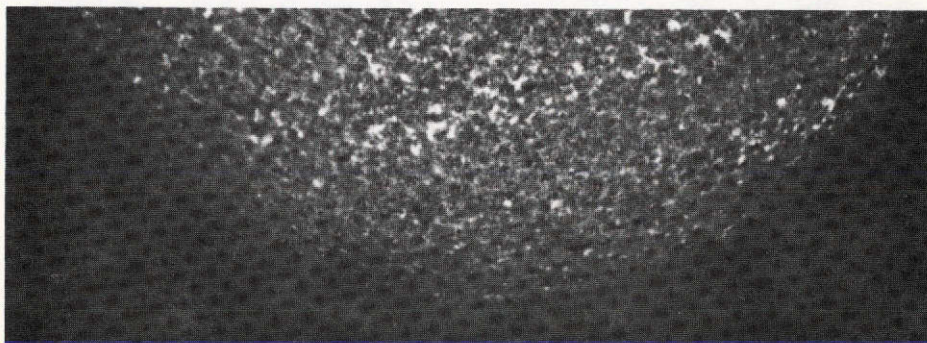
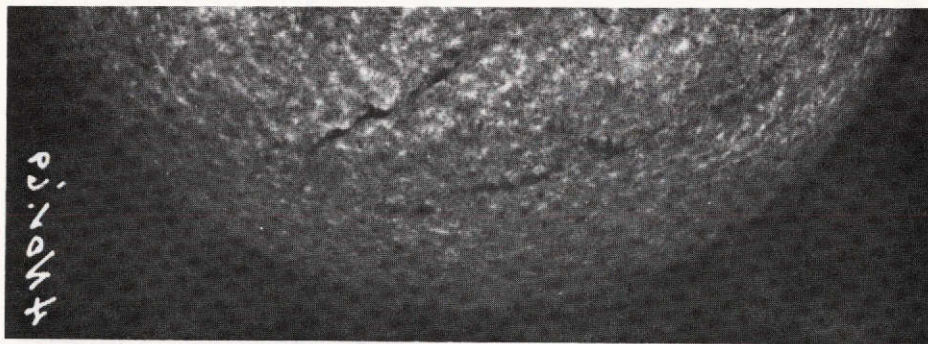
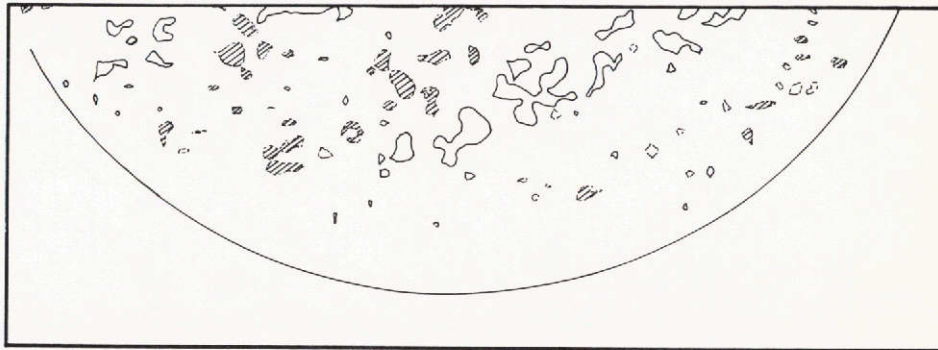
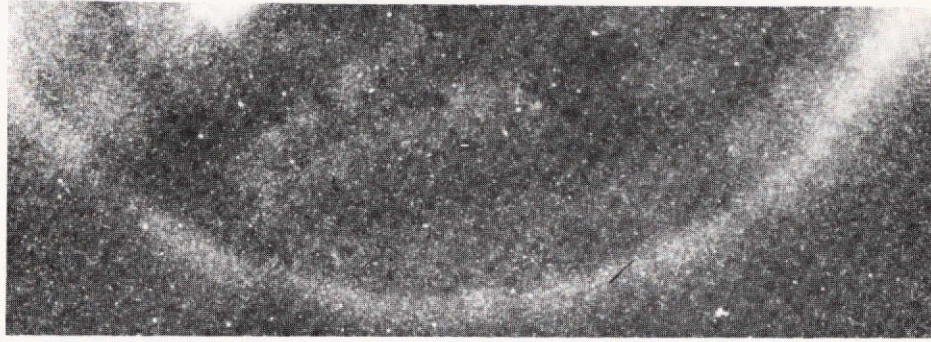


Figure 11 - The appearance of a unipolar magnetic region in (from top to bottom): 3 - 23 Å, 44 - 64 Å X-rays; photospheric magnetic field (courtesy of Mt. Wilson Observatory); H $\alpha$  and CaK. The H $\alpha$  and CaK photographs were provided by the Sacramento Peak Observatory.



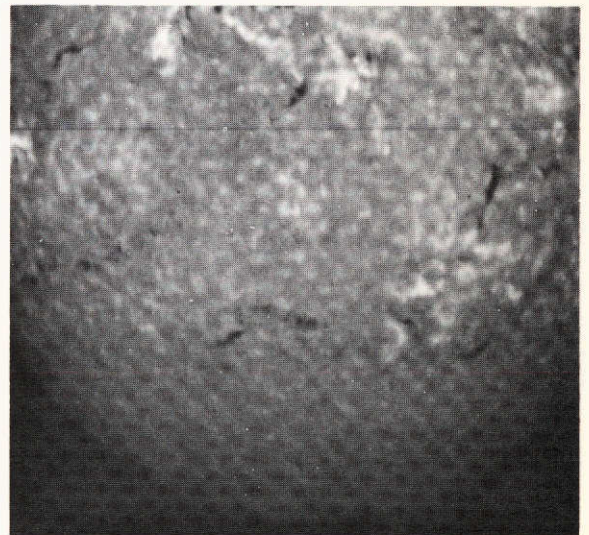
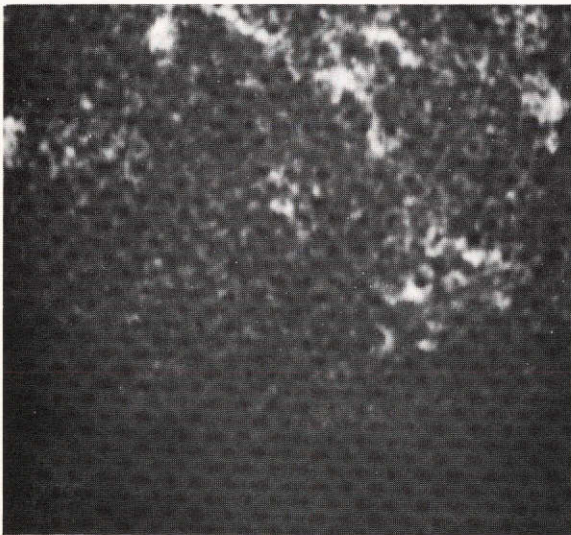
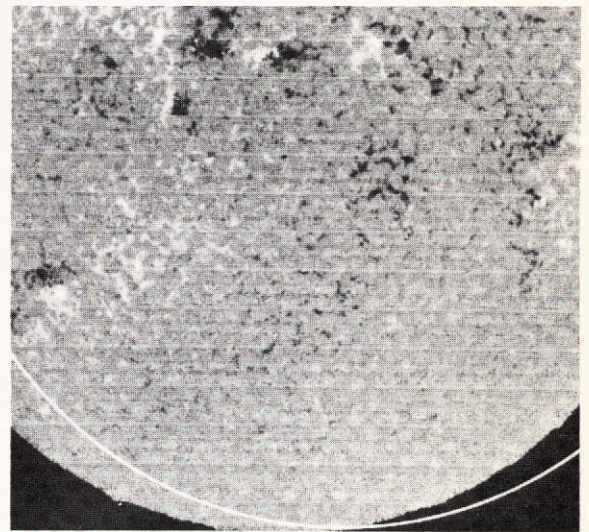
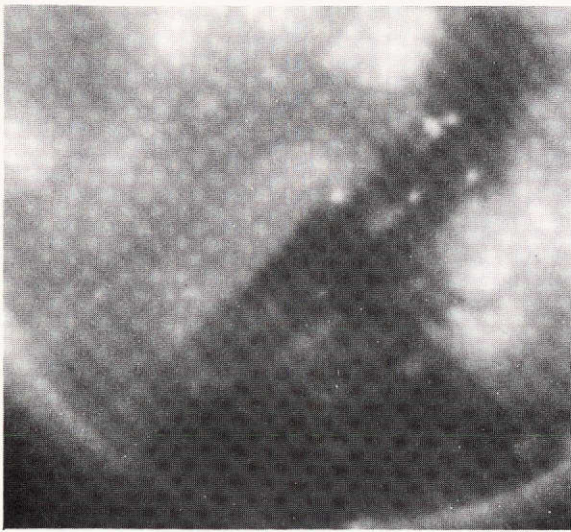


Figure 12 - The southern portion of the solar disk on November 24, 1970. The X-ray photograph shows both high loop structure overlying the remnants of a filament which had disappeared several days before and a large coronal hole near the central meridian. The appearance of the coronal hole and surrounding in (a)  $3 - 35 \text{ \AA}$  and  $44 - 51 \text{ \AA}$  X-rays; (b) photospheric magnetic field on November 25, 1970, with the approximate position of the November 24th disk marked (courtesy of Kitt Peak National Observatory); (c) CaK spectroheliogram (courtesy of Sacramento Peak Observatory); (d)  $H\alpha$  spectroheliogram (courtesy of Sacramento Peak Observatory).



REPRODUCIBILITY OF THE  
ORIGINAL PAGE IS POOR

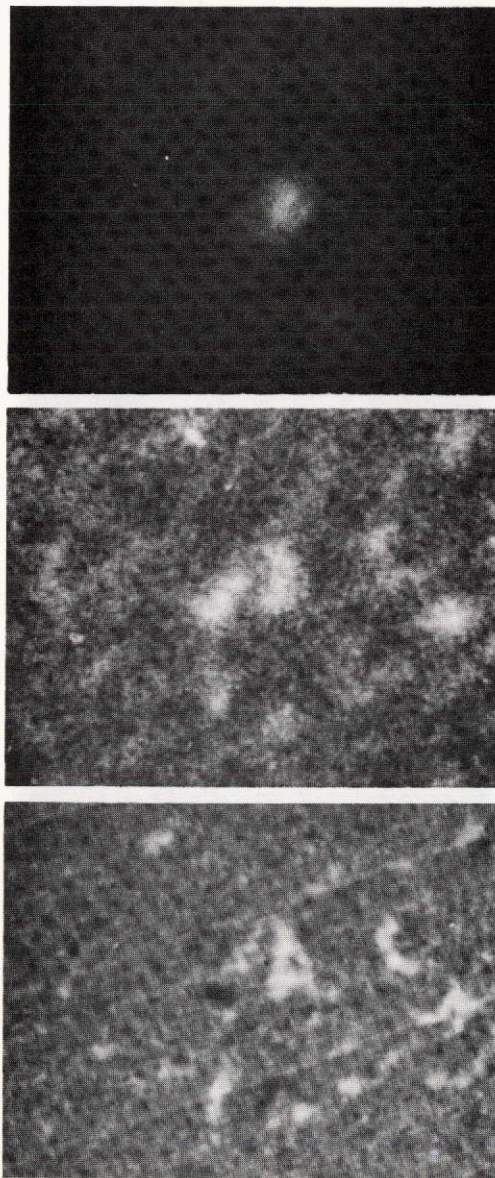


Figure 13 - An X-ray 'bright point' in the quiescent corona and the underlying structures in CaK (courtesy of Sacramento Peak Observatory) and the photospheric magnetic field (Kitt Peak National Observatory).

REPRODUCIBILITY OF THE  
ORIGINAL PAGE IS POOR

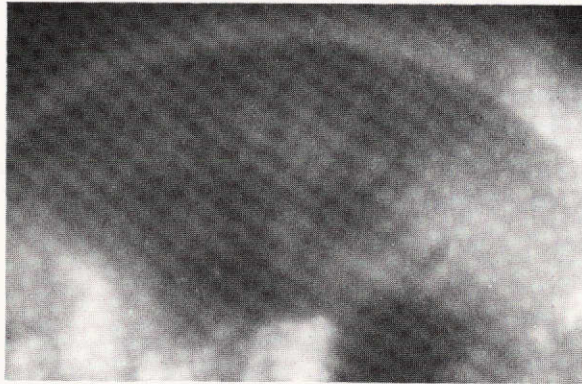


Figure 14 - A quiescent filament in the northern hemisphere observed on November 24, 1970 in (top) 3 - 35 Å, 44 - 51 Å X-rays and (bottom) H $\alpha$  (Sacramento Peak Observatory).



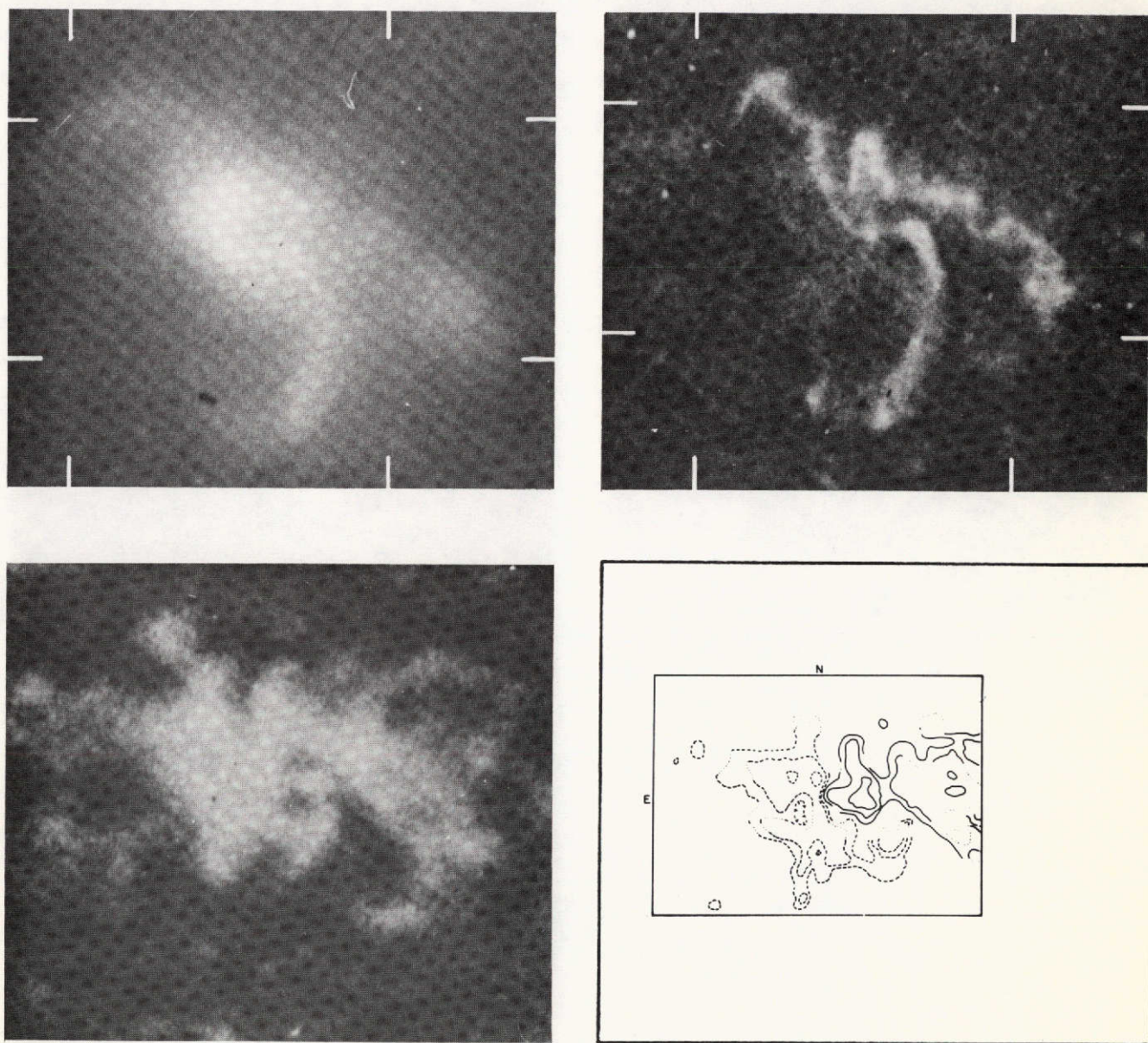


Figure 15 - Appearance of the solar flare of June 8, 1968 (1742 UT) in X-rays, H $\alpha$  and CaK and the magnetic configuration at the time of the flare. Top left: 3 - 18 Å X-rays. Top right: H $\alpha$  (courtesy of NOAA



REPRODUCIBILITY OF THE  
ORIGINAL PAGE IS POOR

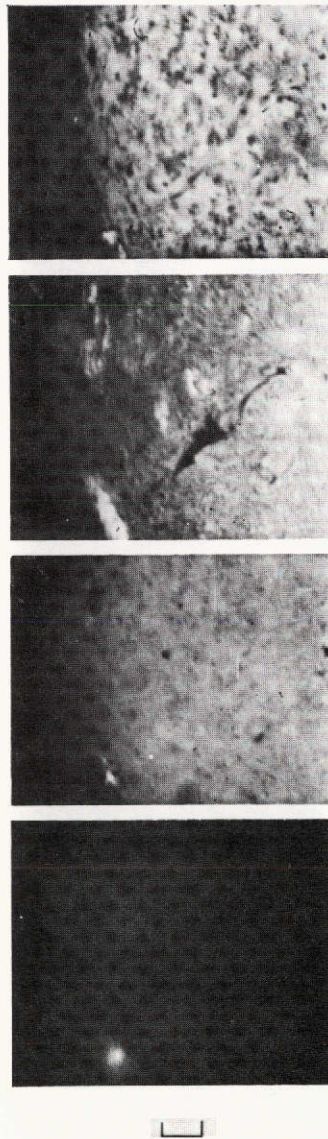


Figure 16 - The appearance of the solar flare of November 4, 1969 in  $H\alpha$  and X-rays. Top to bottom: Red wing  $H\alpha$ ,  $H\alpha$  on band, Blue wing, 3-12 Å X-rays. The photographs were taken at about 2030 UT. The  $H\alpha$  photographs were provided by H. Zirin, California Institute of Technology. The bracket below the photographs is one arc minute in length.

REPRODUCIBILITY OF THE  
ORIGINAL PAGE IS POOR

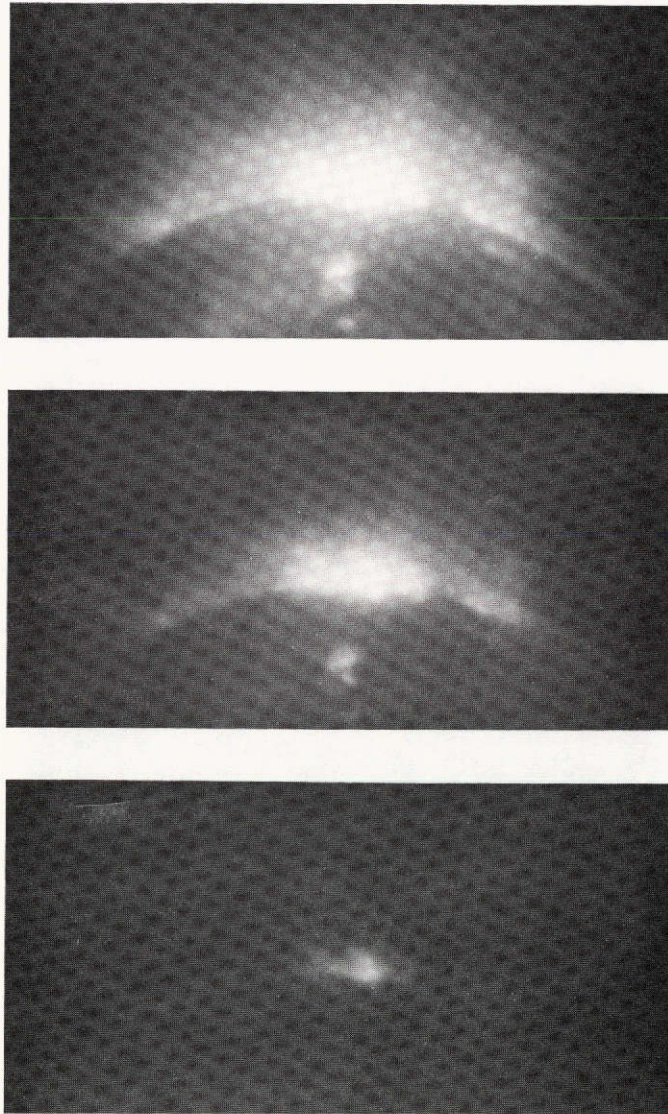


Figure 17 - X-ray images of the coronal active region above McMath plage 11035. Top: Photograph through a thin organic filter passing the bands  $3 - 35 \text{ \AA}$  and  $44 - 51 \text{ \AA}$ . Middle: Photograph through a thin beryllium filter passing the band  $3 - 18 \text{ \AA}$ . Bottom: Photograph through a thicker beryllium filter ( $3 - 12 \text{ \AA}$ ).

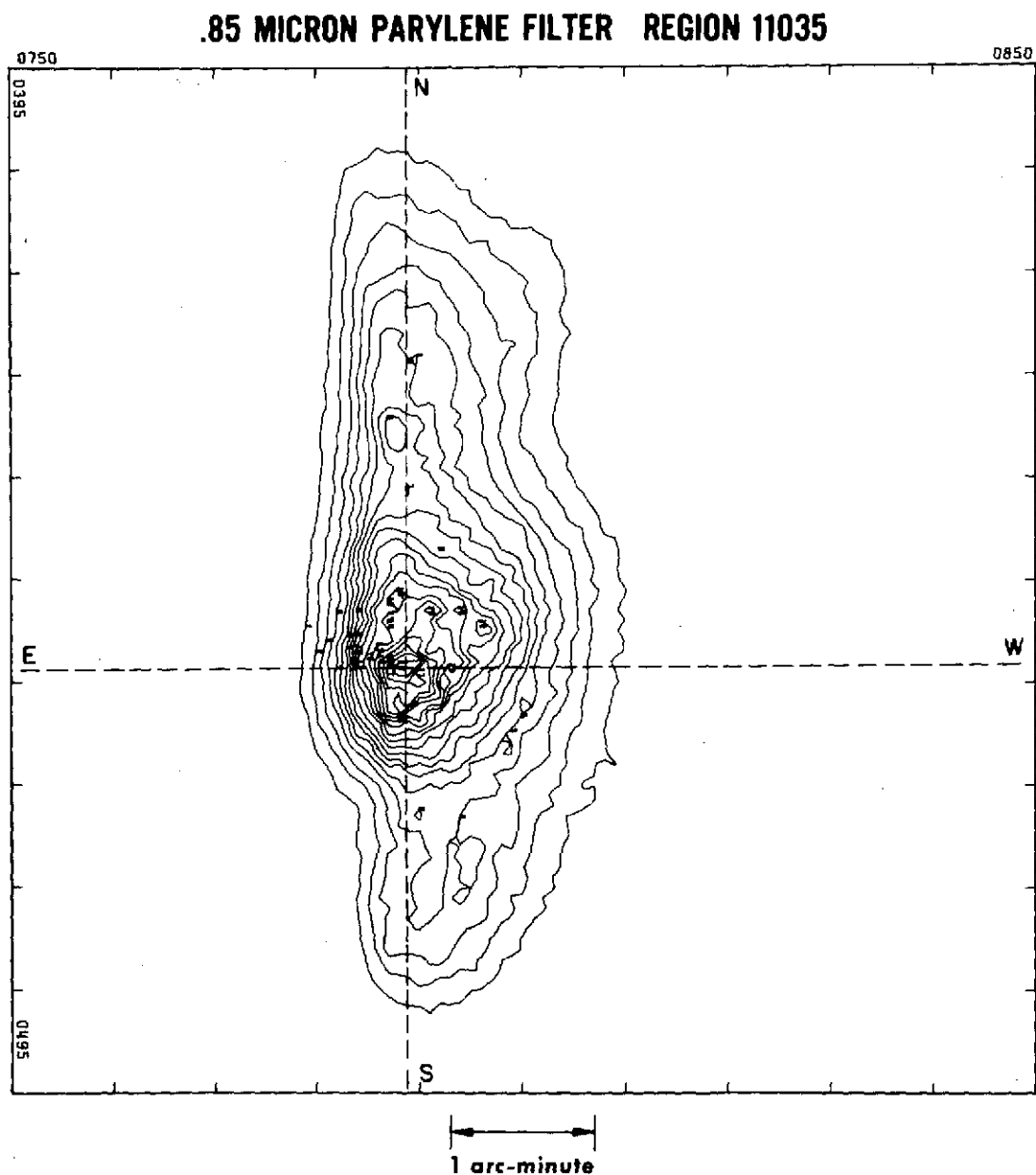


Figure 18 - A contour map of the energy deposited in the film plane made from the upper photograph of Figure 17. The isophotes represented linear energy intervals. The dashed lines labeled N-S and E-W are tangential and radial to the limb respectively through the point of maximum brightness.

REGION 11035 EAST TO WEST

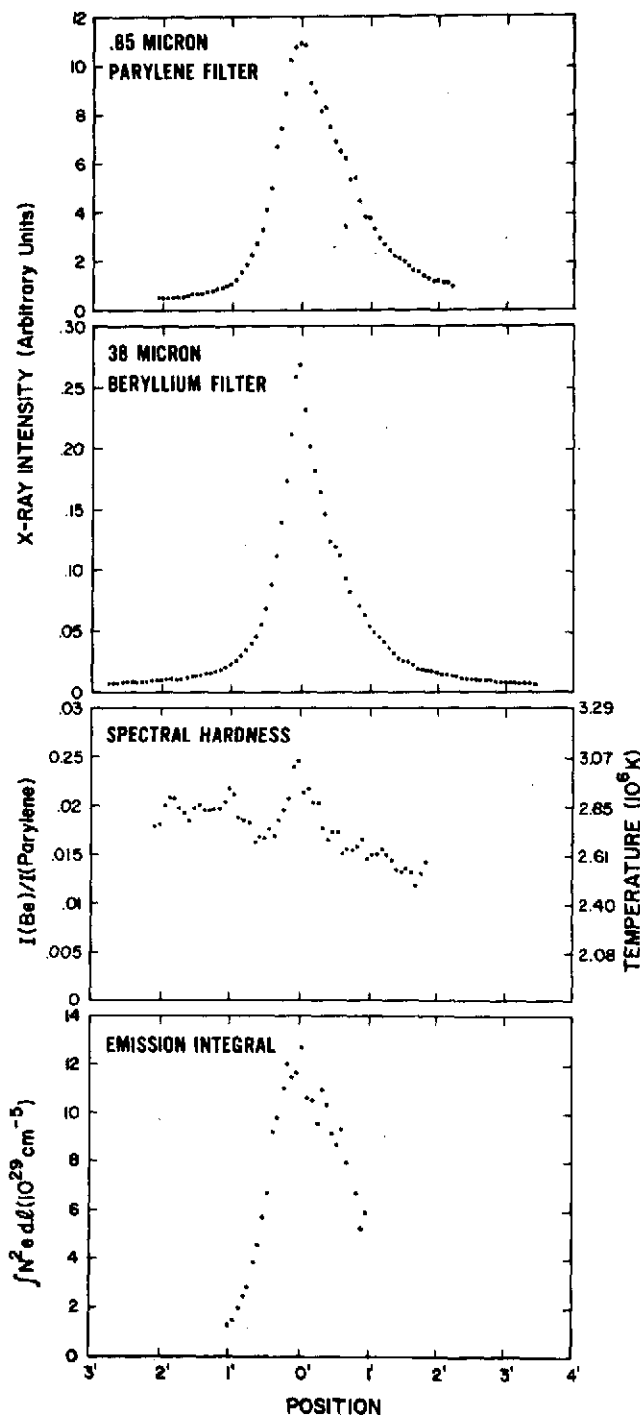


Figure 19 - The radial scan line through the peak of region 11035. (a) X-ray intensity through the thin organic filter. (b) X-ray intensity through the beryllium filter. (c) Spectral hardness at each point along the scan line. The small peaks at 1 and 2 arc minutes from the brightest point are probably statistical fluctuations, but the peak in spectral hardness at the brightest point is statistically significant. (d) The emission integral along the line of sight computed from the spectral hardness data and the intensities through the organic filter according to the formula of equation (2).



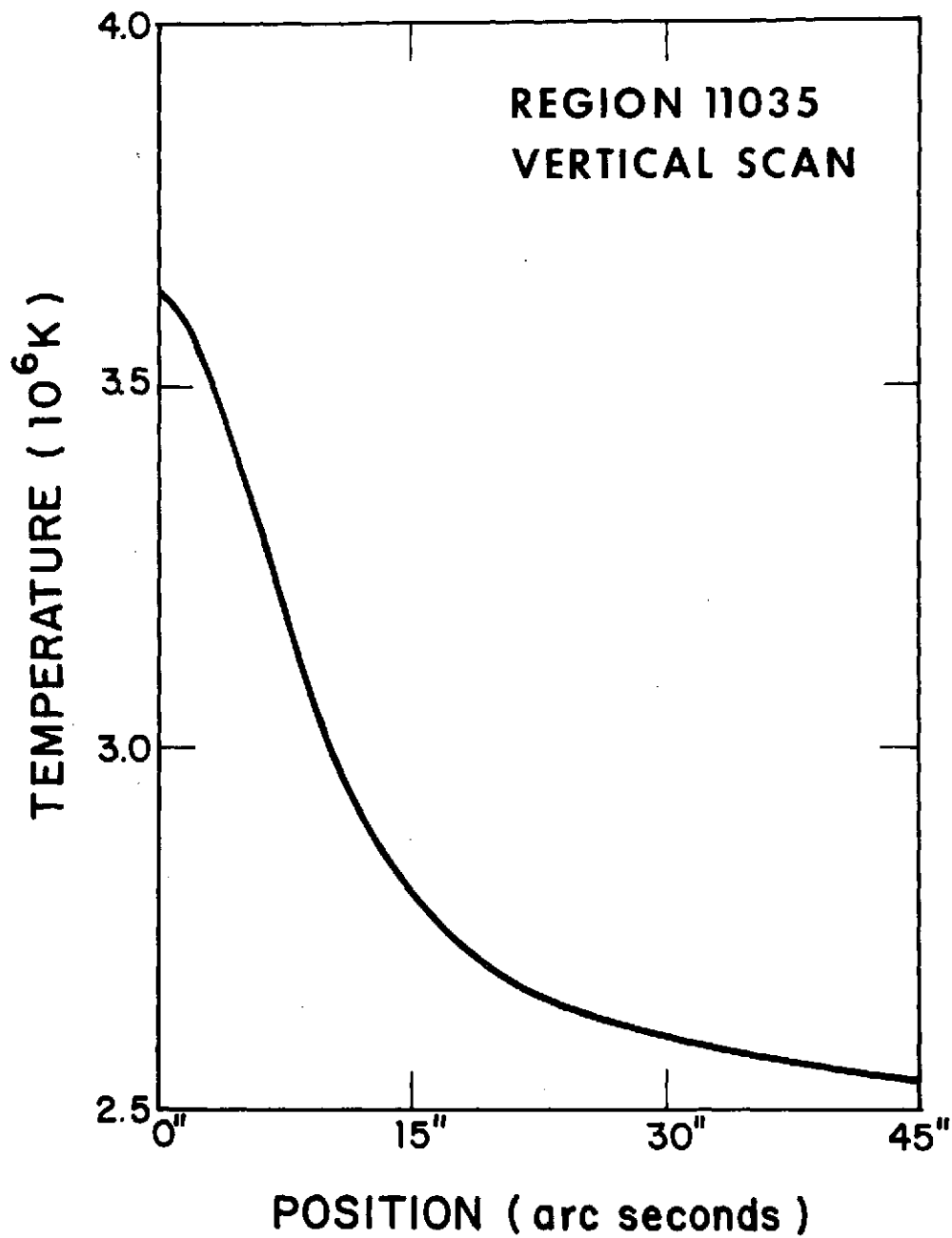


Figure 20 - Electron temperature as a function of position for region 11035 computed by inverting the data of Figure 19 (a) and (b) under the assumption of spherical symmetry. The temperature decreases only slightly beyond 20 arc-seconds from the center of the region.

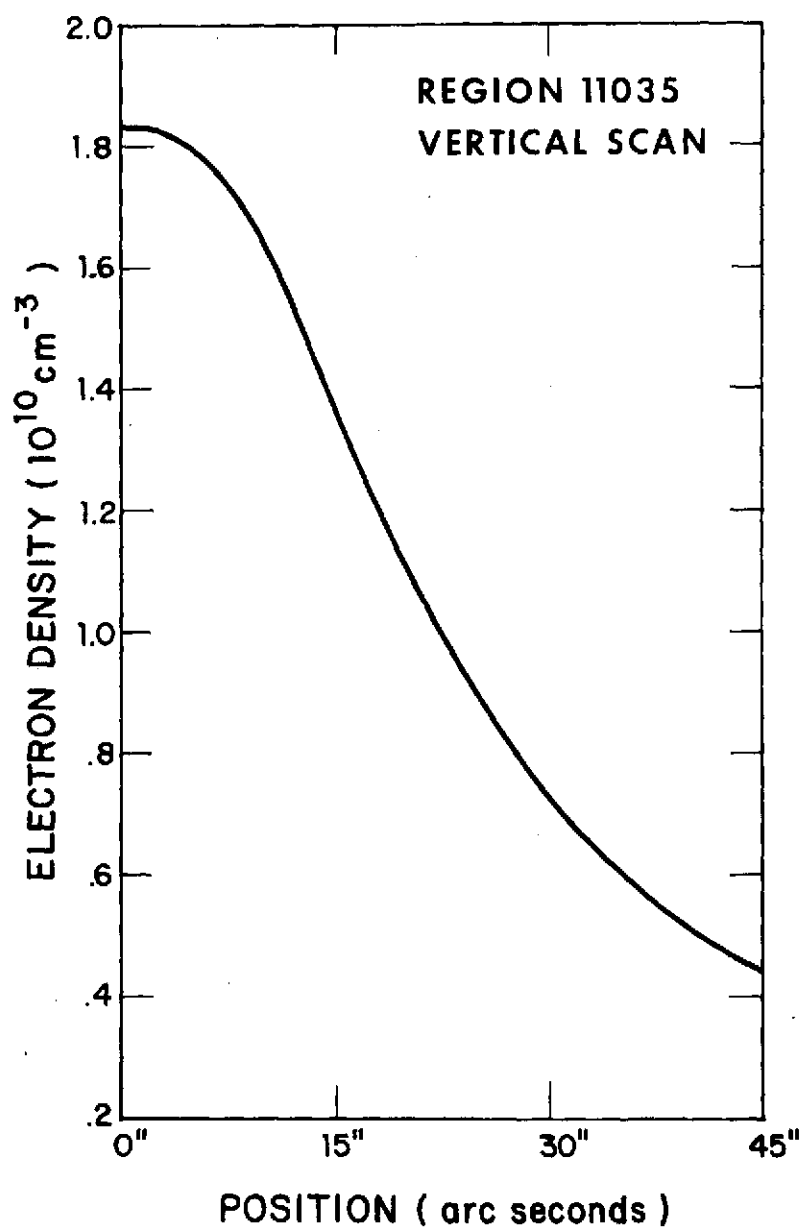


Figure 21 - Electron density as a function of position for region 11035.

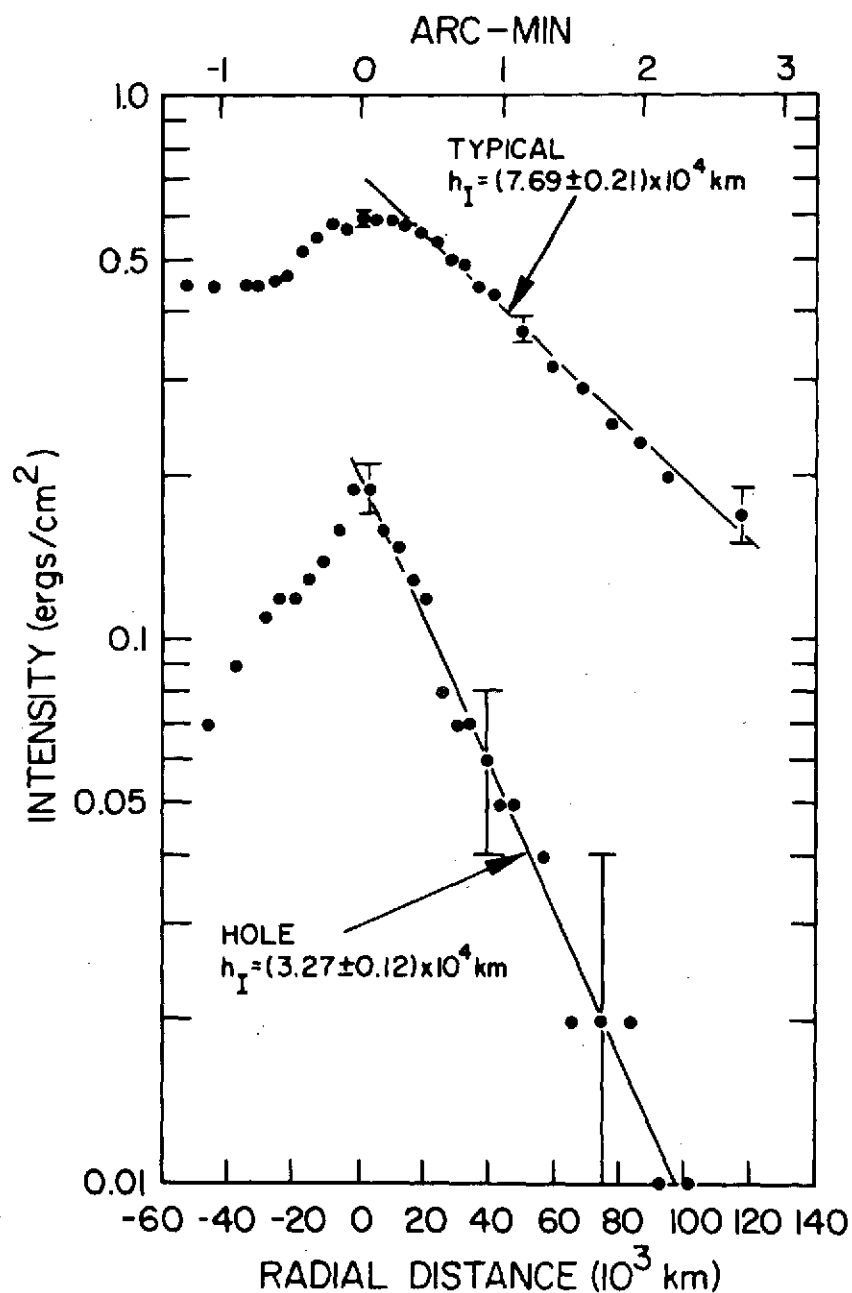


Figure 22 - Graph of X-ray intensity as a function of radial position for the coronal hole and for a typical closed region (November 24, 1970, 3 - 25 Å and 44 - 51 Å bandpass). The error brackets on the points represent the second to least significant bit of the microdensitometer. The data is quantitized at the lowest levels. For each plot the intensity scale height  $h_I$  is determined from a least squares fit to the data.



REPRODUCIBILITY OF THE  
ORIGINAL PAGE IS POOR

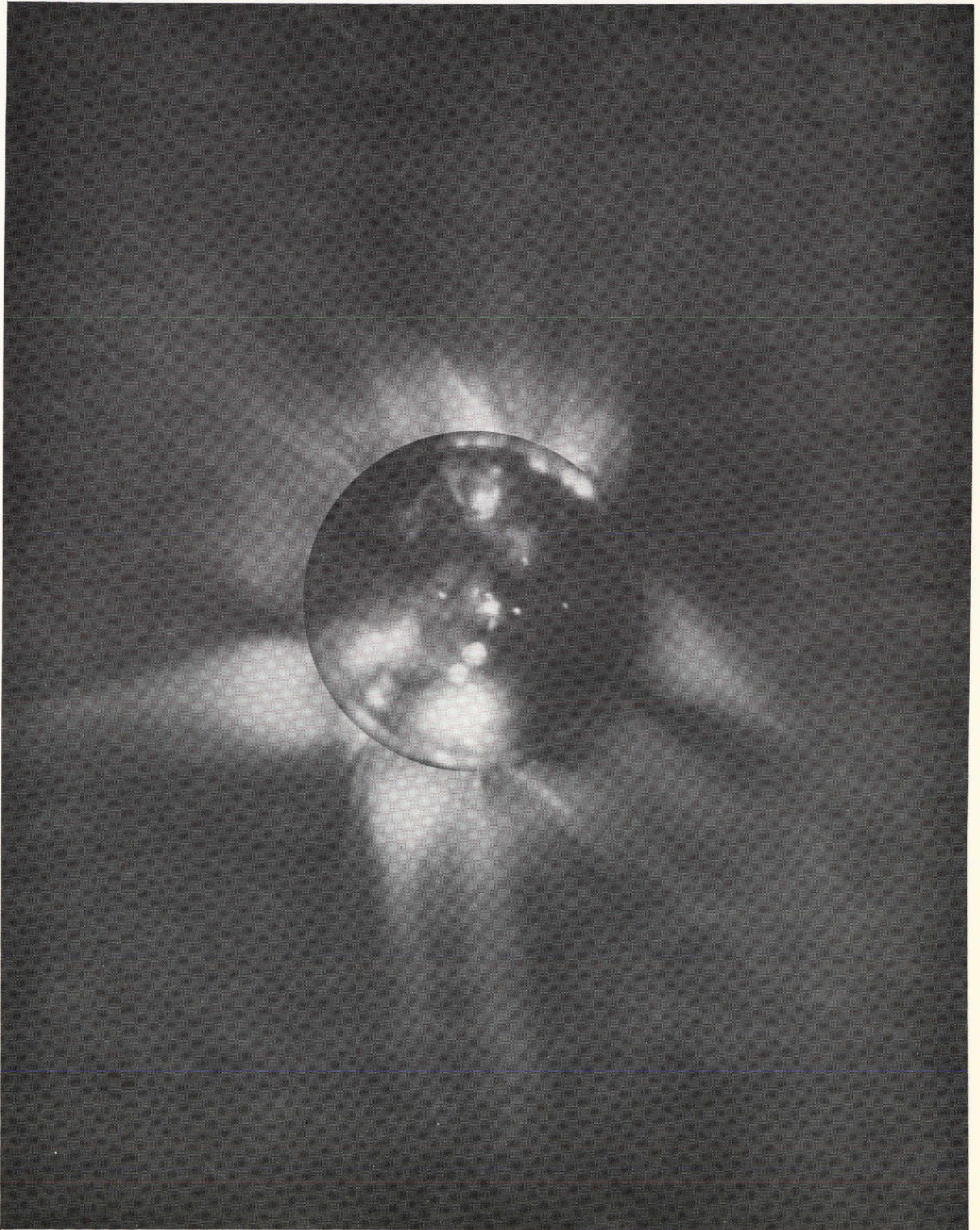




Figure 23 - A composite print of the solar corona on March 7, 1970 composed of an X-ray exposure in the 3 - 36 Å, 44 - 64 Å wavebands and the radial density gradient filter white light exposure of Newkirk and Lacey (1970). There is a one-to-one correspondence between the position of the bases of white light coronal structures and regions of enhanced limb brightening in the X-ray image.

## APPENDIX B

TABLE I

8 June 1968 Aerobee Rocket Flight

Films and Filters

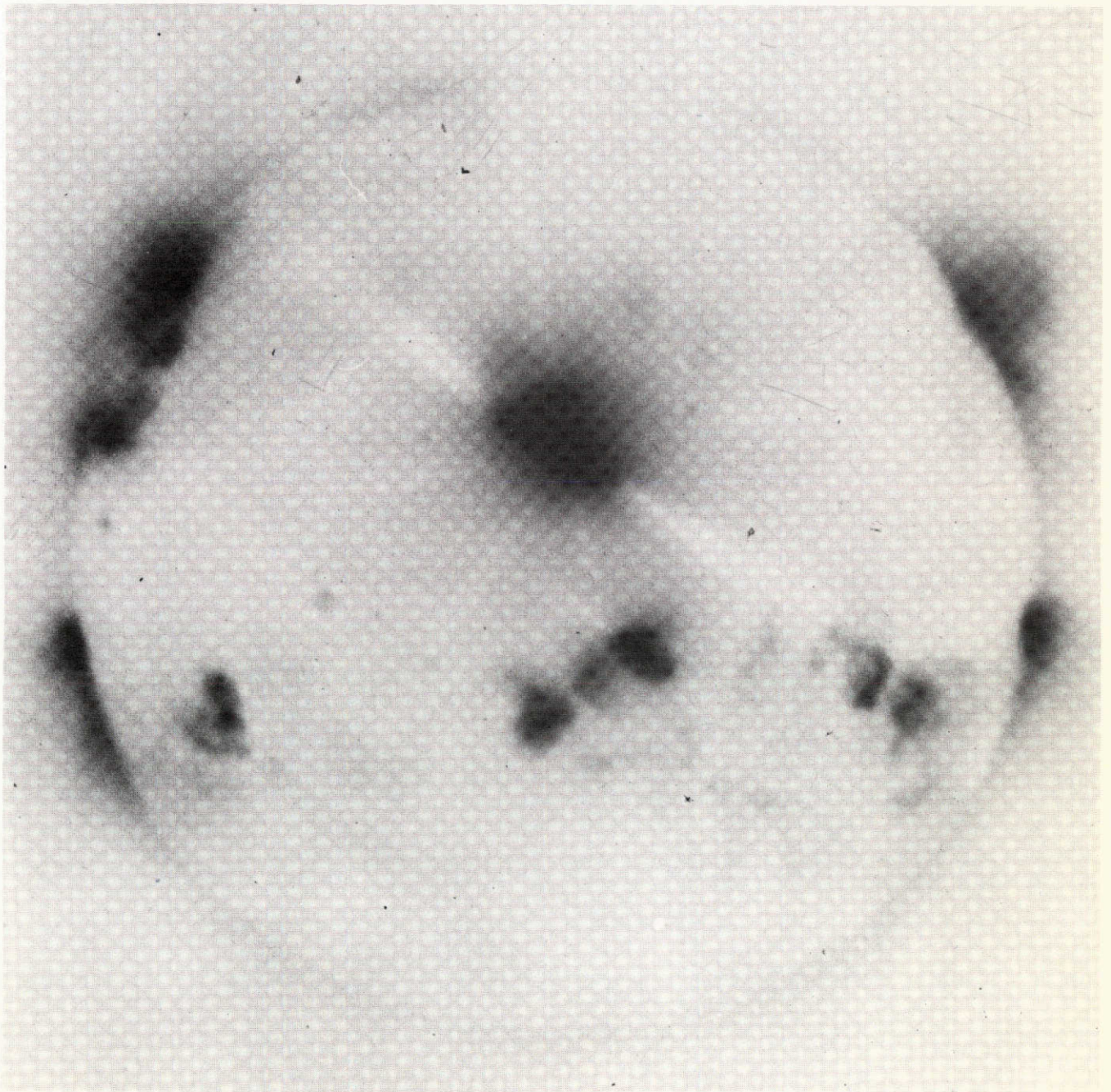
<u>Nominal Exposure Time (sec)</u>	<u>Nominal Passband</u>	<u>Nominal Filter Thickness</u>	<u>Filter Material</u>	<u>Film</u>
6	3-18, 44-51 $\text{\AA}$	4.0 $\mu$	Mylar + Al <sup>1</sup>	Pan-X un-Tc <sup>2</sup>
6	3-18, 44-51	4.0	Mylar + Al	Ilford Special <sup>3</sup>
22	3-18	10.2	Beryllium	103-0 un-Tc
19	3-18	10.2	Beryllium	Pan-X un-Tc
6	3-18	10.2	Beryllium	Pan-X Tc
2	3-18	10.2	Beryllium	Pan-X Tc
52	3-18	10.2	Beryllium	103-0 un-Tc <sup>3</sup>
22	3-18	10.2	Beryllium	103-0 un-Tc <sup>3</sup>
6	3-18	10.2	Beryllium	103-0 un-Tc <sup>3</sup>
2	3-12	51	Beryllium	Pan-X Tc
18		2.5	Steel	103-0 un-Tc
2	4000-7000	White Light		Pan-X Tc

1 The Mylar filters consisted of 3.8 $\mu$  Mylar and 0.2 $\mu$  Aluminum

2 "Tc" and "un-Tc" are with or without a protective "topcoat" gelatin layer

3 Exposures made with the transmission grating.

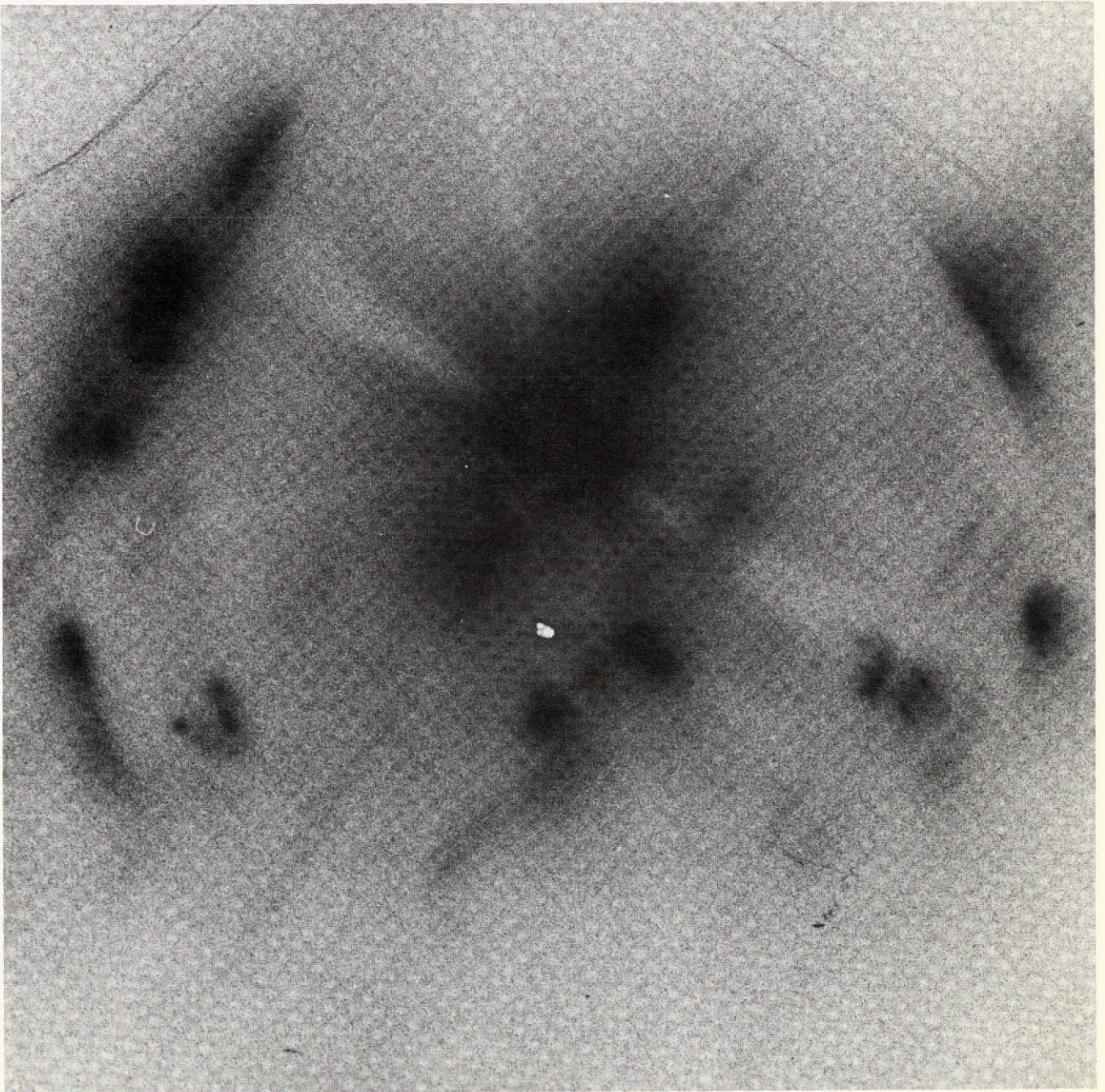
REPRODUCIBILITY OF THE  
ORIGINAL PAGE IS POOR



0.2MY/UTC PAN-X/DZ065



REPRODUCIBILITY OF THE  
ORIGINAL PAGE IS POOR



0.2MY+G/ILSPEC/DZ068



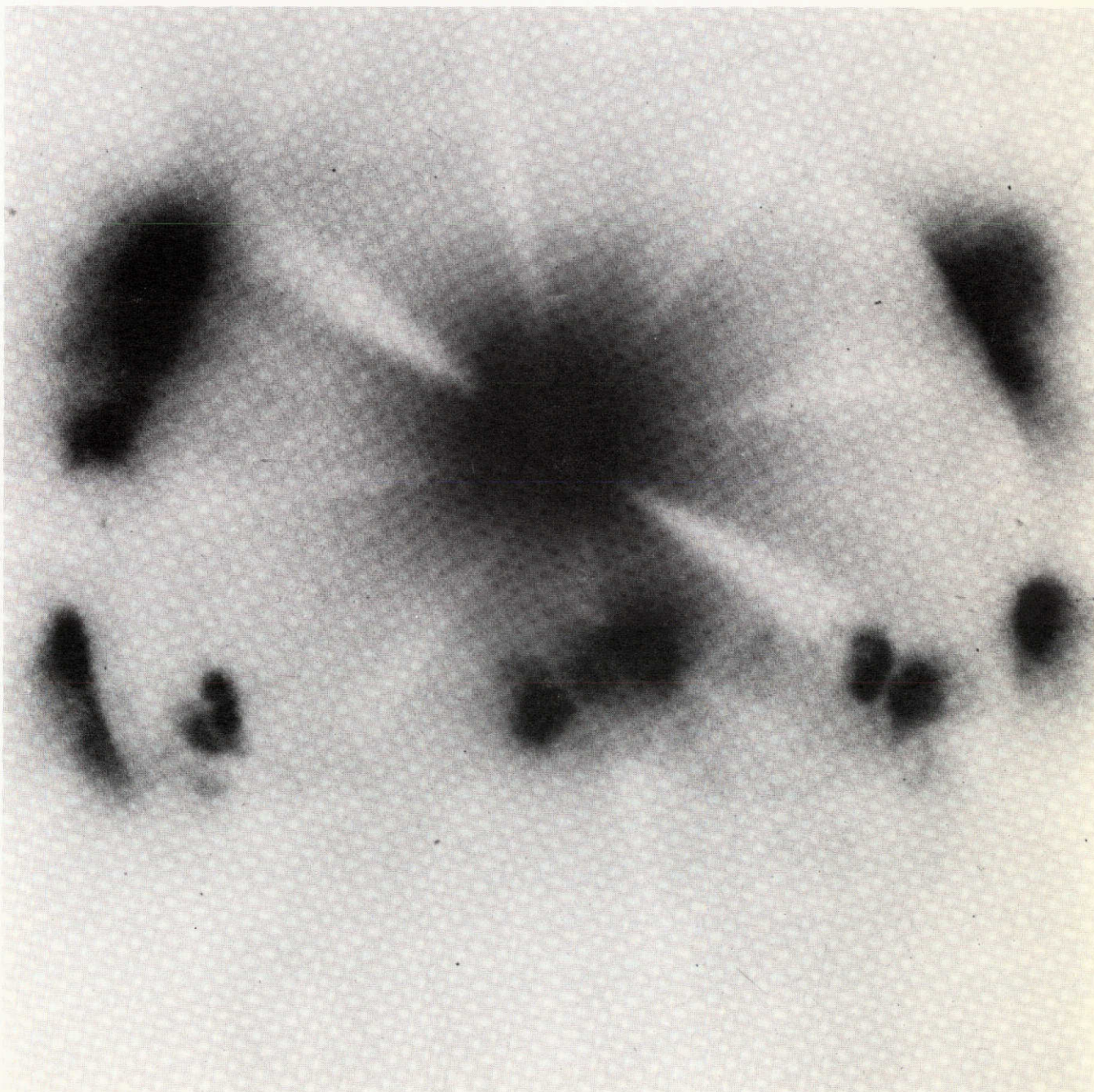
REPRODUCIBILITY OF THE  
ORIGINAL PAGE IS POOR



0.5BE/UTC 103-0/DZ060

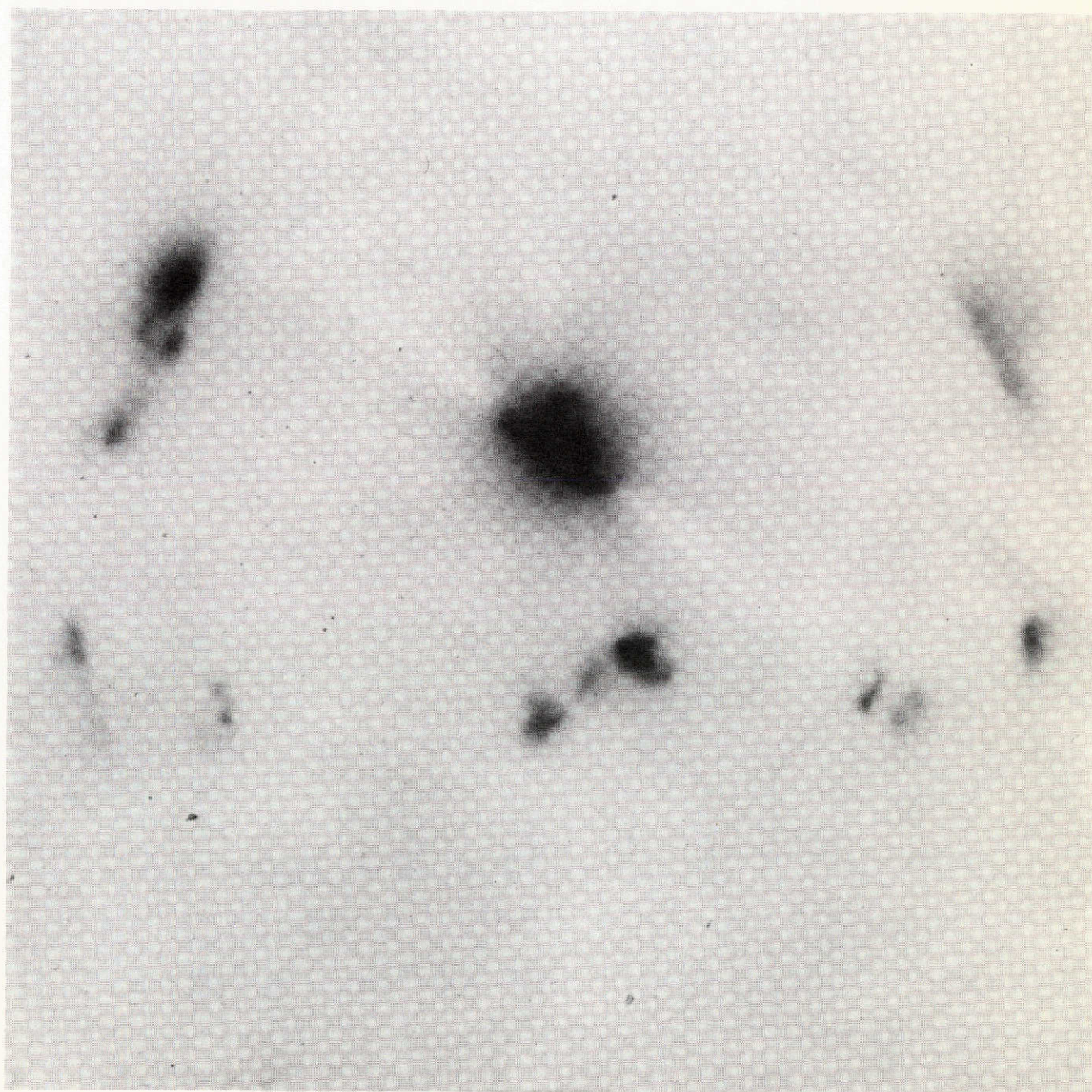


REPRODUCIBILITY OF THE  
ORIGINAL PAGE IS POOR



0.5BE/UTC PAN-X/DZ063

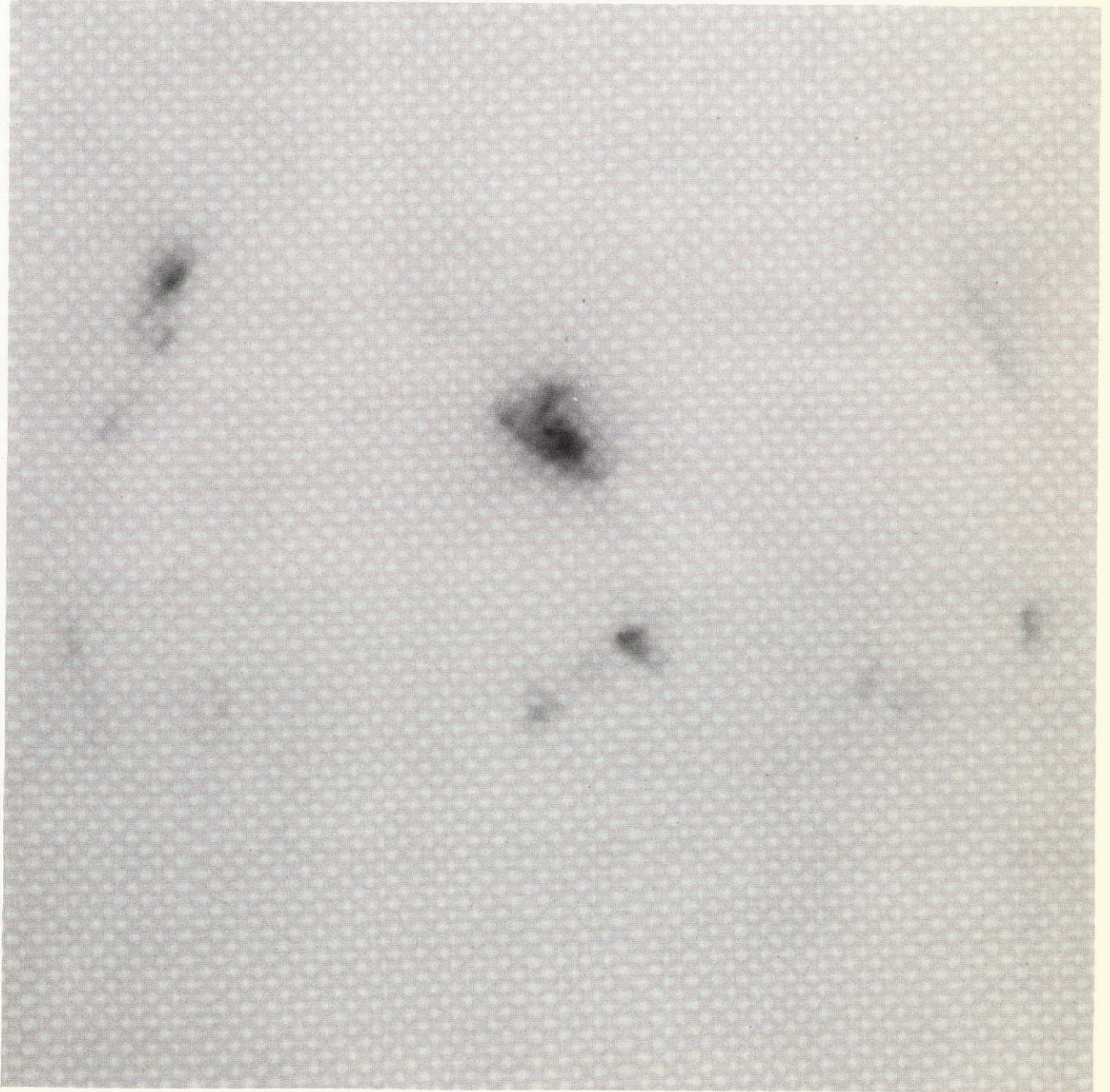




0.5BE/TC PAN-X/DZ062

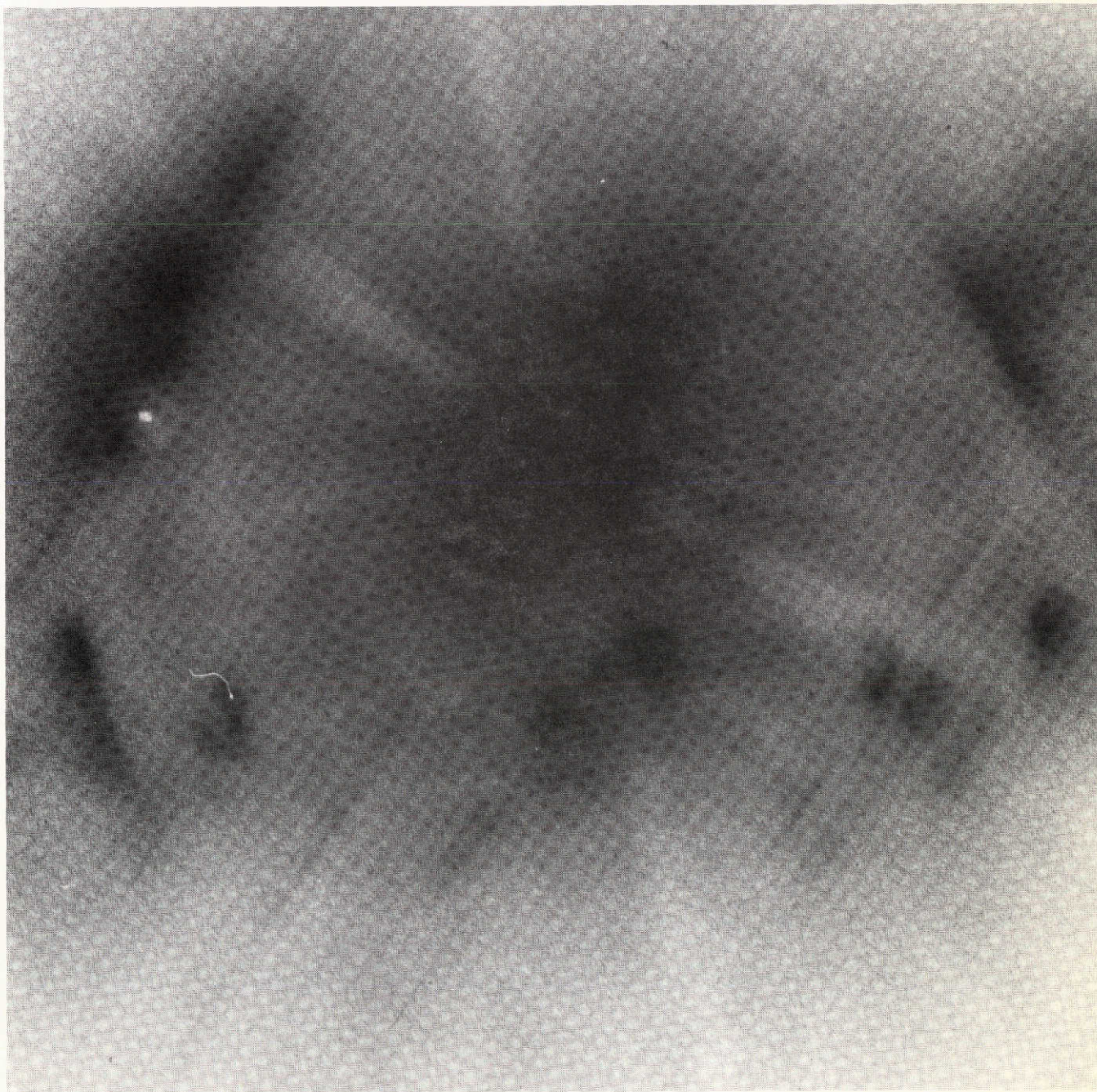


REPRODUCIBILITY OF THE  
ORIGINAL PAGE IS POOR



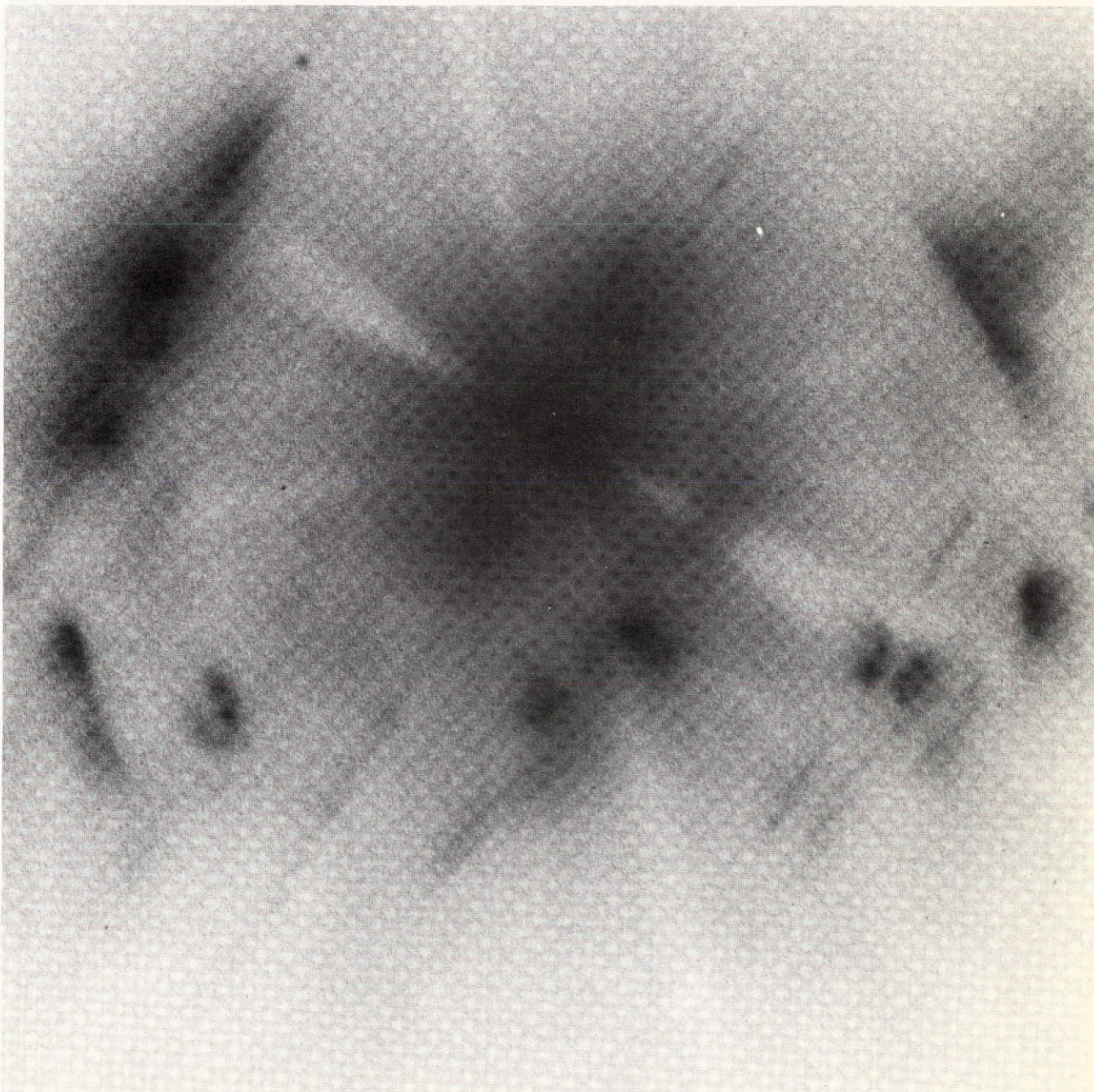
0.5BE/TC PAN-X/DZ064





0.5BE+G/UTC 103-0/DZ071

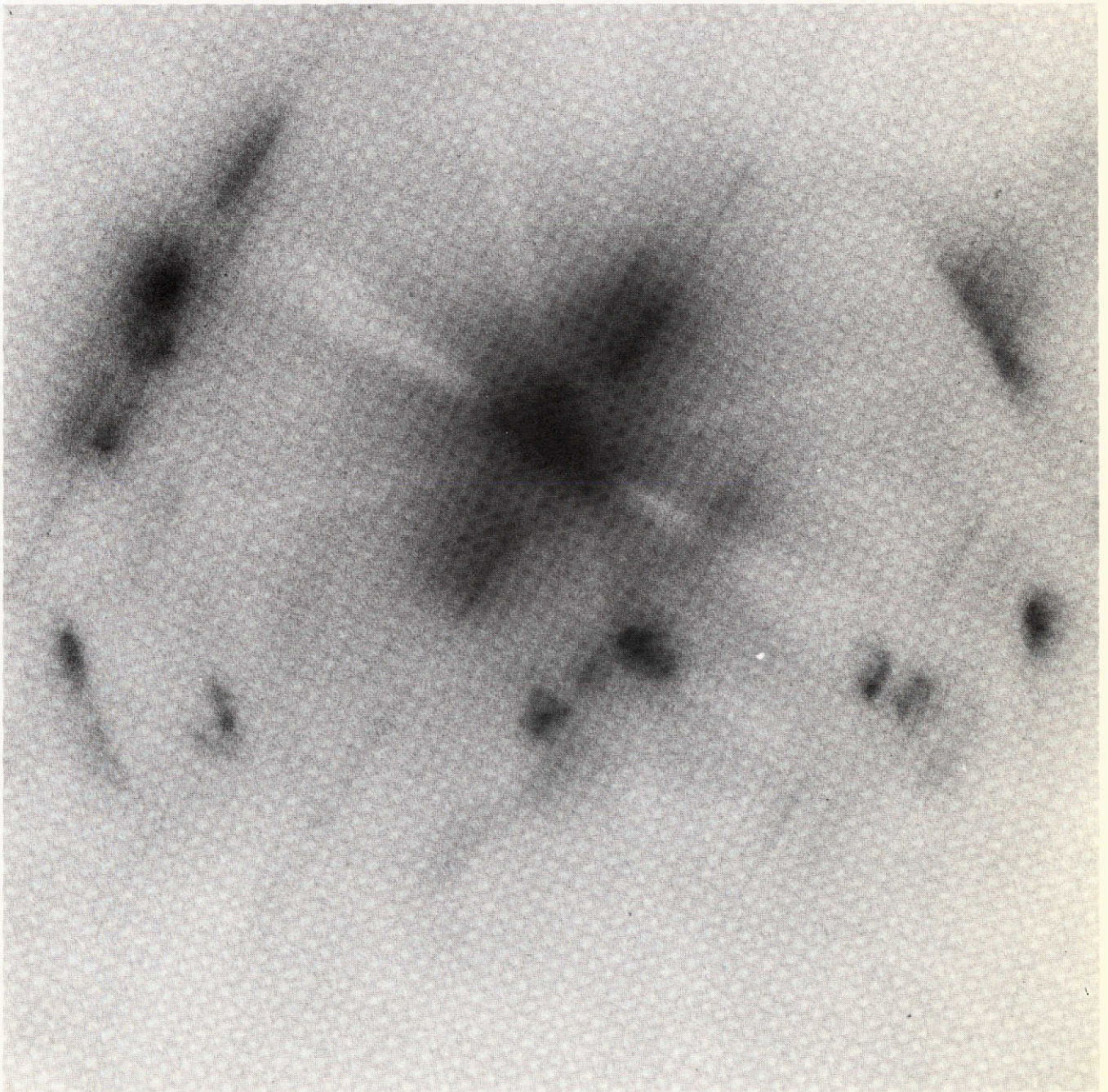




0.5BE+G/UTC 103-0/DZ070



REPRODUCIBILITY OF THE  
ORIGINAL PAGE IS POOR



0.5BE+G/UTC 103-0/DZ069



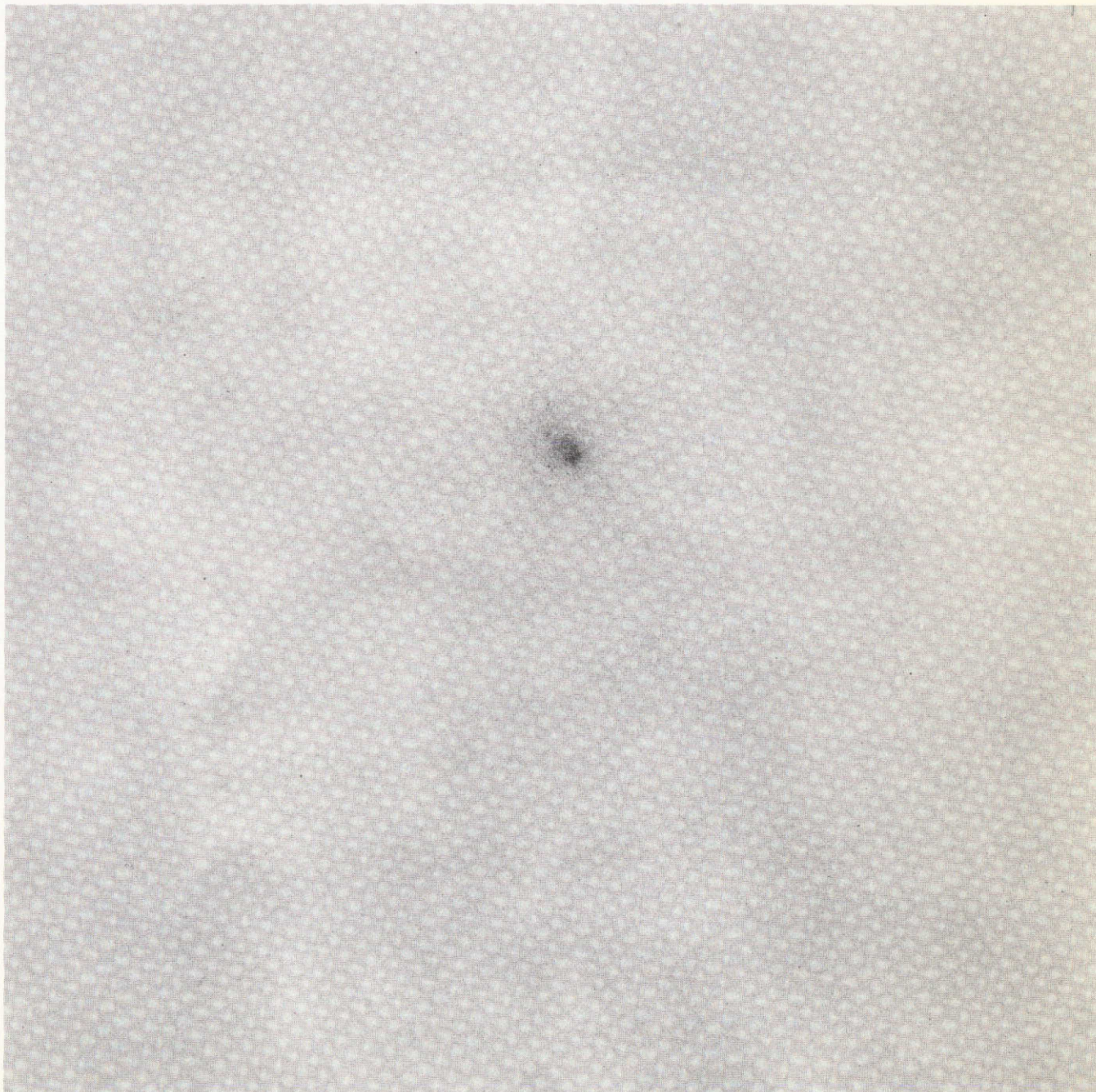
REPRODUCIBILITY OF THE  
ORIGINAL PAGE IS POOR



2.0BE/TC PAN-X/DZ061



REPRODUCIBILITY OF THE  
ORIGINAL PAGE IS POOR



0.1FE/UTC 103-0/DZ066

TABLE II

8 April 1969 Aerobee Rocket Flight

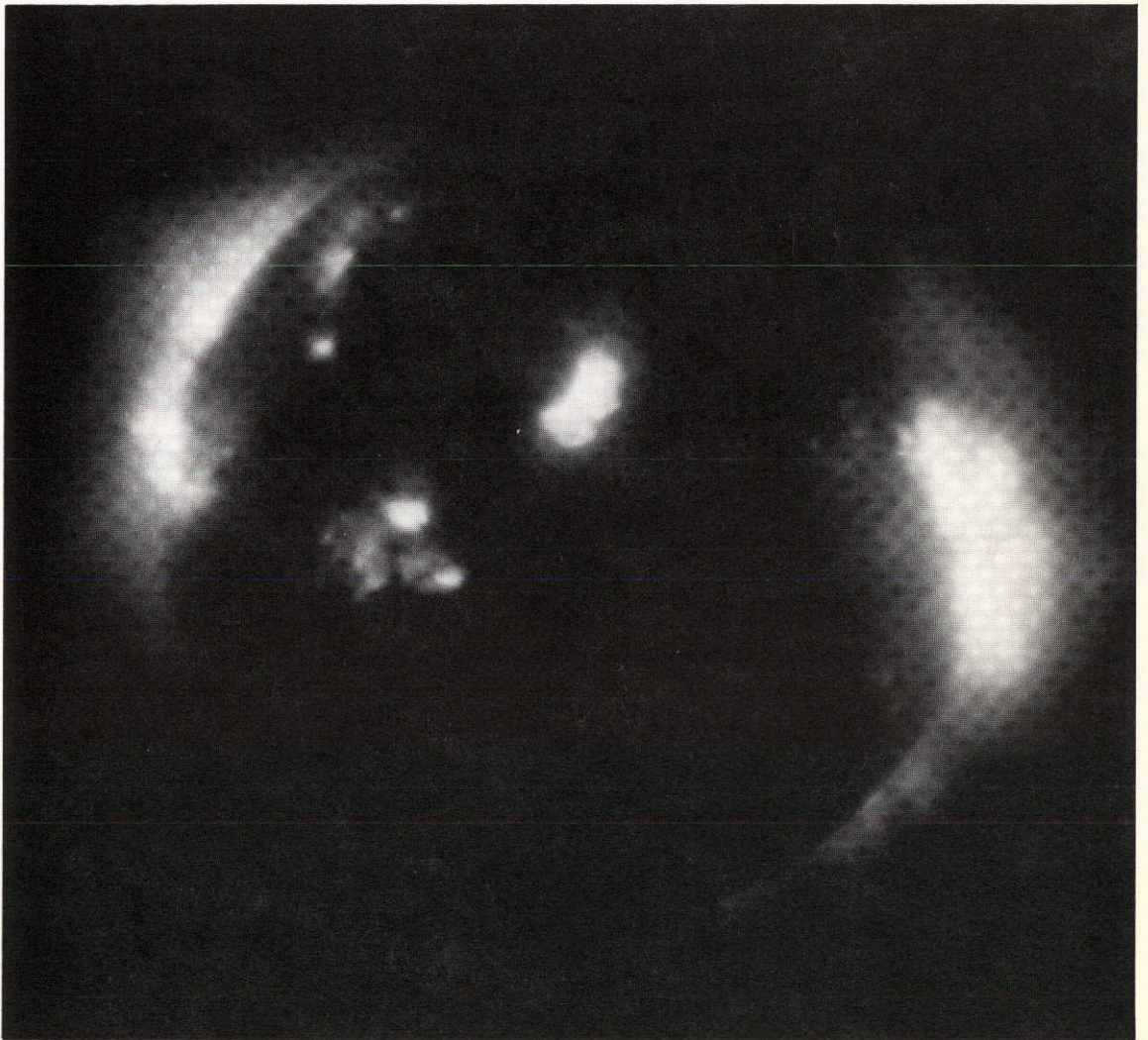
## Films and Filters

<u>Nominal Exposure Time (sec)</u>	<u>Nominal Passband</u>	<u>Nominal Filter Thickness</u>	<u>Filter Material</u>	<u>Film</u>
6	3-32, 44-47 <sup>0</sup>	1.3 $\mu$	Parylene-c +Al <sup>1</sup>	Pan-X un-Tc <sup>2</sup>
2	3-32, 44-47	1.3	Parylene-c +Al	Pan-X un-Tc <sup>3</sup>
25	3-32, 44-47	1.3	Parylene-c +Al	Pan-X un-Tc <sup>4</sup>
70	3-18, 44-46	4.1	Mylar + Al <sup>1</sup>	Pan-X un-Tc
12	3-18, 44-46	4.1	Mylar + Al	Pan-X un-Tc
6	3-18, 44-46	4.1	Mylar + Al	Pan-X un-Tc <sup>3</sup>
15	3-60	0.1	Al	Microfile
2	3-60	0.1	Al	Pan-X un-Tc
10	3-18	10.2	Beryllium	Pan-X un-Tc <sup>3</sup>
6	3-18	10.2	Beryllium	Pan-X Tc
2	3-18	10.2	Beryllium	Pan-X Tc
75	3-18	10.2	Beryllium	Pan-X Tc <sup>4</sup>
2	4000 - 7000		Neutral Density (White Light)	

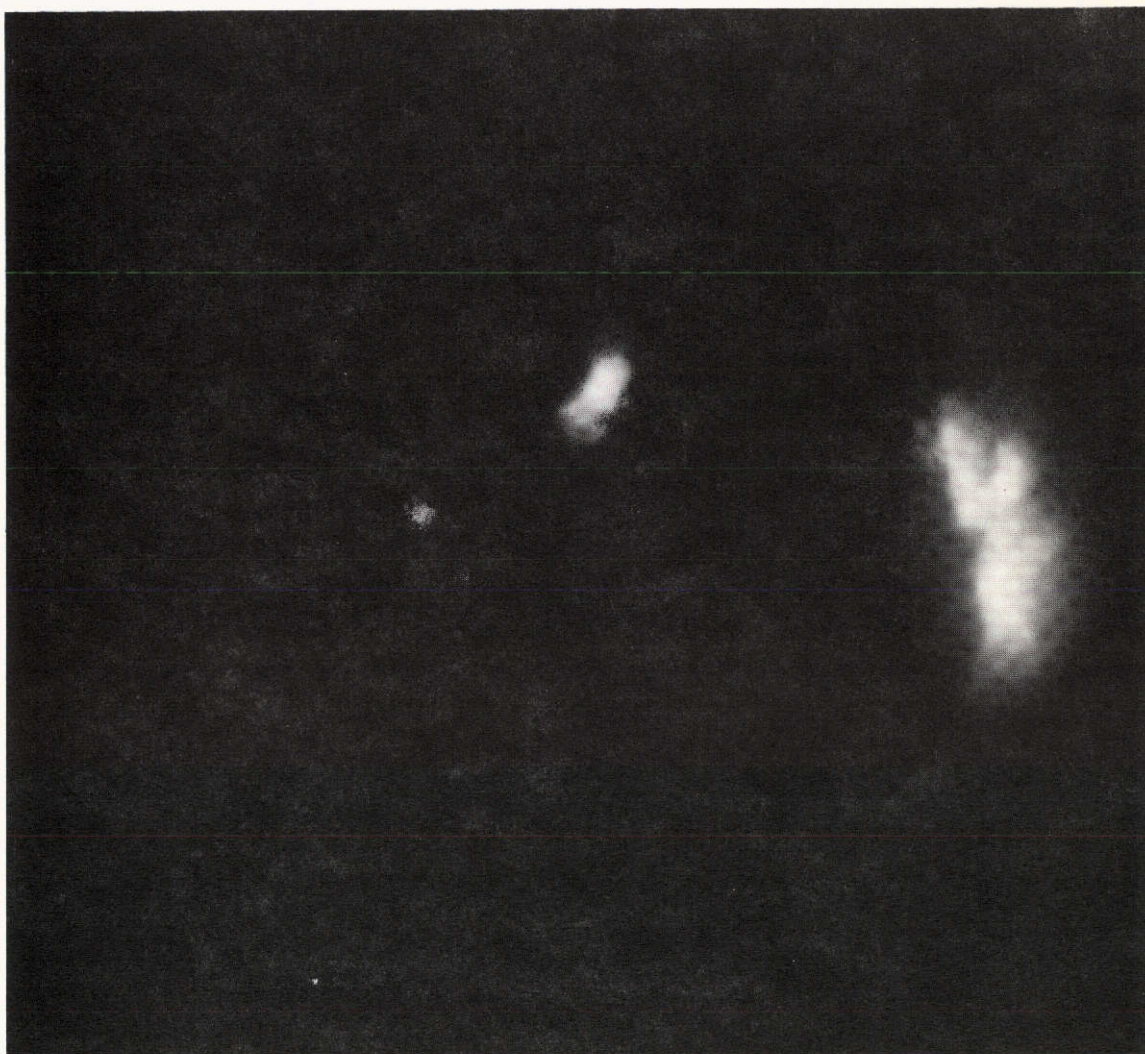
- 1 The Parylene and Mylar filters were coated with 0.3 $\mu$  Aluminum
- 2 "Tc" and "un-Tc" are with and without a protective "topcoat" gelatin layer
- 3 Telescope was offset pointed to the limb
- 4 Exposures made with the transmission grating



REPRODUCIBILITY OF THE  
ORIGINAL PAGE IS POOR

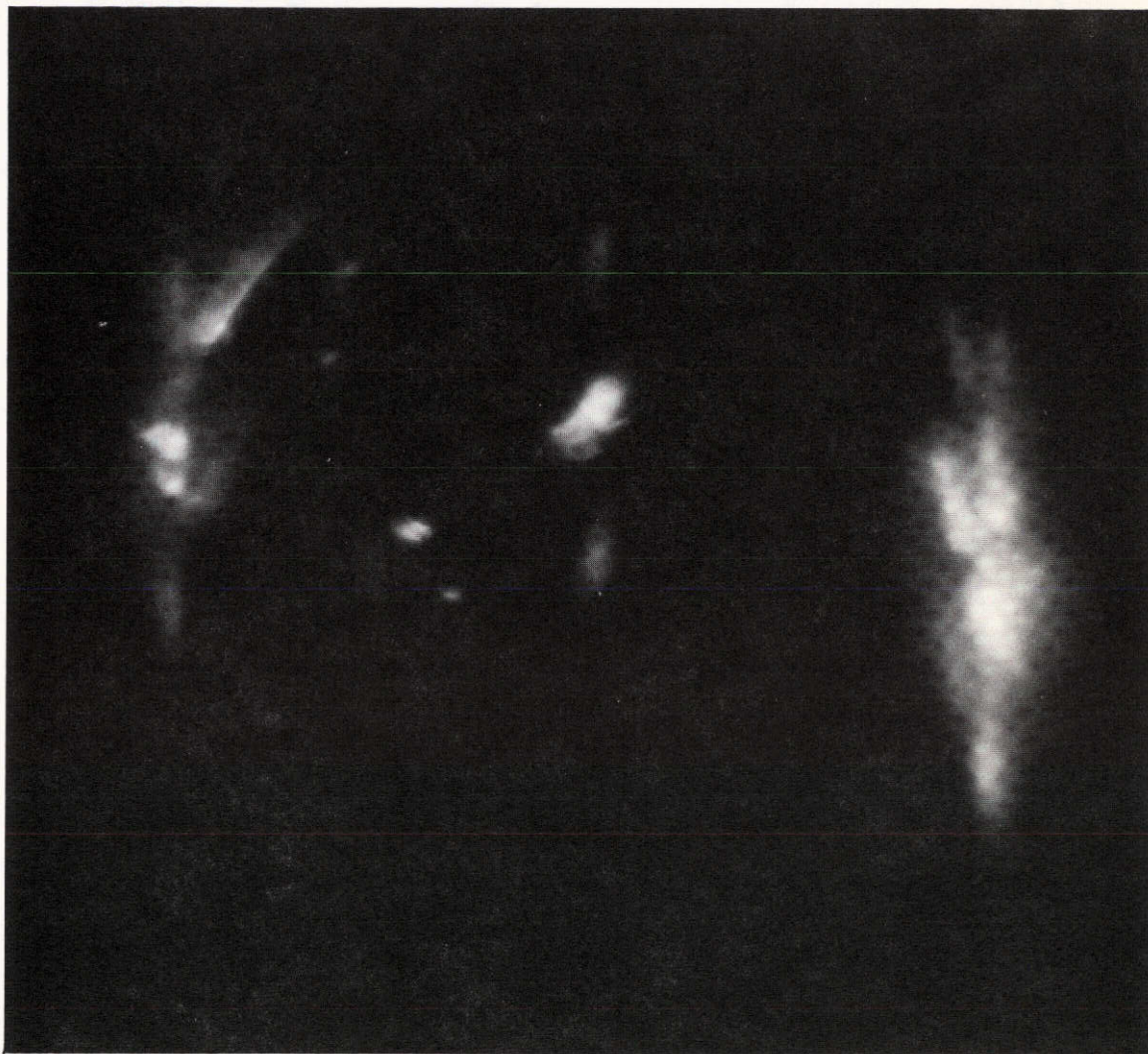


1.0PA+P/UTC PAN-X/EF009

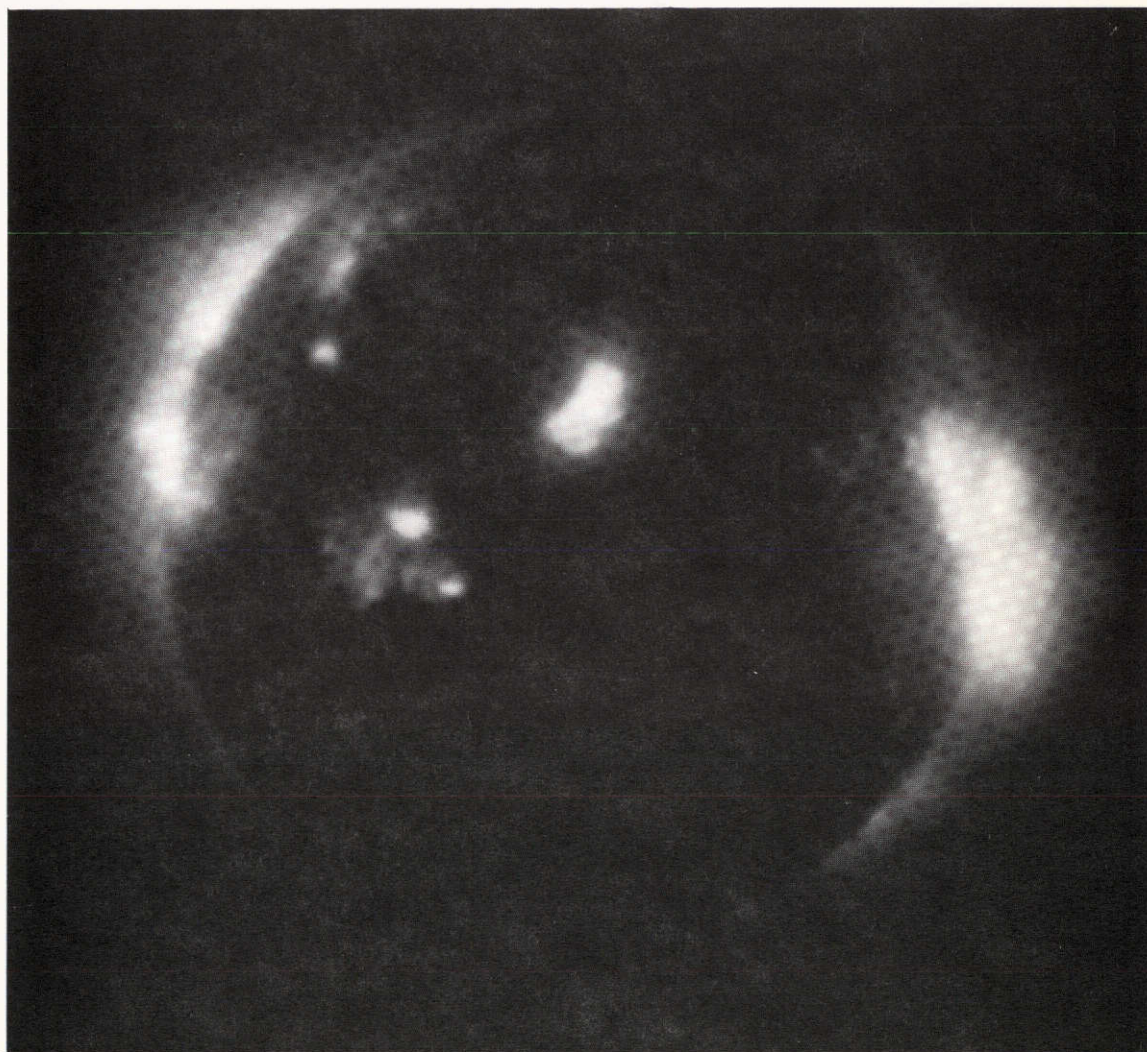


1.0PA+P/UTC PAN-X/EF003





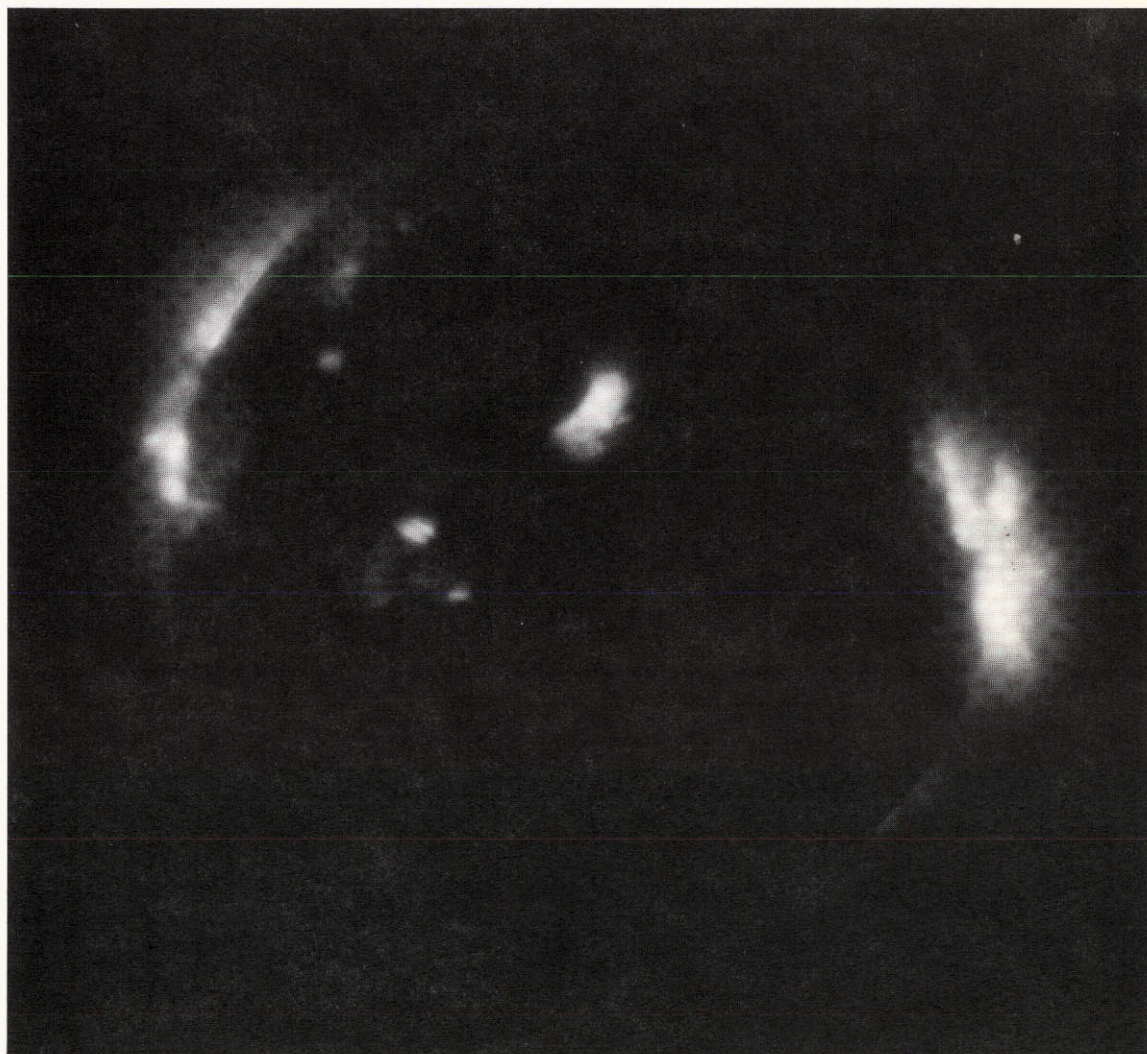
1.0PAR+G/UTC PAN-X/EF013



0.2MY+P/UTC PAN-X/EF011

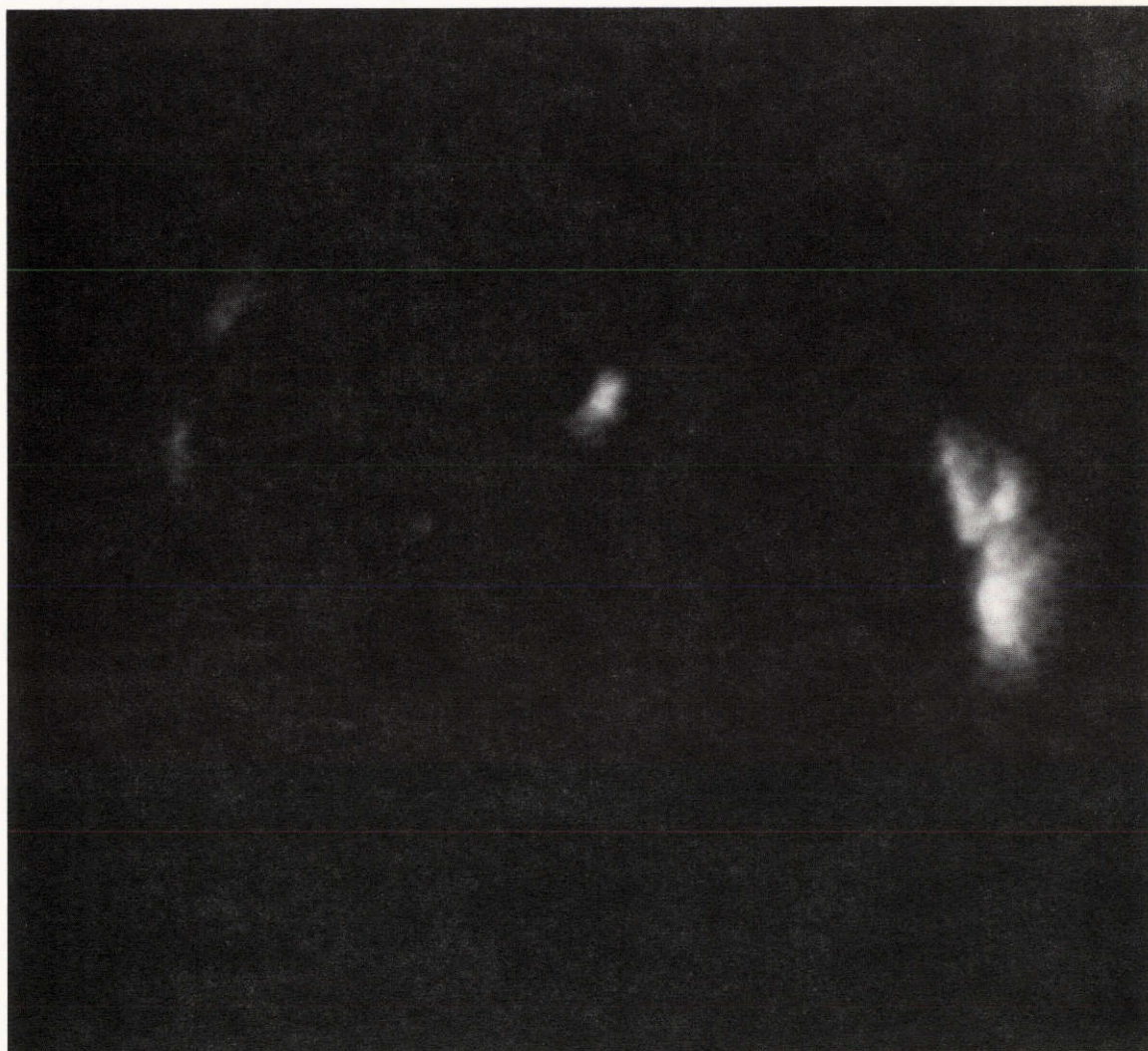
REPRODUCIBILITY OF THE  
ORIGINAL PAGE IS POOR





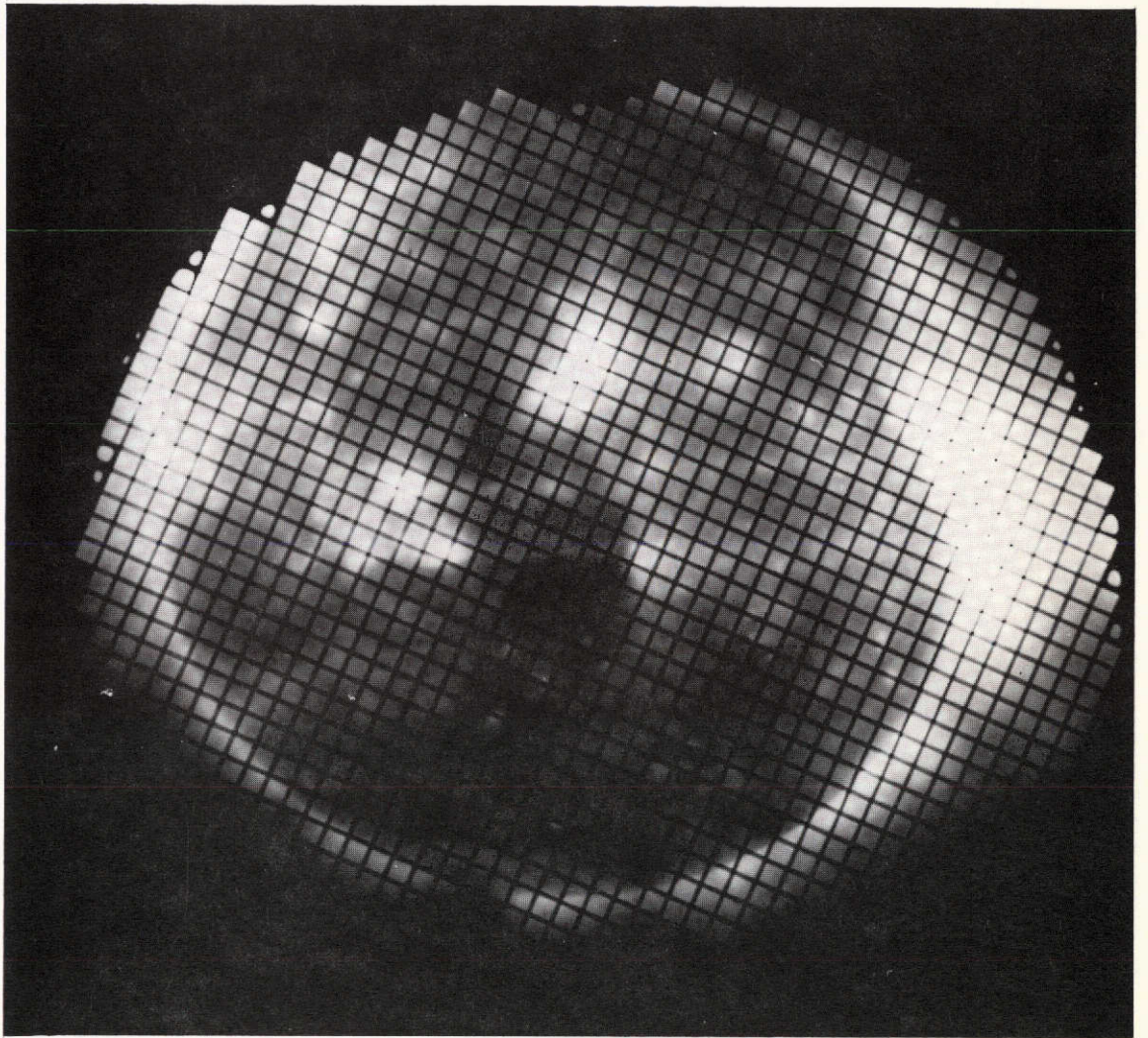
0.2MY+P/UTC PAN-X/EF-006





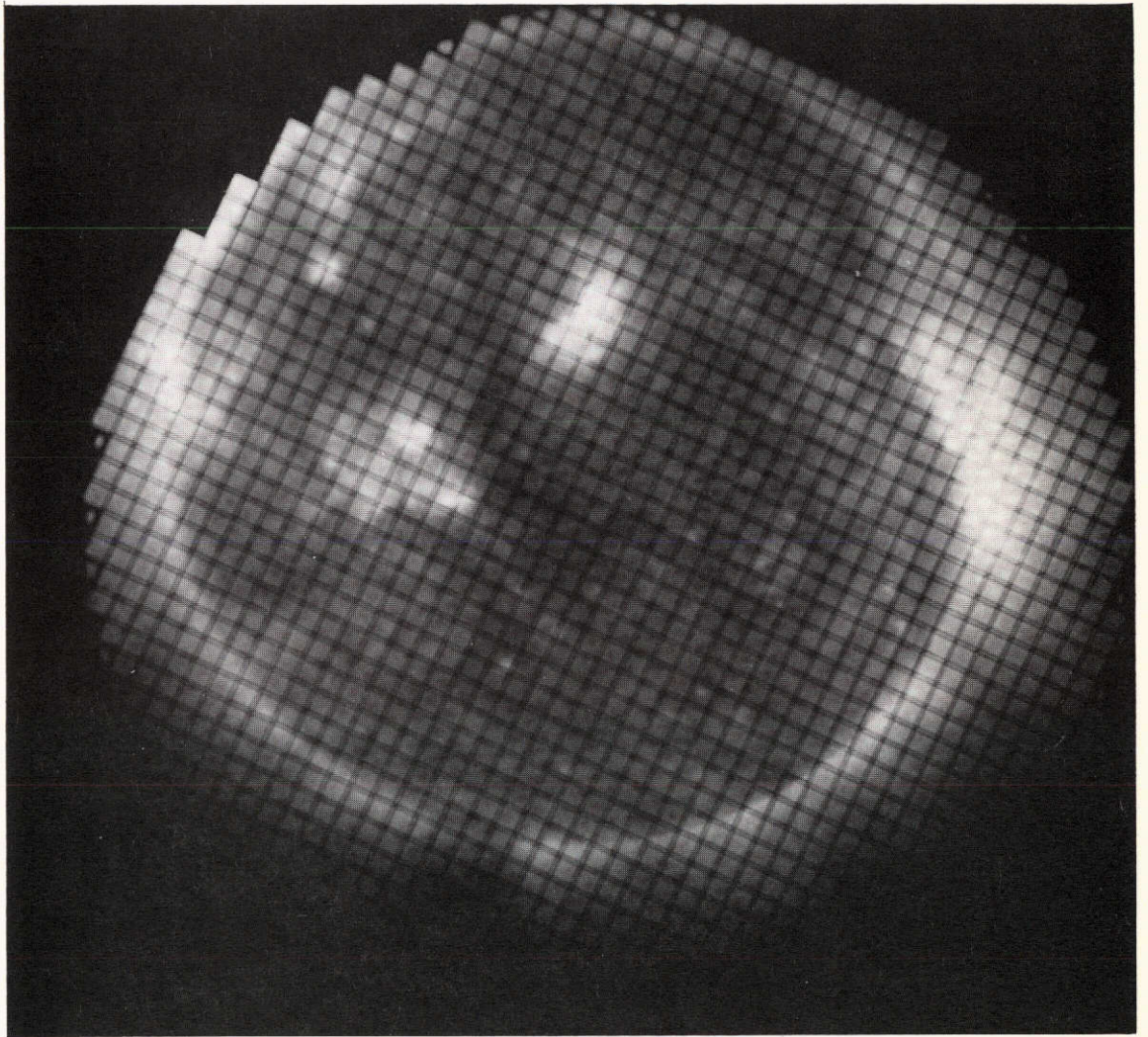
0.2MY+P/UTC PAN-X/EF004

REPRODUCIBILITY OF THE  
ORIGINAL PAGE IS POOR

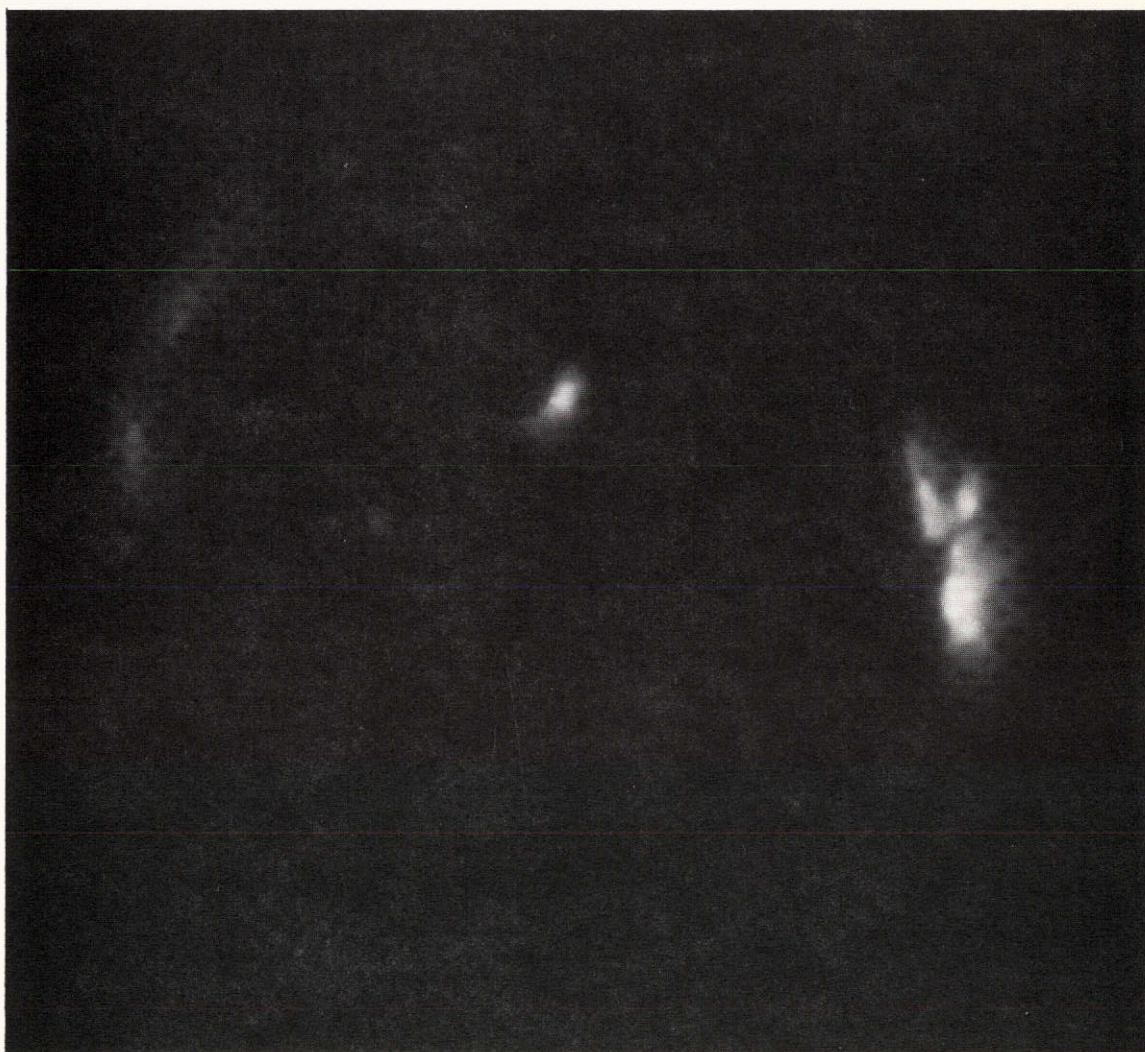


AL-P/MICROFILE/EF005





AL+P/UTC PAN-X/EF008



0.5BE+P/TC PAN-X/EF002





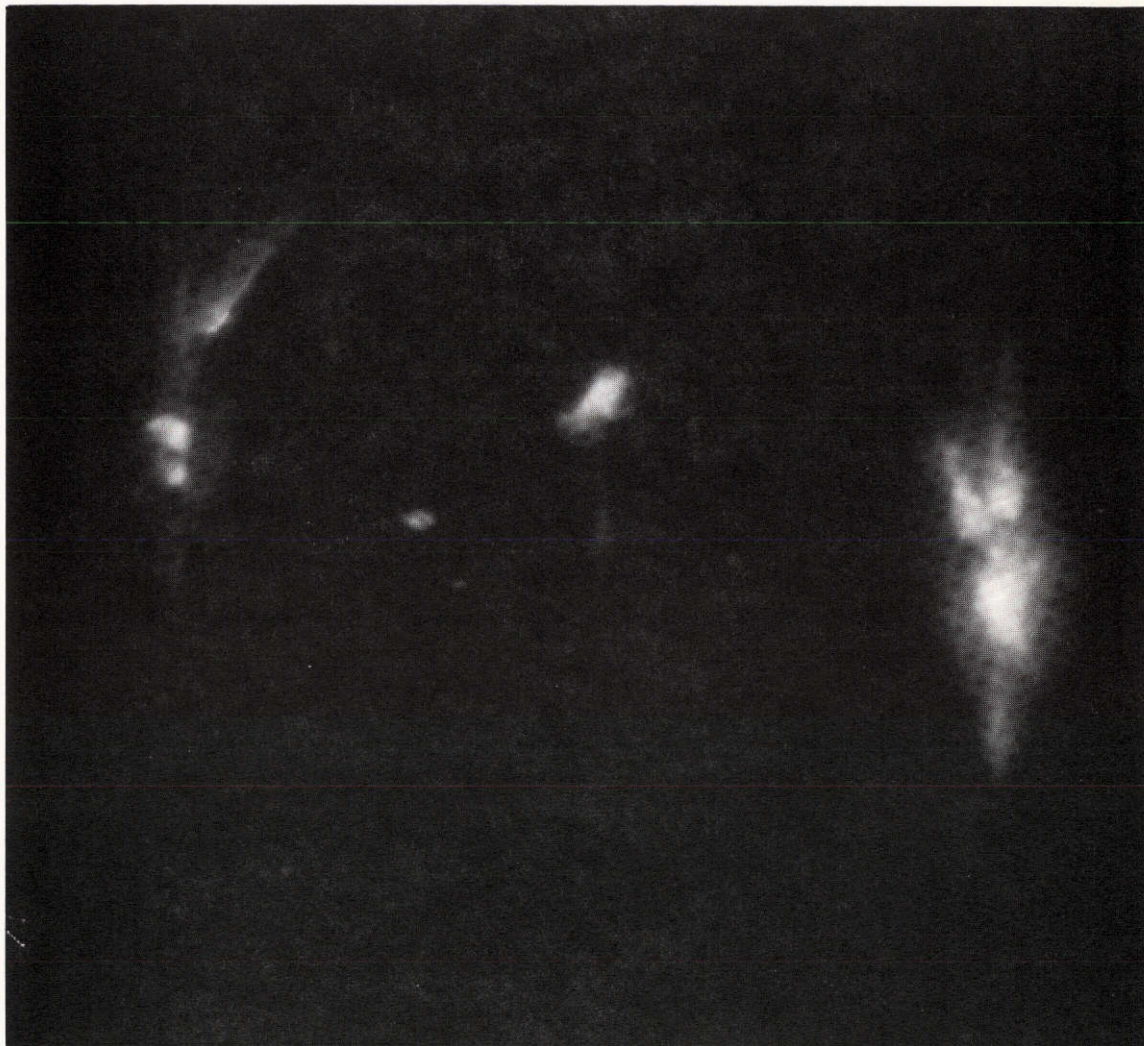
0.5BE+P/TC PAN-X/EF007



0.5BE+P/TC PAN-X/EF010

C-2





0.5BE+G/TC PAN-X/EF012



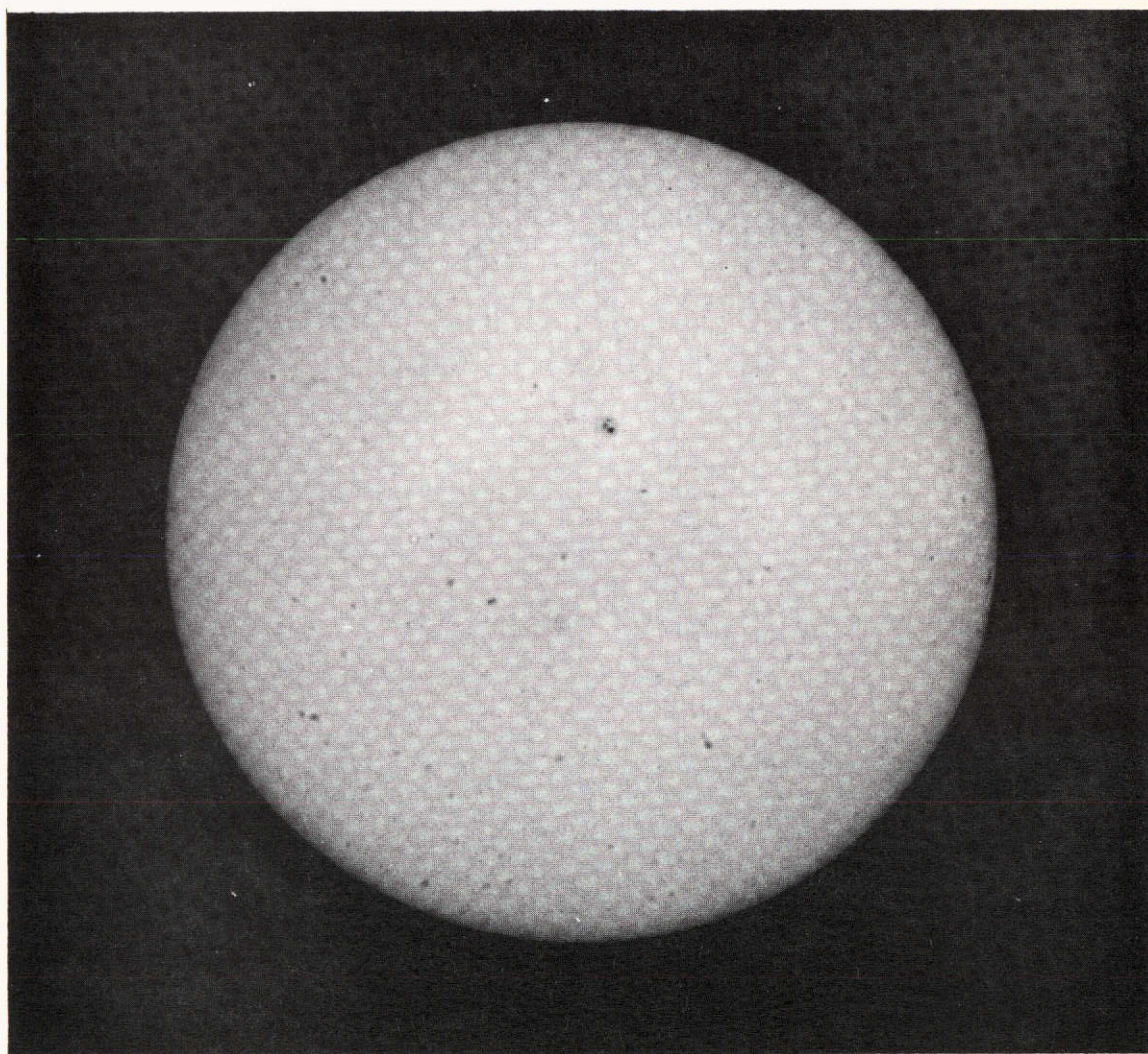


TABLE III

4 November 1969 Aerobee Rocket Flight  
Film and Filters<sup>1</sup>

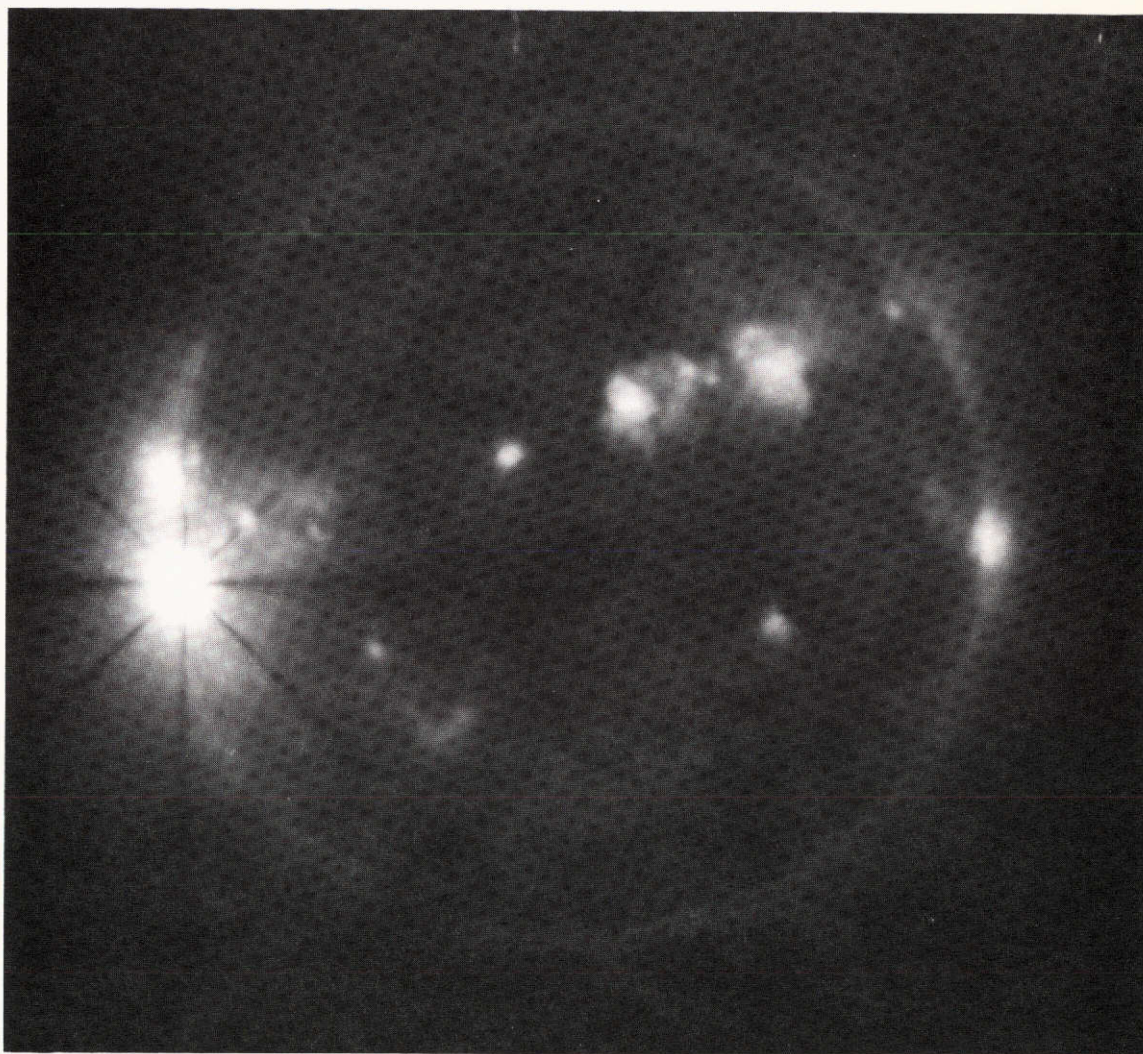
<u>Nominal Exposure Time(sec)</u>	<u>Measured Passband ( 1% Transmission)</u>	<u>Measured Filter Thickness</u>	<u>Film Material</u>
1.8	3-23, 44-60 Å	3.7μ	Parylene-n + Al <sup>2</sup>
0.02	3-23, 44-60 Å	3.7μ	Parylene-n Al
1.8	3-18 Å	10.2μ	Beryllium
0.02	3-18 Å	10.2μ	Beryllium
1.8	3-12 Å	44.2μ	Beryllium
1.8	4000-7000		Neutral Density (White Light)

This flight involved cinematography of a flare. The photographs included here represent a typical sequence of exposures.

1 - Kodak 3400 film was used for all exposures. It is basically Pan-X with a protective ("topcoat") gelatin layer.

2 - The Parylene filter was coated with 0.2μ Aluminum. All values are nominal.





3.5PA+P/3400/

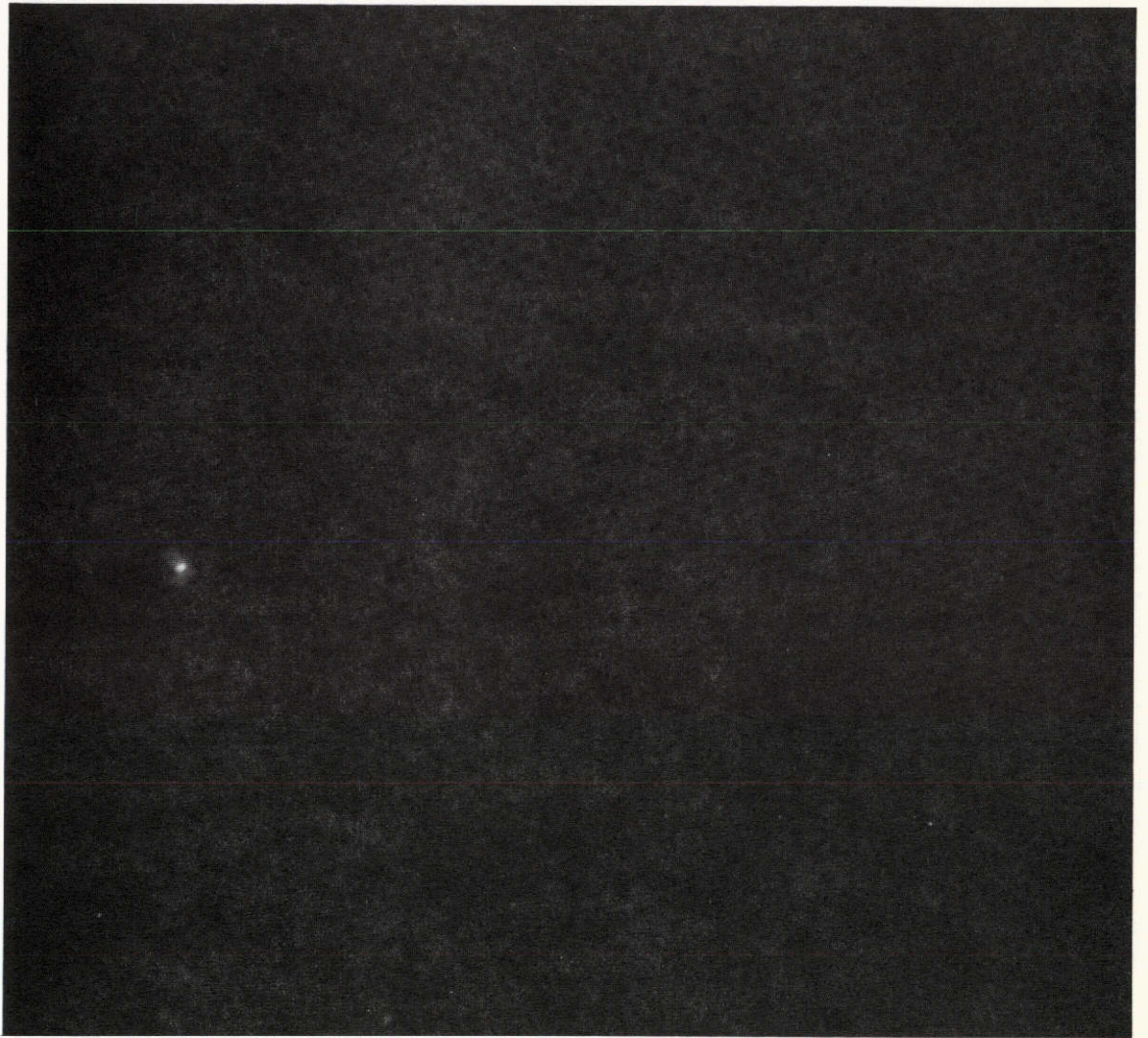


3.5PA+P/3400/





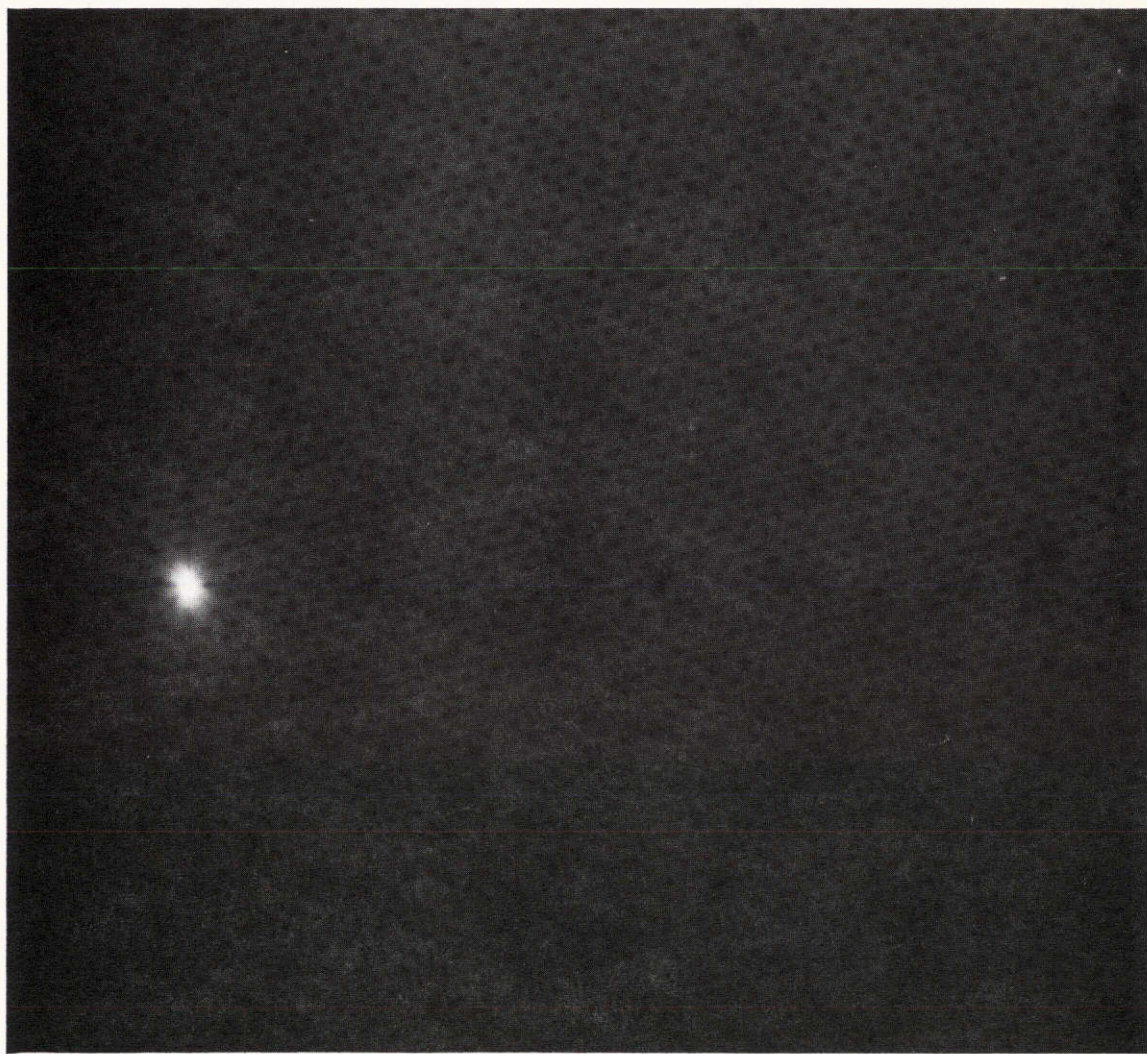
0.5BE+P/3400/



0.5BE+P/3400/

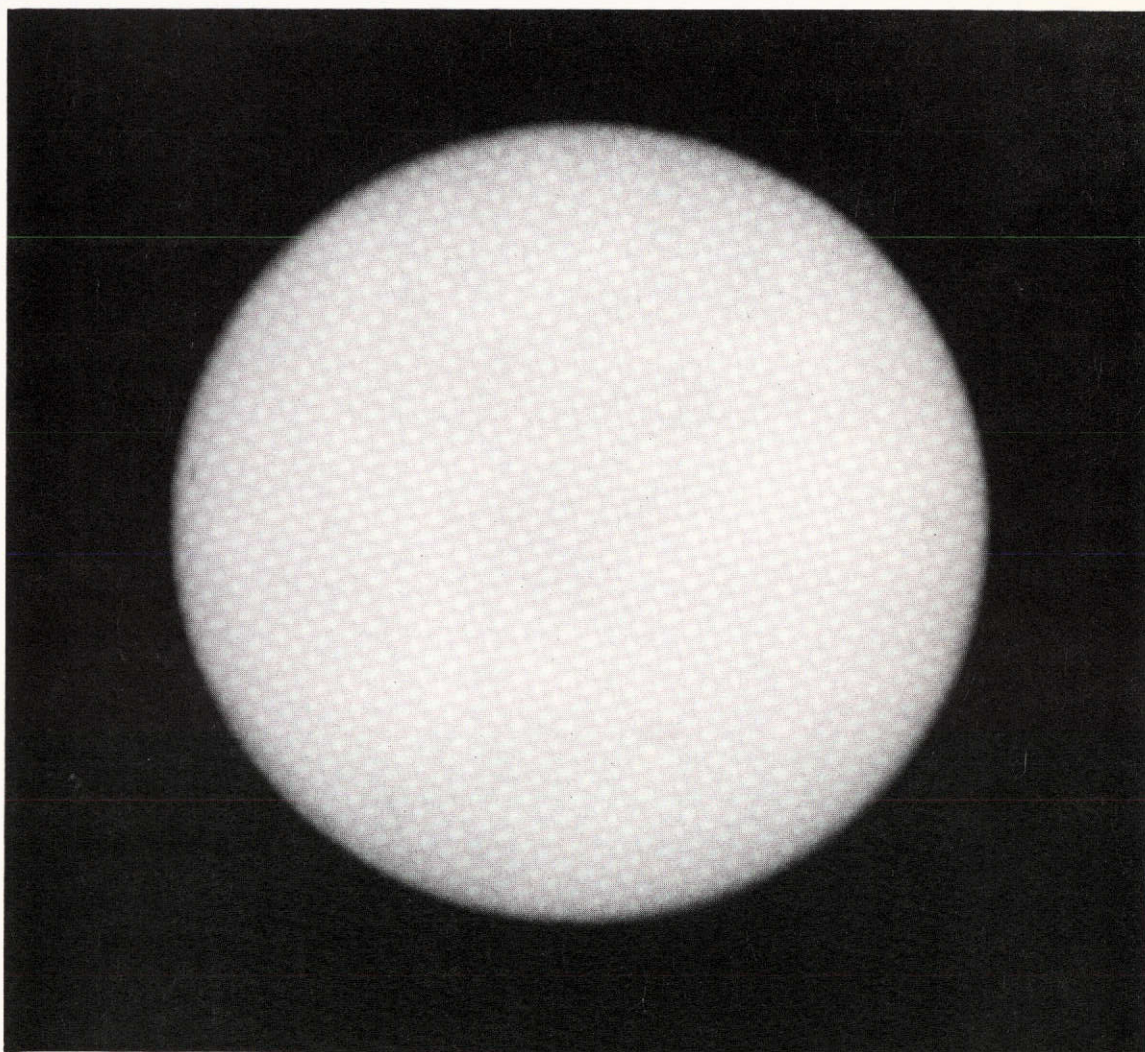
REPRODUCIBILITY OF THE  
ORIGINAL PAGE IS POOR





1.5BE+P/3400/





VL/3400/

TABLE IV

7 March 1970 Aerobee Rocket Flight

Film and Filters<sup>1</sup>

<u>Exposure Time (sec)</u>	<u>Measured Passband (1% Transmission)</u>	<u>Measured Filter Thickness</u>	<u>Filter Material</u> <sup>3</sup>
11.4	3-28, 31-34, 44-49 Å <sup>2</sup>	1.2μ	Parylene-n + Al <sup>4</sup>
1.8	3-35, 44-51 Å	1.2μ	Parylene-n + Al
29.1	3-18, 44-46 Å	4.1μ	Mylar + Al <sup>5</sup>
27.0	3-13, 18-23 Å	4.6μ	Teflon + Parylene-n + Al <sup>6</sup>
6.0	3-13 <sup>2</sup>	4.6μ	Teflon + Parylene-n + Al
1.0	4300 - 4800		Neutral Density (White Light)

1 - Kodak SO-114 film was used for all exposures. It is basically Pan-X with no protective ("topcoat") gelatin layer.

2 - This passband includes the effect of atmospheric absorption near the end of the flight.

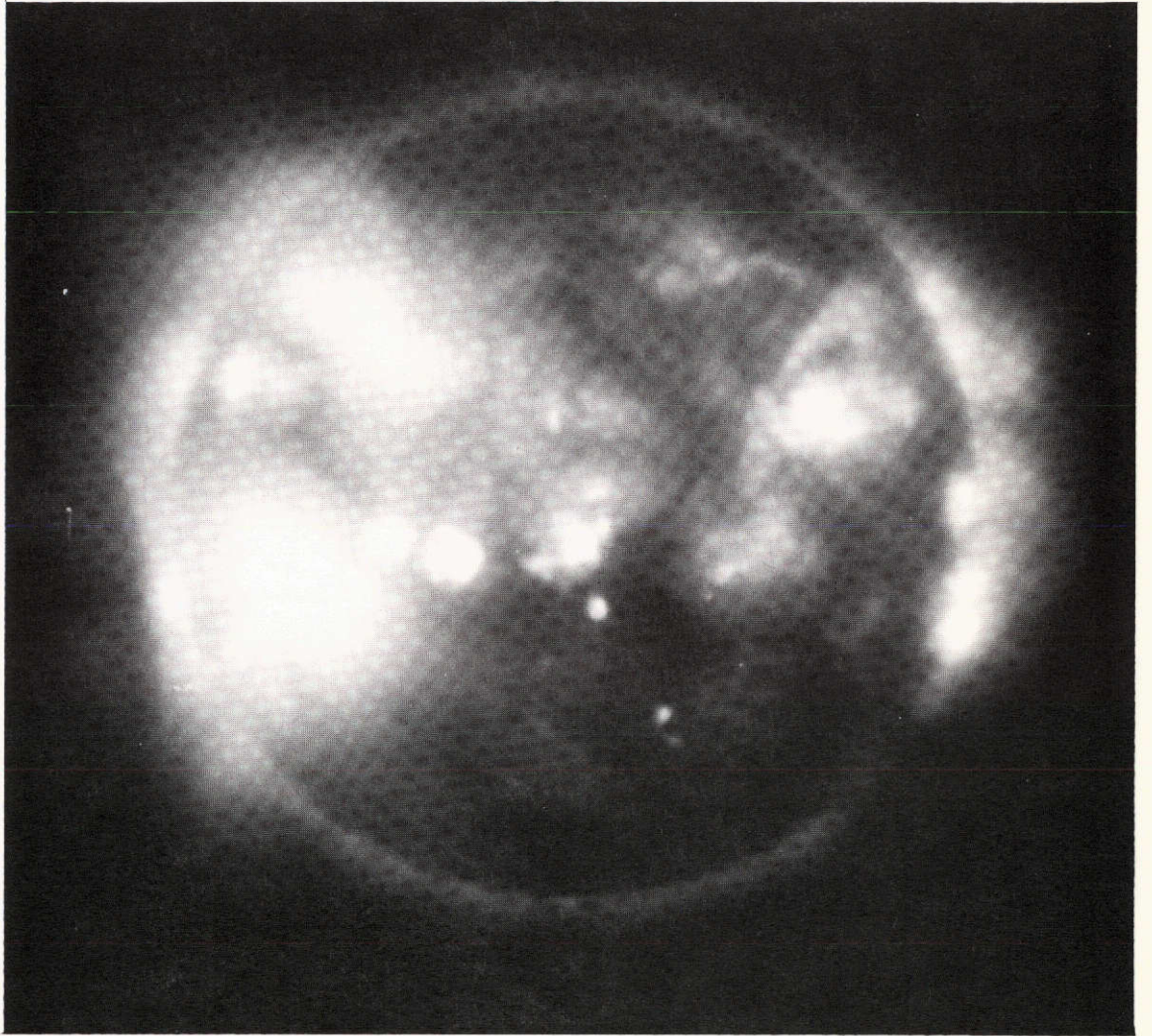
3 - All of the exposures except the White Light include the effect of a fixed heat rejection 0.15μ Al filter in the optical path with a 78% transparent Ni mesh.

4 - The Parylene filter was coated with 0.25μ Al.

5 - The Mylar filter was coated with 0.2μ Al. All values are nominal.

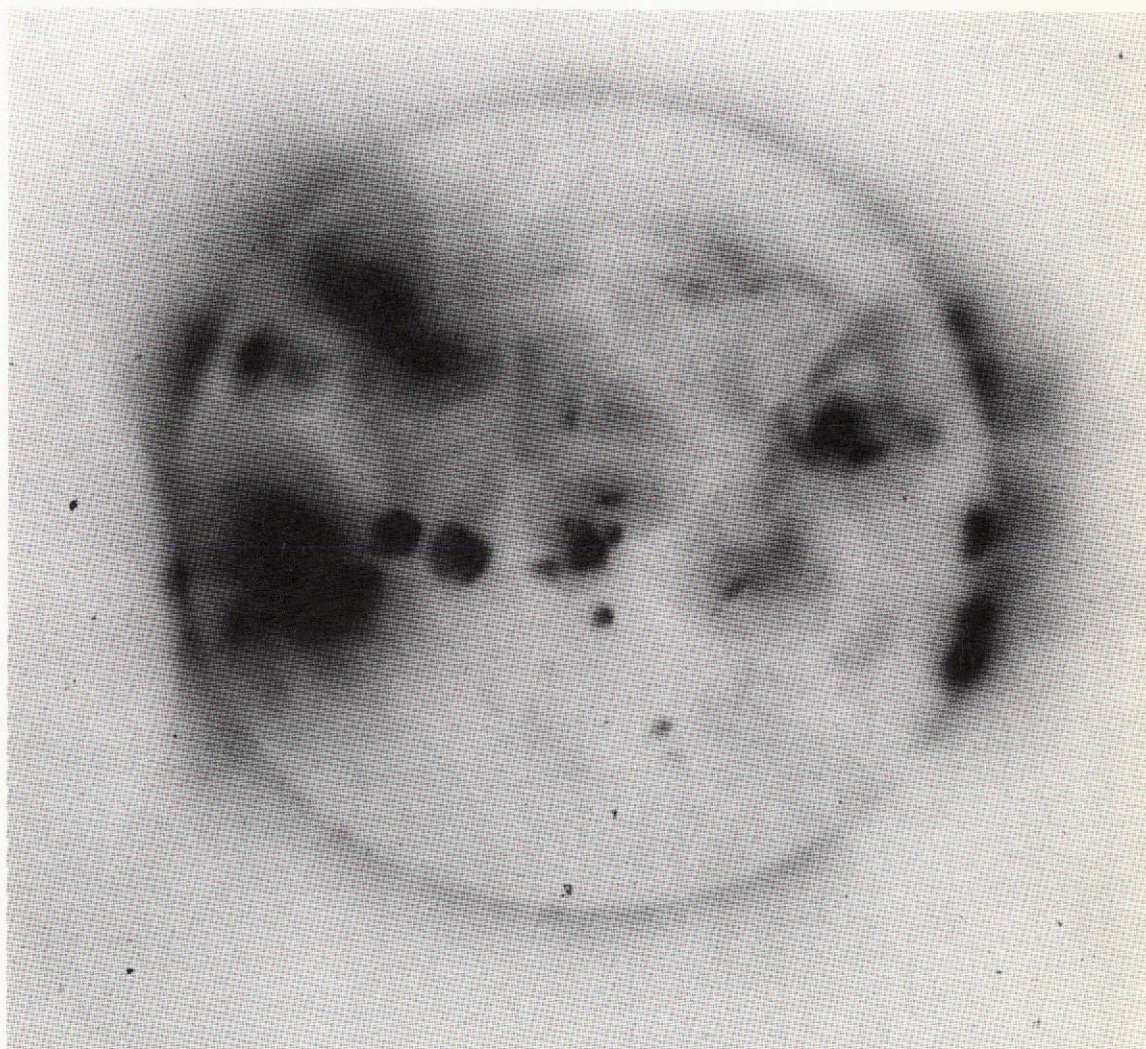
6 - This filter consisted of 3.2μ Teflon, 1.1μ Parylene and 0.2μ Al. All values are nominal





0.8PA+P/S0114/EN012

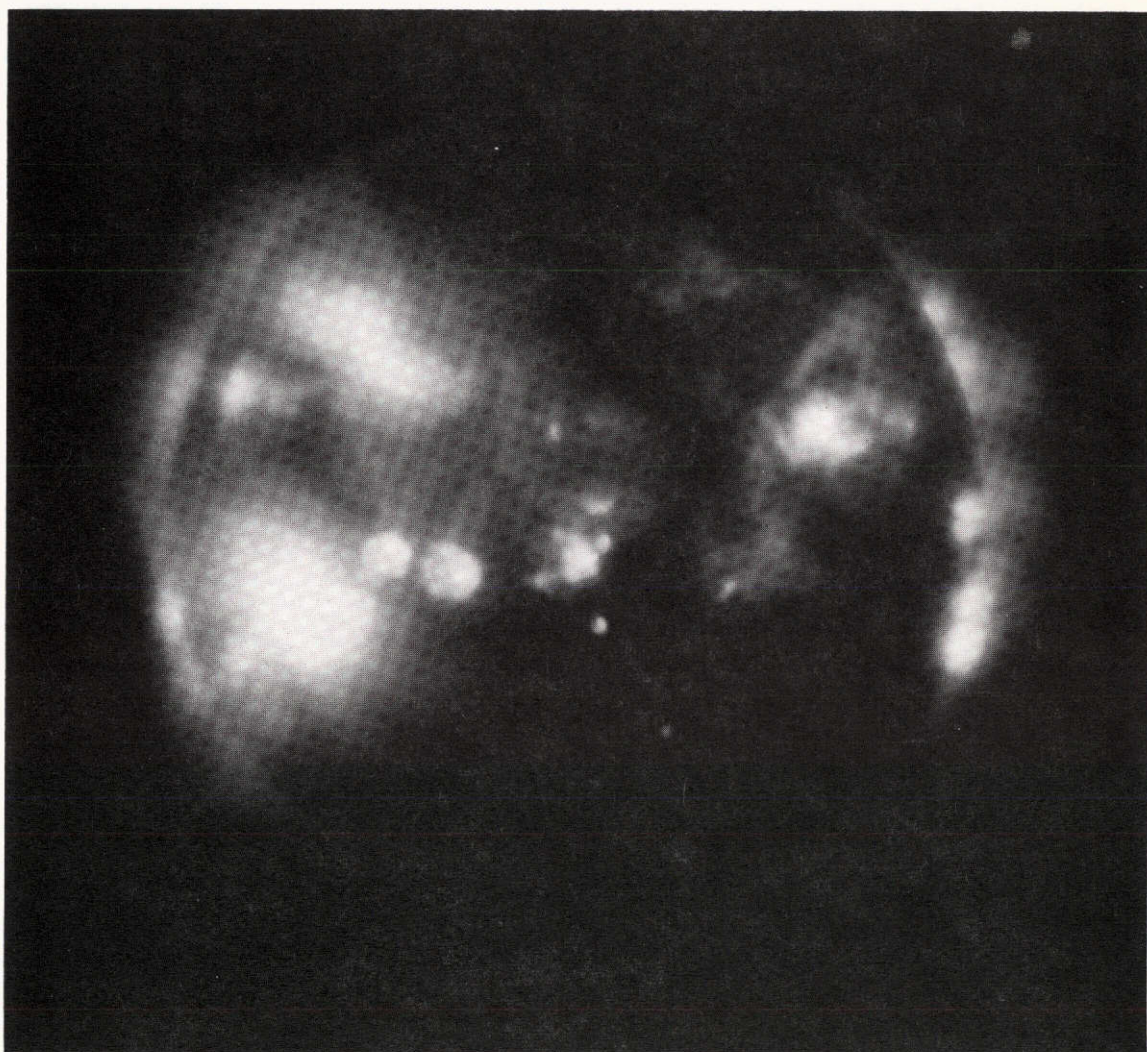




0.8PA+P/SO114/EN015

REPRODUCIBILITY OF THE  
ORIGINAL PAGE IS POOR





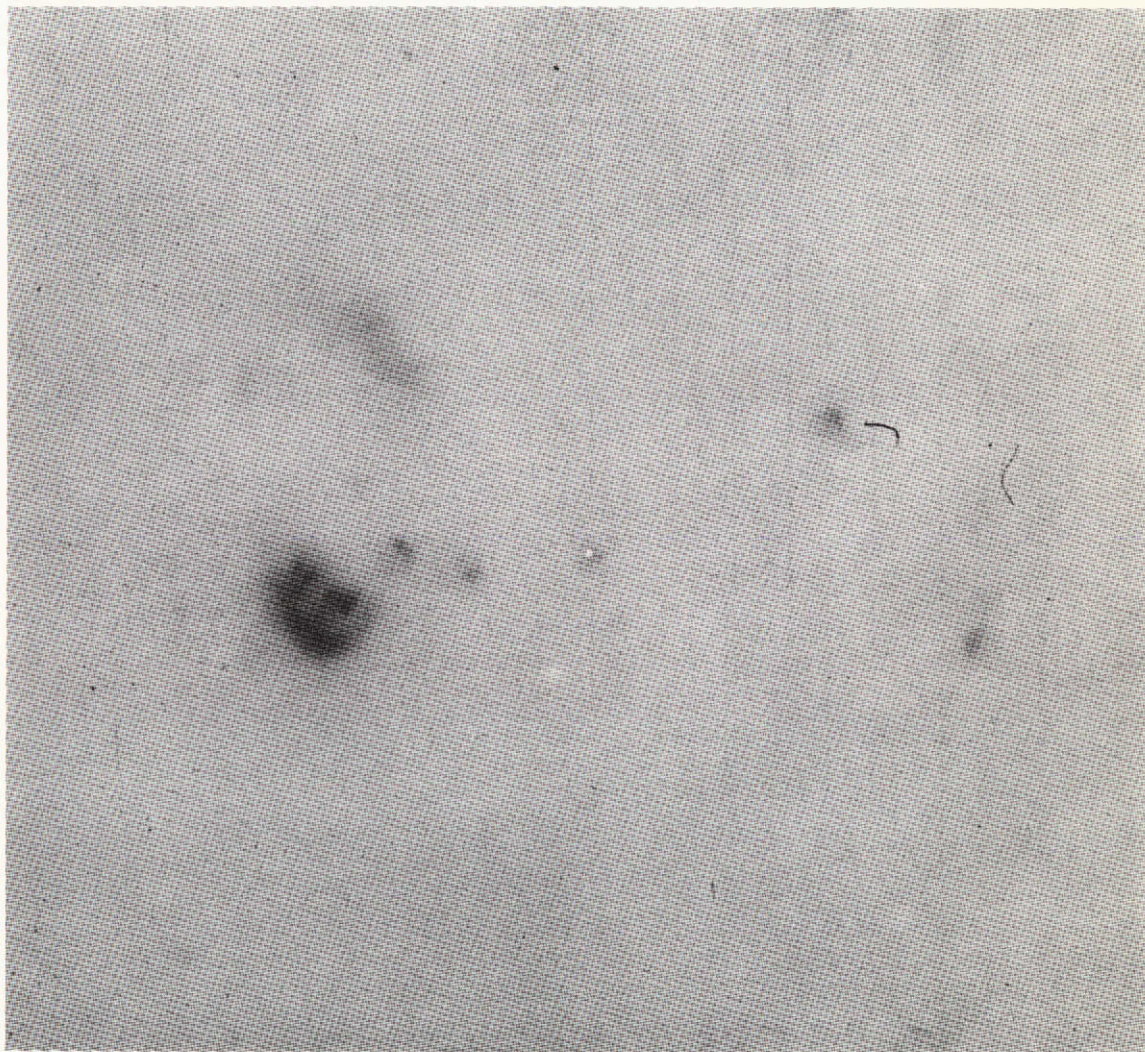
3.8MY+P/S0114/EN010





TEF+P/S0114/EN011

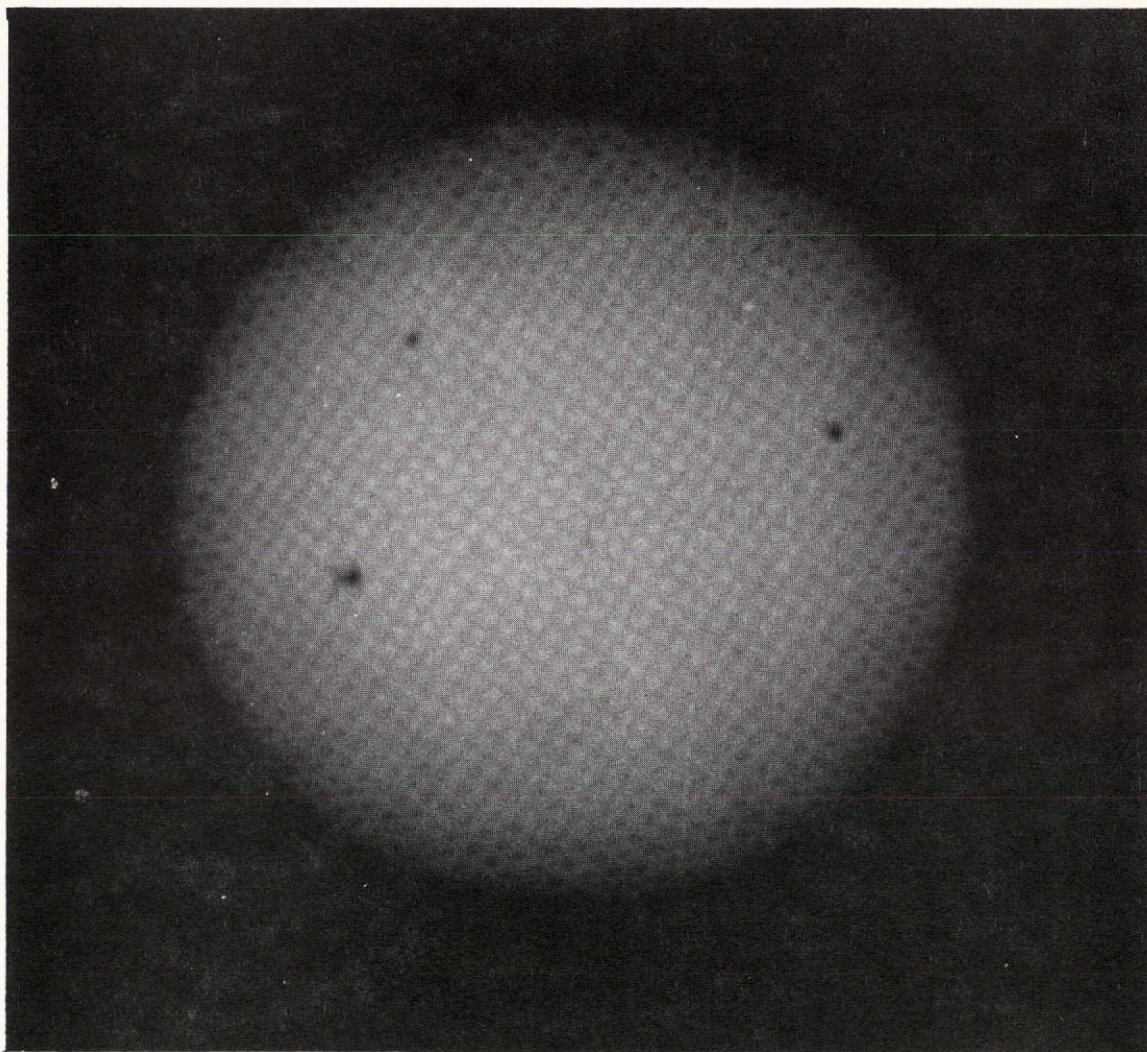




TEF+P/S0114/EN017

REPRODUCIBILITY OF THE  
ORIGINAL PAGE IS POOR





VL/S0114/EN013



TABLE V

24 November 1970 Aerobee Rocket Flight

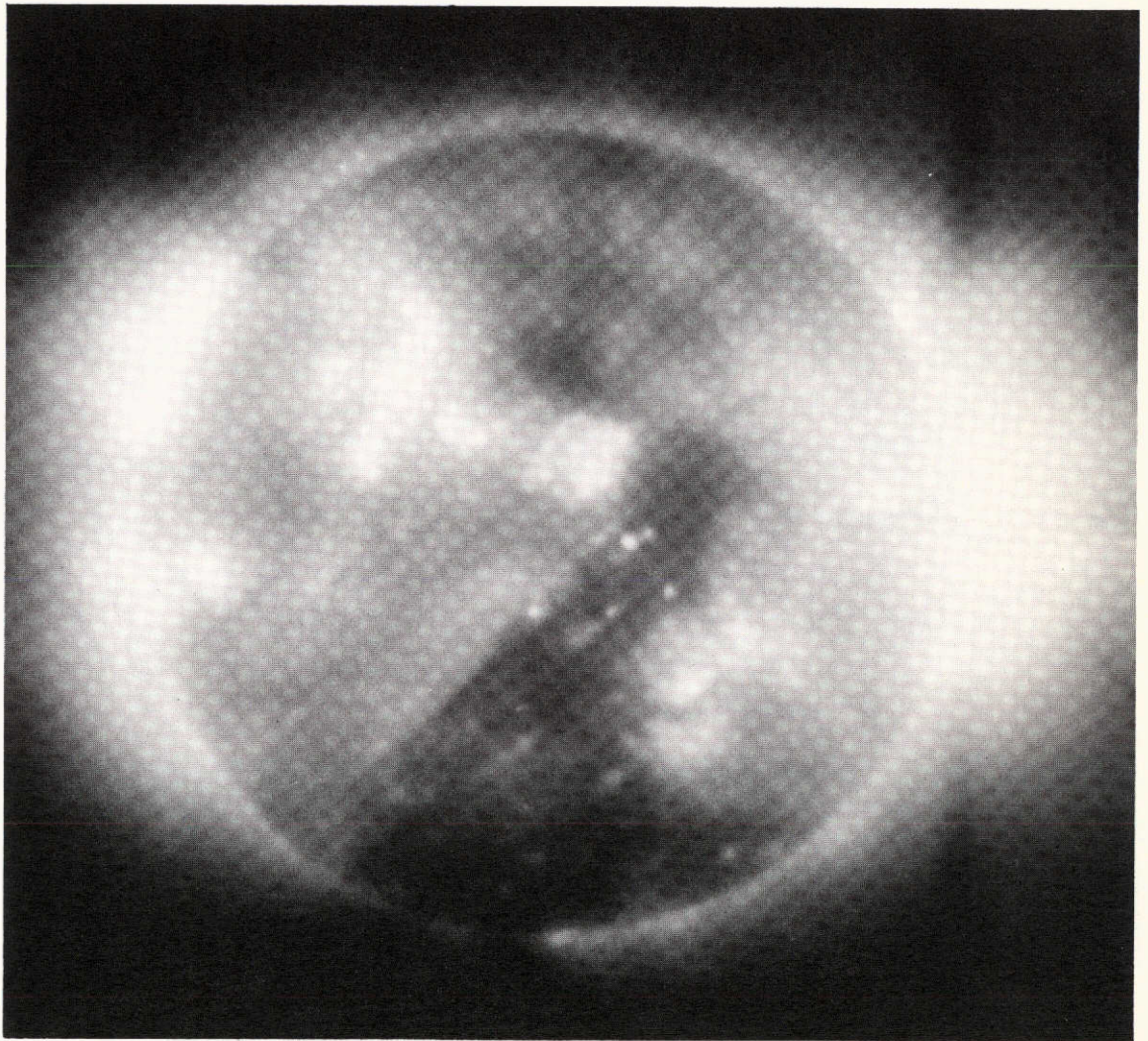
Films and Filters<sup>1</sup>

<u>Exposure Time (sec)</u>	<u>Measured Passband (1% Transmission)</u>	<u>Measured Filter Thickness</u>	<u>Filter Material</u>
40.7	3-35, 44-51 Å	1.2μ	Parylene-n + Al <sup>2</sup>
9.5	3-35, 44-51 Å	1.2μ	Parylene-n + Al
3.0	3-35, 44-51 Å	1.2μ	Parylene-n + Al
0.8	3-35, 44-51 Å	1.2μ	Parylene-n + Al
29.7	3-19 Å	6.2μ	Parylene-n + Al
9.3	3-19 Å	6.2μ	Parylene-n + Al
2.9	3-19 Å	6.2μ	Parylene-n + Al
0.7	3-19 Å	6.2μ	Parylene-n + Al
60.9	3-18 Å	10.2μ	Beryllium <sup>3</sup>
9.4	3-18 Å	10.3μ	Beryllium
1.9	3-18 Å	10.3μ	Beryllium
50.3	3-12 Å	44.2μ	Beryllium <sup>3</sup>
9.2	3-12 Å	44.2μ	Beryllium <sup>3</sup>
1.9	3-12 Å	44.3μ	Beryllium
0.7	4300 - 4800 Å		Neutral Density (White Light)

1 - Kodak SO-114 film was used for all exposures. It is basically Pan-X with no protective "topcoat" gelatin layer.

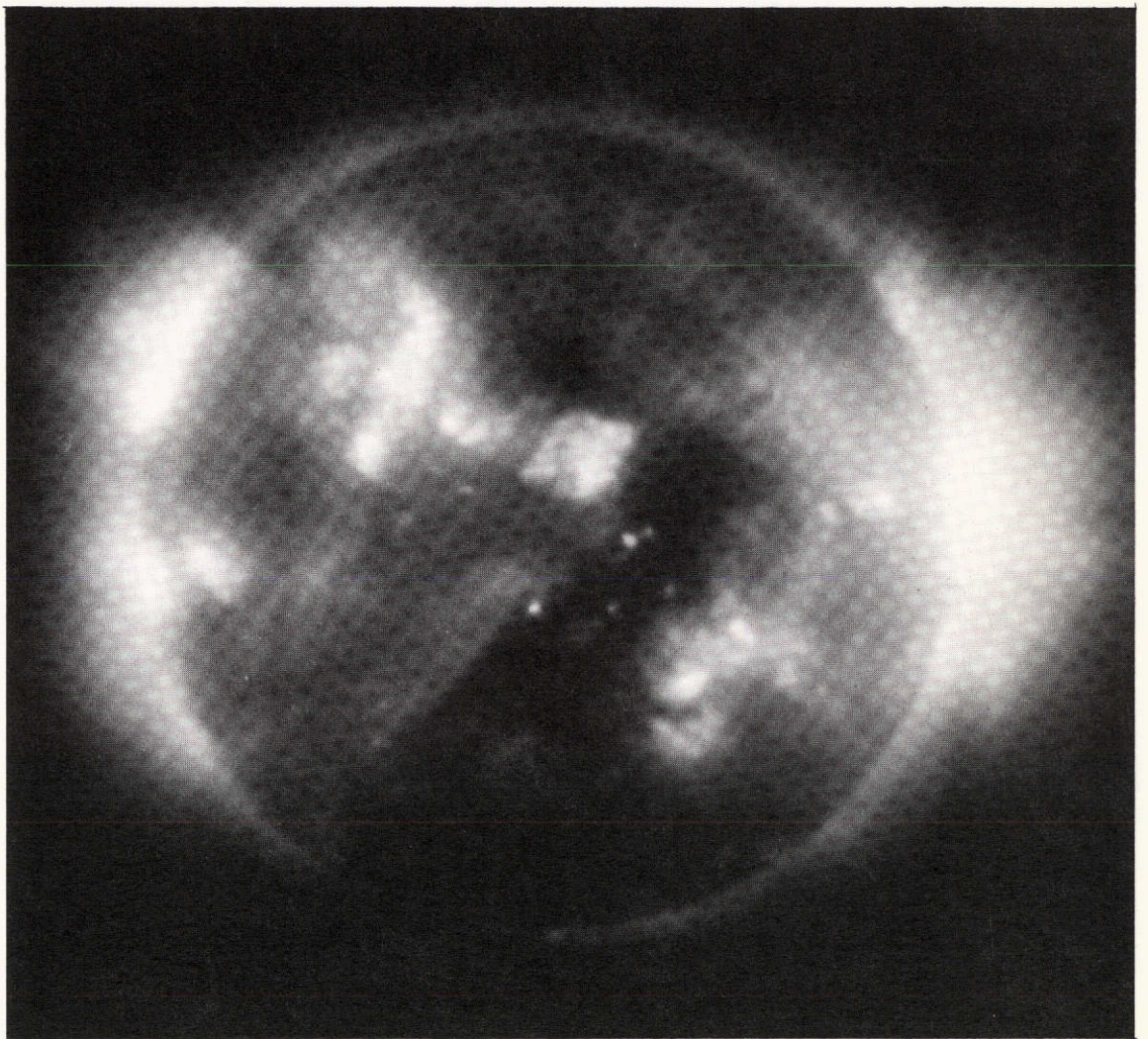
2 - The Parylene filters were coated with Aluminum (the thin filter with 0.25μ and the thicker with 0.32μ). These values also include the effect of a fixed heat rejection 0.15μ Al filter in the optical path with a 78% transparent Ni mesh.

3 - Filter does not have heat rejection filter in optical path.



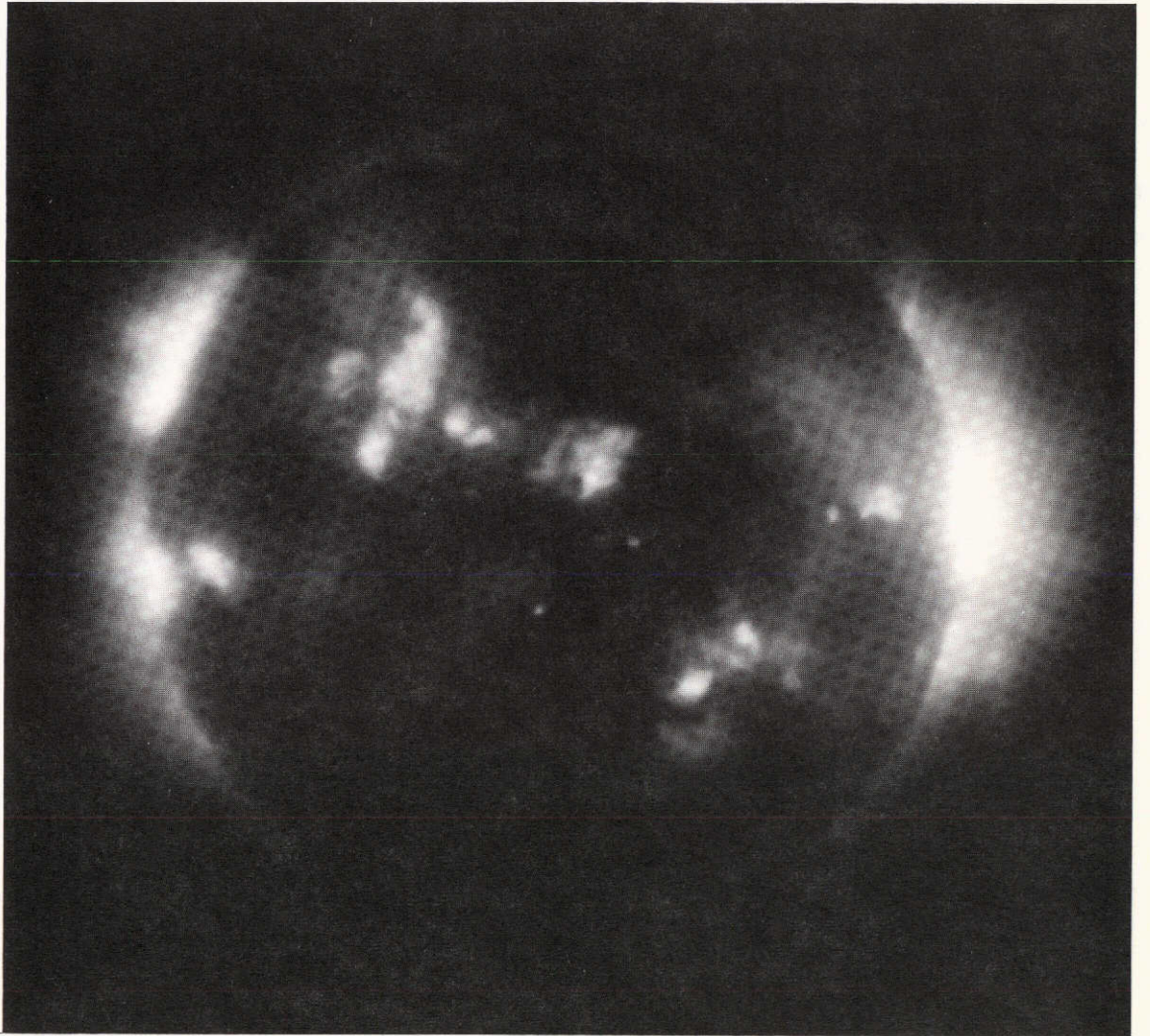
0.8PA+P/S0114/ER018



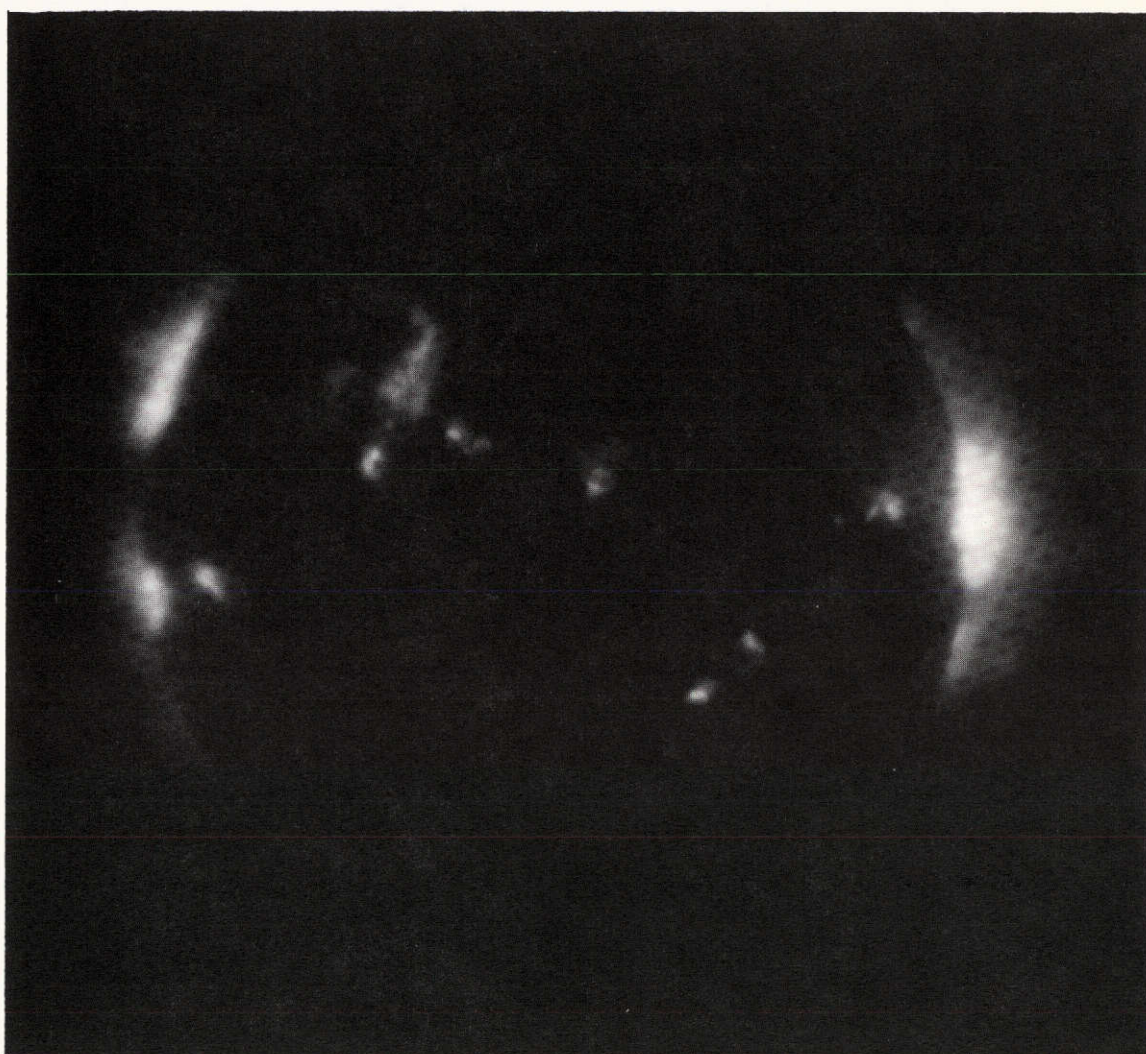


0.8PA+P/SO114/ER011



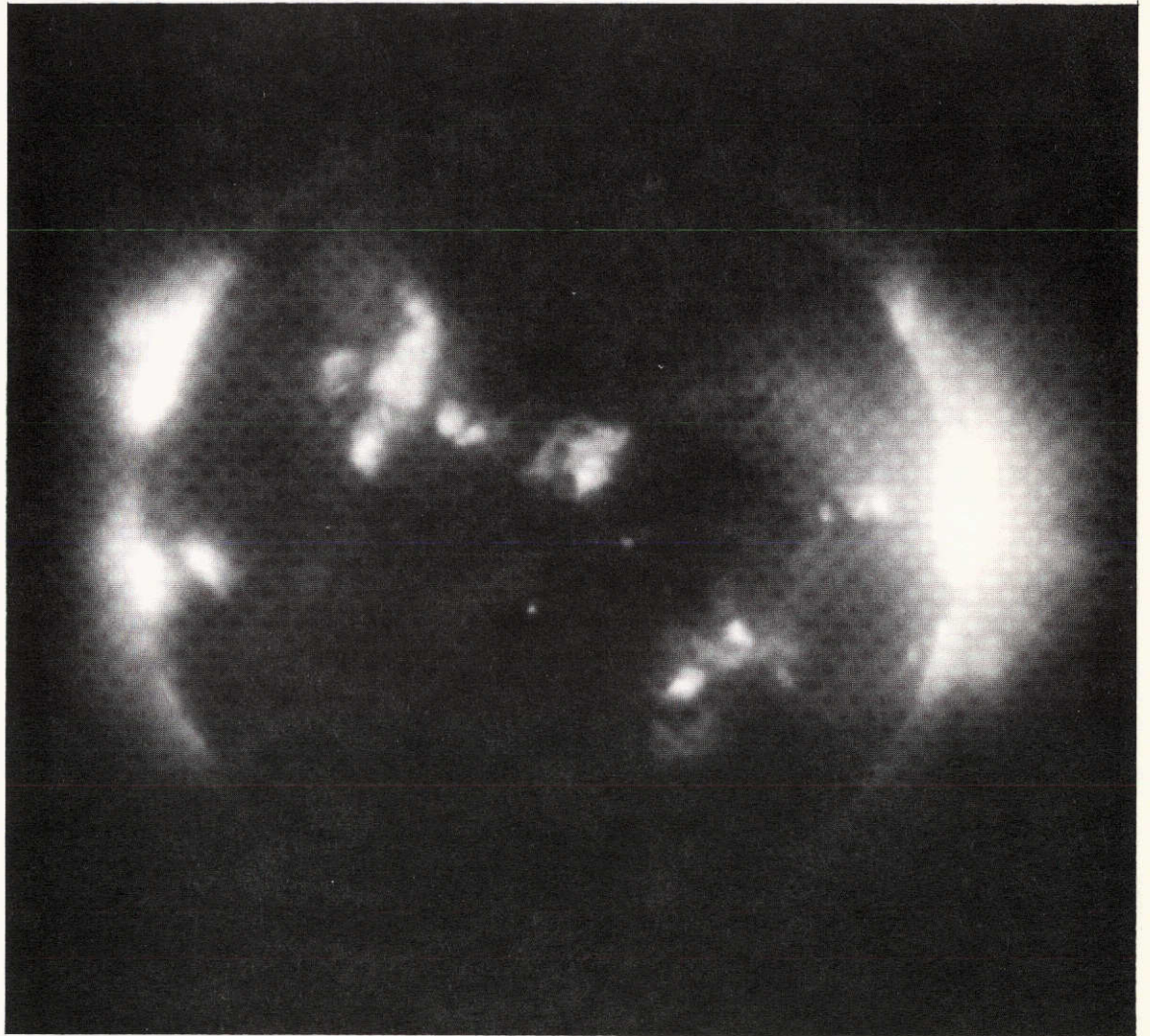


0.8PA+P/SO114/ER013



0.8PA+P/S0114/ER016





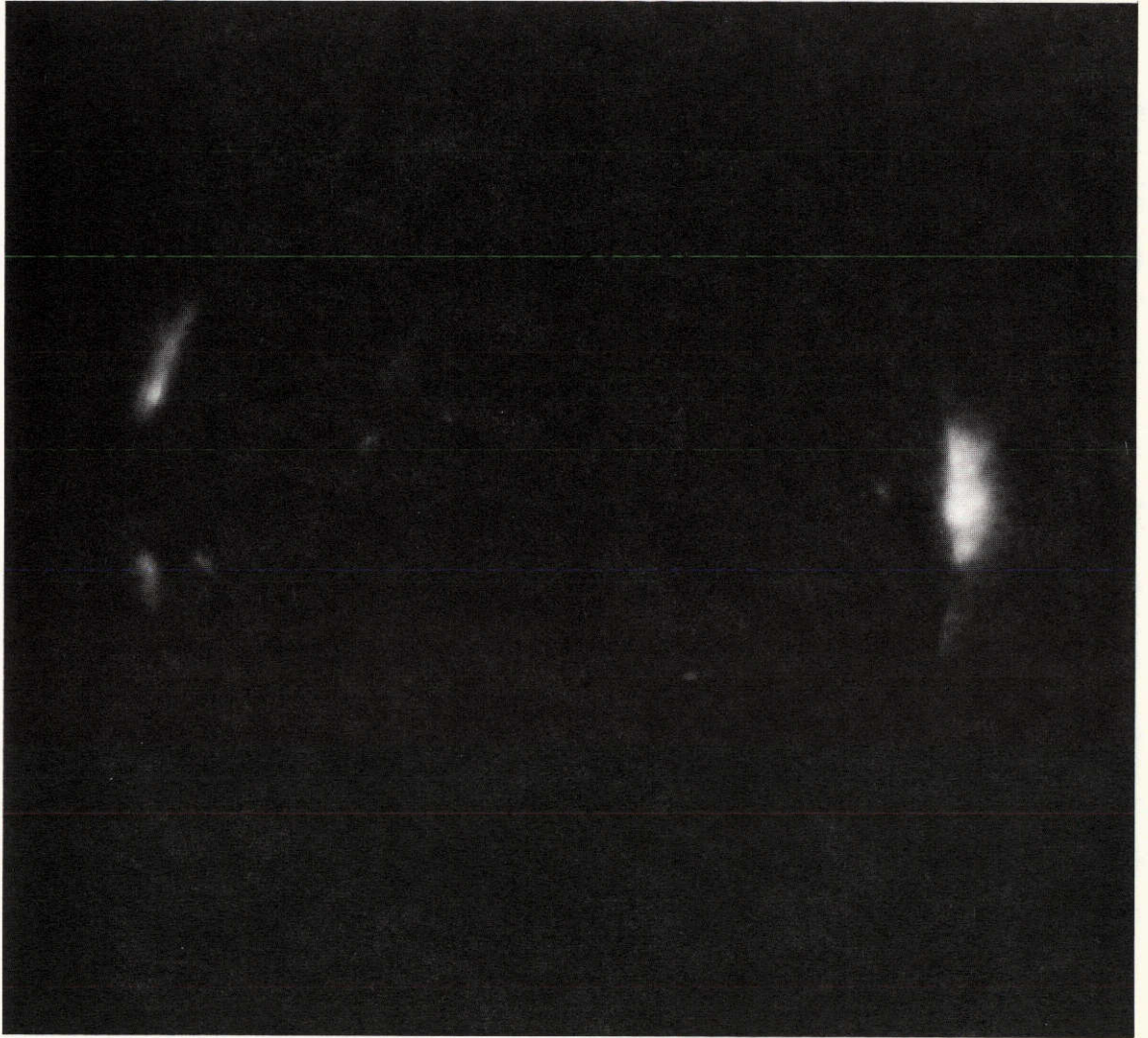
5.7PA+P/SO114/ER010





5.7PA+P/SO114/ER014

REPRODUCIBILITY OF THE  
ORIGINAL PAGE IS POOR



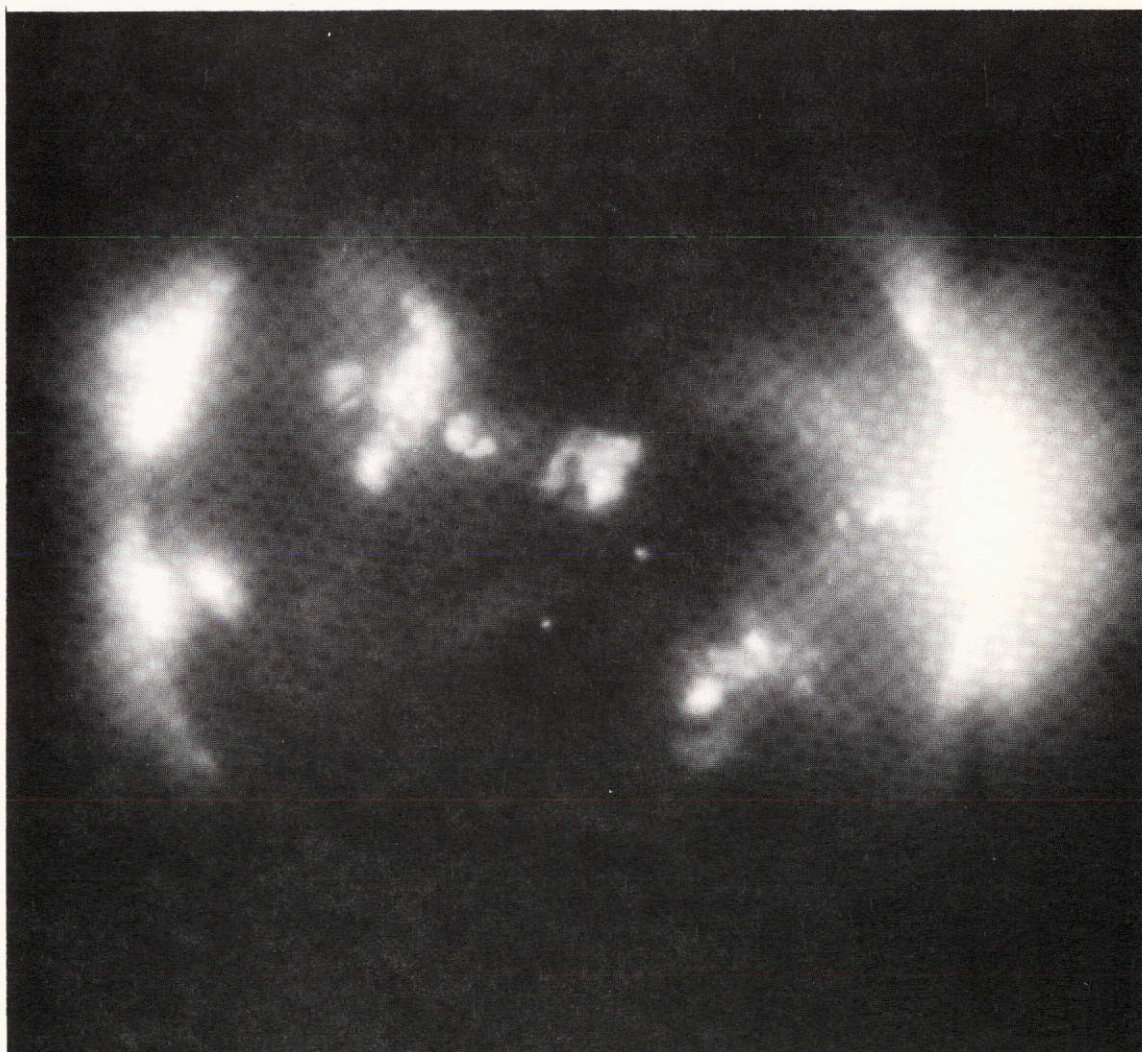
5.7PA+P/S0114/ER017





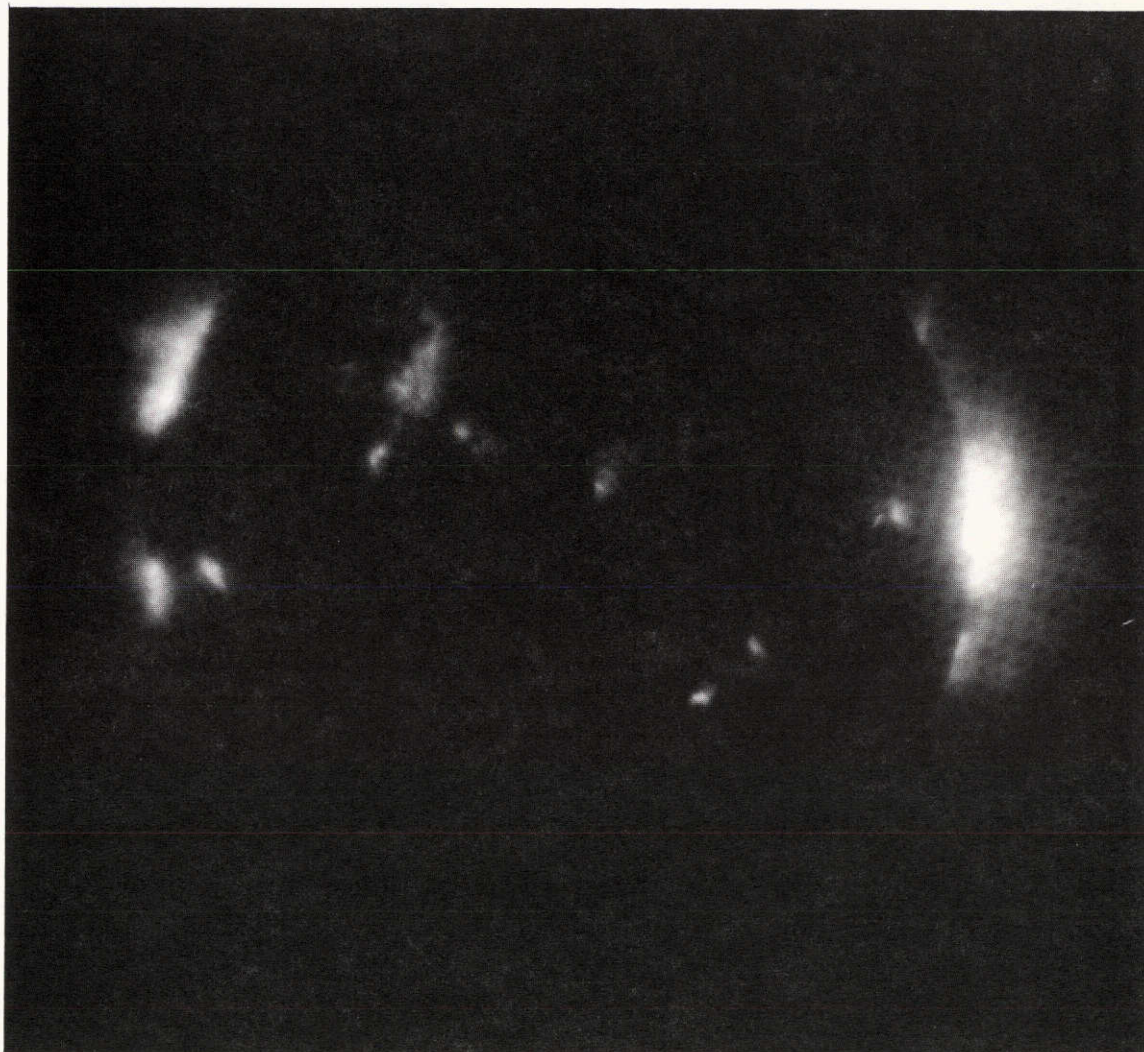
5.7PA+P/S0114/ER019





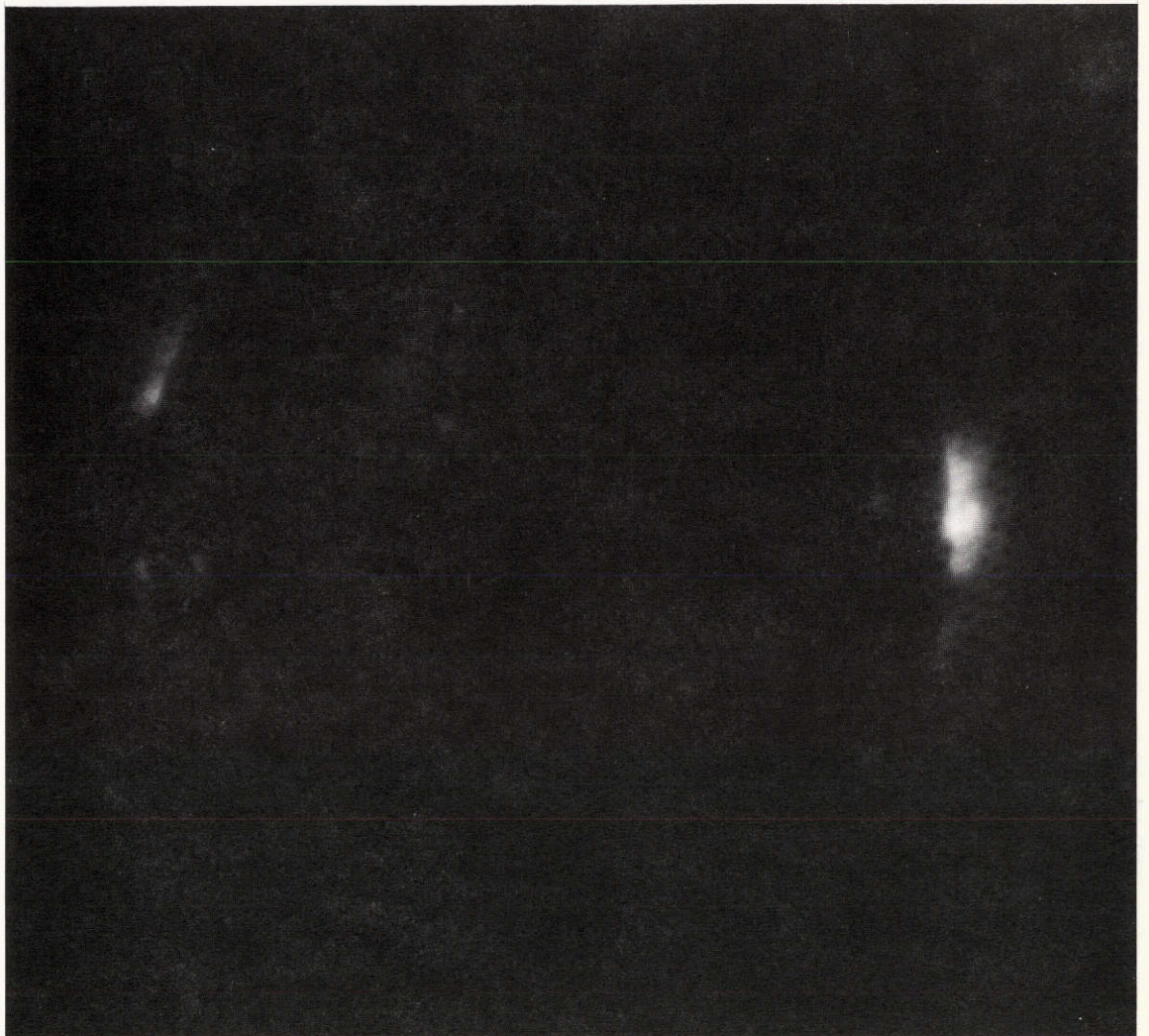
0.5BE/S0114/ER020

REPRODUCIBILITY OF THE  
ORIGINAL PAGE IS POOR



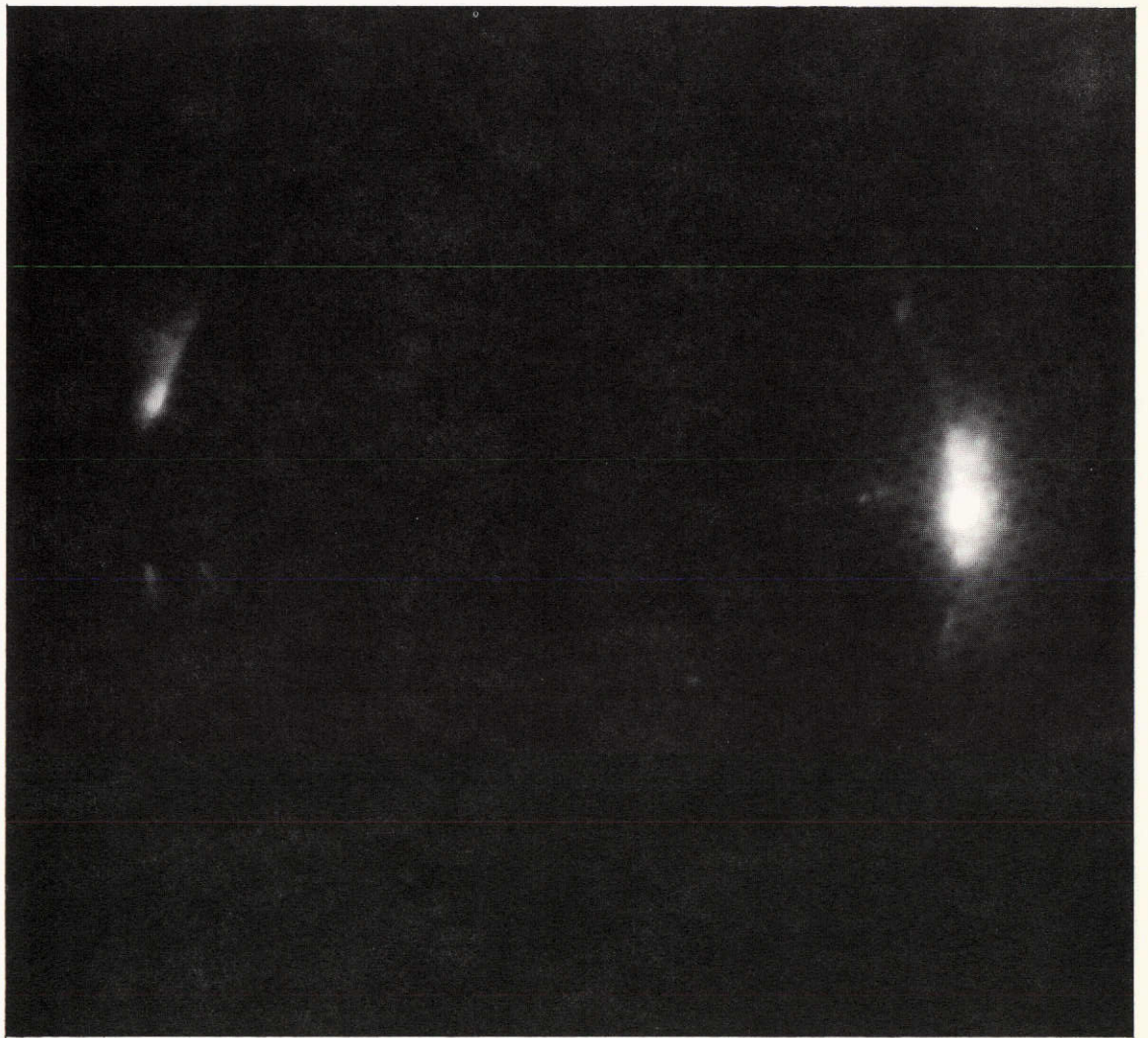
0.5BE+P/S0114/ER009





0.5BE+P/S0114/ER012



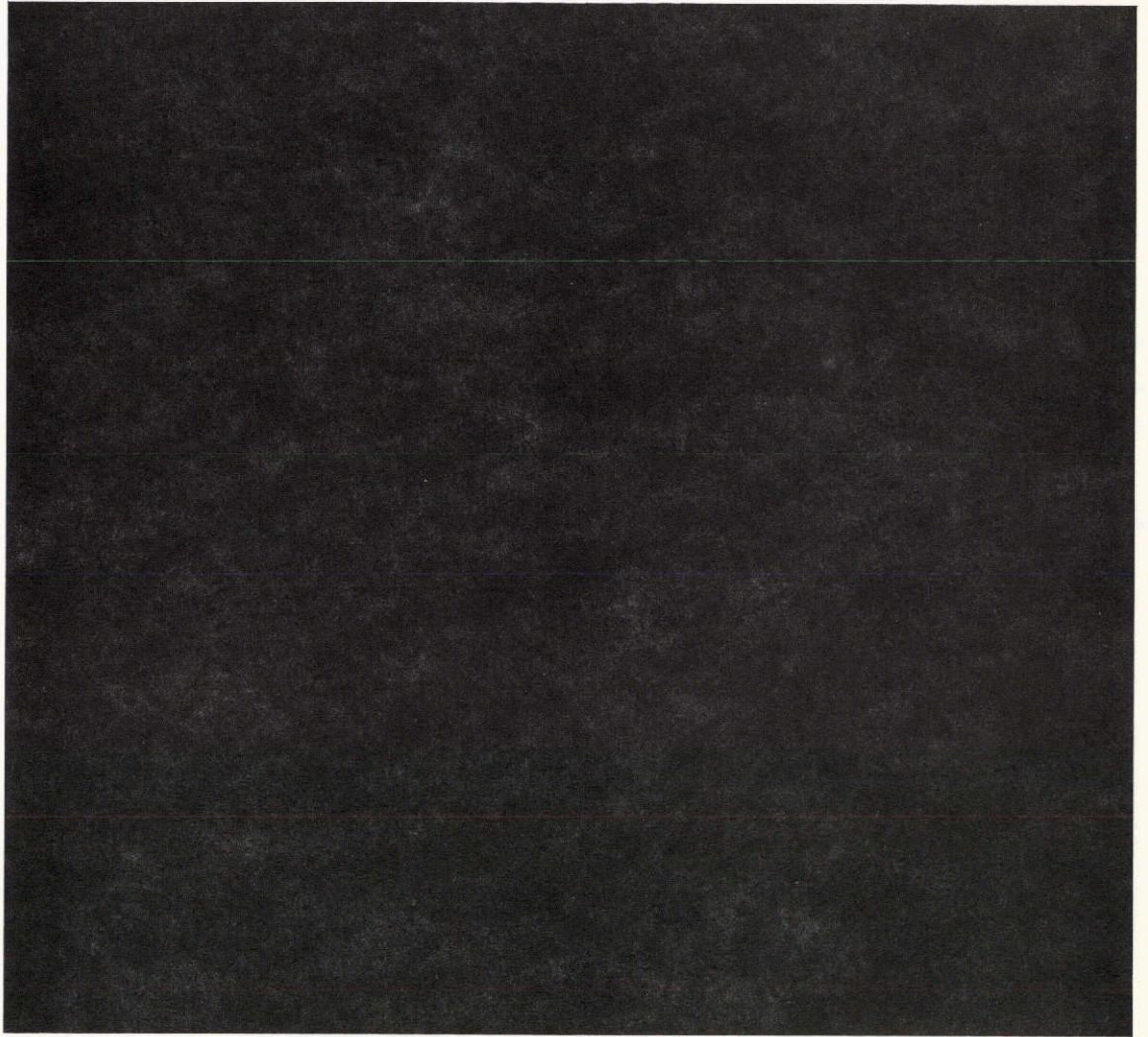


1.5BE/S0114/ER022



1.5BE/S0114/ER007

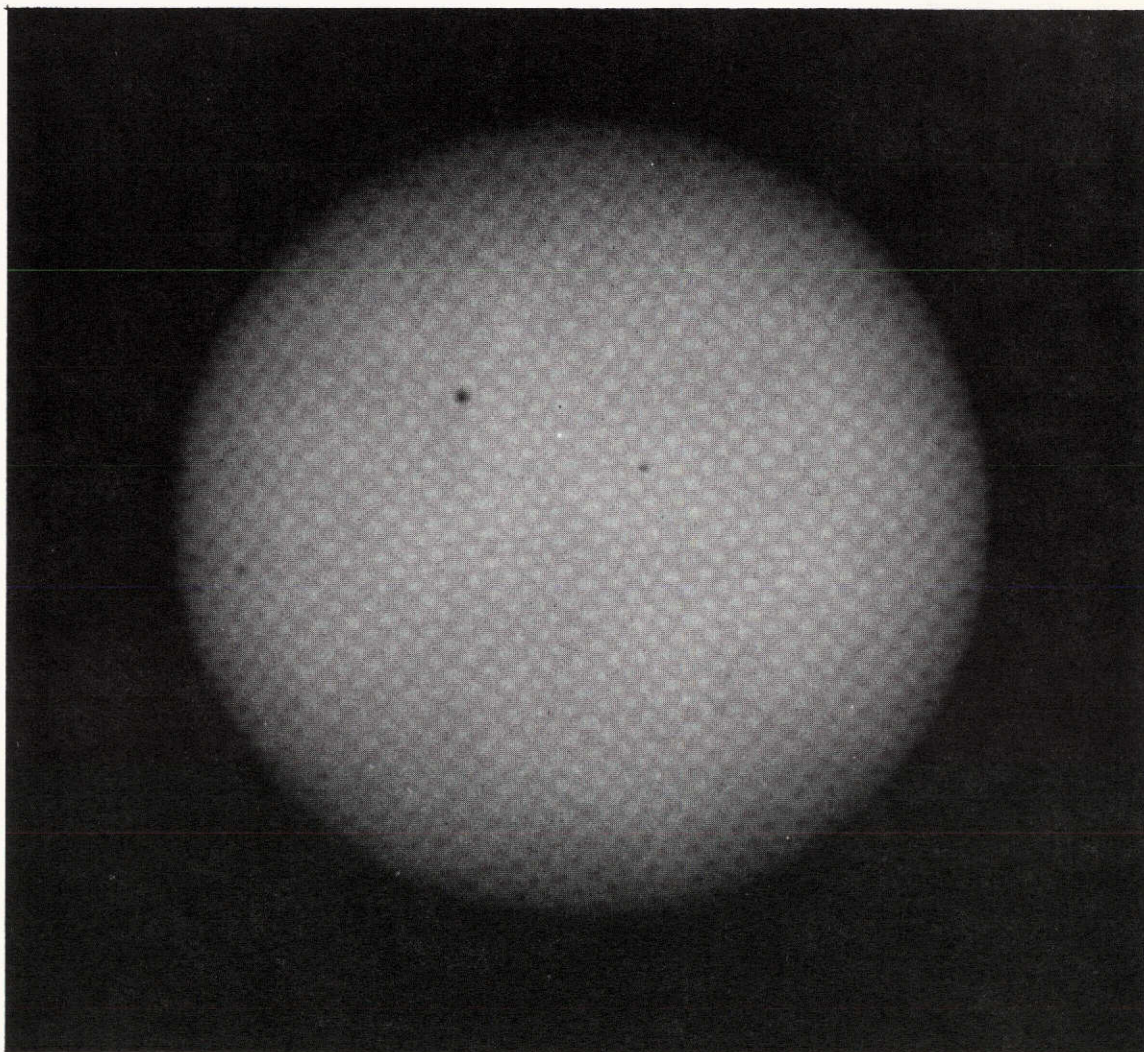




1.5BE+P/SO114/ER015

REPRODUCIBILITY OF THE  
ORIGINAL PAGE IS POOR





VL/S0114/ER008

## APPENDIX C

ASE-3029-A

A CORONAL HOLE AND ITS IDENTIFICATION AS THE  
SOURCE OF A HIGH VELOCITY SOLAR WIND STREAM

A. S. Krieger and A. F. Timothy

American Science and Engineering, Cambridge, Massachusetts

and

E. C. Roelof

University of New Hampshire, Durham, New Hampshire

Submitted for publication to the Editor of SOLAR PHYSICS

August 1972

Revised: December 1972



ABSTRACT. X-ray images of the solar corona, taken on November 24, 1970, showed a magnetically open structure in the low corona which extended from N20W20 to the South Pole. Analysis of the measured X-ray intensities shows the density scale height within the structure to be typically a factor of two less than that in the surrounding large scale magnetically closed regions. The structure is identified as a coronal hole.

Since there have been several predictions that such a region should be the source of a high velocity stream in the solar wind, wind measurements for the appropriate period were traced back to the sun by the method of instantaneous ideal spirals. A striking agreement was found between the Carrington longitude of the solar source of a recurrent high velocity solar wind stream and the position of the hole.

Solar wind bulk velocity and photospheric magnetic field data from the period 1962-1970 indicate the possible extension of the result to the interpretation of long term variations in the wind pattern.

## 1. Introduction

Periodicities of approximately 27 to 28 days duration observed in the solar wind bulk velocity (Snyder and Neugebauer, 1966) and in the interplanetary magnetic sector structure (Wilcox, 1968) suggest that there should be a link between these features and conditions in the low corona. There has, however, been a lack of success in finding consistent experimental evidence of that link (Snyder and Neugebauer, 1966; Couturier and Leblanc, 1970; Pathak, 1971). The major difficulty in such studies lies in the fact that neither the sources of the wind streams nor the location of the critical point are known. If the former could be predicted theoretically and the results merely verified by observation of a large number of events, then the correct extrapolation of wind streams back to the sun would present no problem. Alternatively, if the velocity profile of the wind as a function of radial distance from the solar surface were accurately predictable, the extrapolation of individual streams back to the sun could be carried out with confidence and their sources located.

There are a number of workers (Billings and Roberts, 1964; Davis, 1965; Pneuman and Kopp, 1971; Gosling et al., 1972; and Pneuman, 1972) who have suggested that high velocity streams in the solar wind might originate from magnetically open regions in the corona rather than from regions of elevated coronal temperatures. Furthermore, there are now recognized to be a new class of feature in the solar corona, called coronal holes, which have many characteristics which are the antithesis of active regions (Munro and Withbroe, 1972; Altschuler and Perry, 1972; Altschuler, Trotter and Orrall, 1972). When seen in soft X-ray wavelengths they appear as a marked reduction in coronal emission surrounded by coronal structure which has the appearance of a diverging magnetic field configuration.

Since these features apparently have the properties required for the production of high velocity solar wind streams, one example of a coronal hole, seen in soft X-ray solar images, has been compared with a stream source location inferred from solar wind observations for the period. In the absence of the additional X-ray observations of such features, required for a statistical proof of the hole-stream relationship, evidence supporting the extrapolation technique used is cited from theoretical studies of non-linear solar wind equations as well as from recent applications of the mapping to the analysis of low energy solar particle events.

## 2. The Structure of a Coronal Hole a) Inferred Magnetic Field Geometry

The development of high resolution X-ray imaging techniques (Vaiana, 1970; Krieger et al., 1970) has enabled the density and temperature structure of the lowest levels of the solar corona ( $r \leq 1.2 R_{\odot}$ ) to be studied extensively. The X-ray image of the solar corona taken on March 7, 1970 was compared (VanSpeybroeck et al., 1970) with a nearly simultaneous radial density gradient white light exposure (Newkirk and Lacey, 1970). Detailed examination showed that the typical tubular loop structures on the X-ray image extended out far into the low corona, particularly in the vicinity of active regions and filaments. In some cases (the closed 'helmet' streamers) the loops reach heights of between  $1.0$  and  $1.5 R_{\odot}$  before being distorted into a radially streaming configuration by the expansion of the gas.

A typical soft X-ray image of the solar corona, taken during a sounding rocket flight on November 24, 1970, is shown in Fig 1. Active regions are seen as brightly emitting, highly structured areas and are somewhat over-exposed in this picture.



Also apparent are the much larger scale, diffusely emitting structures linking both widely separated active regions and areas of moderately intense unipolar magnetic fields. High loop structures ( $h \sim 0.2 R_{\odot}$ ) are seen associated with a large quiescent filament in the northern hemisphere and with the fragmentary remains of a filament in the SE quadrant of the disc.

It may be seen from Figure 1 that in the vicinity of active regions and over large areas of the solar surface the lower corona has a closed loop configuration. This implies both inhibited coronal expansion and inhibited radial heat conduction in these regions. There are however certain areas of the disc which appear almost free from any transverse field constraints. In particular we note the large area of reduced X-ray emission, a 'hole' in the corona, situated somewhat to the west of central meridian, extending from N20W20 to almost the south pole. An expanded view of this region together with  $H\alpha$  and CaK photographs of the underlying chromosphere and a Kitt Peak longitudinal field magnetogram for the following day are shown in Fig 2. The bright spots seen in the X-ray image are low lying, relatively hot regions associated with small, isolated bipolar areas. The soft X-ray structures surrounding the hole appear to diverge from it both to the east and the west. The open form of the hole is thus clearly defined. Comparison with the magnetogram shows the underlying longitudinal field configuration to be quite distinctive. Strips of negative field (black) are seen to border the hole in the southern hemisphere joining in the vicinity of the equator to form a large, predominantly negative area. On the evidence of the X-ray image, the southern strips form the foot points of tubes of force which extend away from the hole, the eastern one forming an arch above the broken filamentary structure seen in  $H\alpha$ , the western one forming a complex of activity with

active regions nearer the limb. Connections into the hole are scarce. Very little structure may be seen in either  $H\alpha$  or CaK pictures within the hole although there is evidence of a slight reduction in the intensity of the chromospheric network emission from the area under the coronal hole visible in the CaK image. This behavior was also reported by Munro and Withbroe (1972) in a study of holes observed in EUV emission from OSO-IV. In each case studied, little evidence of the features was found in lines or continuum formed at temperatures below 800,000 K except for the HeI and HeII emission. It may be that the reduced CaK emission provides further evidence of the weakness of the magnetic field in the hole region at chromospheric levels.

Altschuler and Trotter (private communication) have provided an extrapolation of the photospheric magnetic field into the corona according to the potential field approximation of Altschuler and Newkirk (1969). The resulting potential field map for 24 November 1970 is shown in Fig 3. While the detailed agreement between the computed field distribution and the observed X-ray emitting structure is not good (the north-south alignment of the hole being probably an artifact of the computation), the general features of the X-ray structures are represented. In particular, the inferred magnetic structure bordering the hole region is similar to the X-ray structures shown in Figure 2. We therefore conclude that the magnetic field in the hole region is quite weak and is primarily radial, and that at the boundaries the field arches away from the hole.

The magnetic field thus inferred for the hole region fulfills the divergent field requirement for the source of a high velocity wind stream (Billings and Roberts, 1964; Davis, 1965; Pneuman and Kopp, 1971; Gosling et al., 1972; Pneuman, 1972). There are

however two other properties of such a structure which are also predicted by both Gosling et al. (1972) and Pneuman (1972). These are that in such regions the coronal density should be significantly lower than in the closed magnetic regions and that, because of the uninhibited thermal conduction outward along the open magnetic field lines the temperature may also be lower than in the closed regions.

## 2b) Physical Condition in the Coronal Hole

In order to obtain temperature and density measures from X-ray observations it is necessary to digitize the images obtained on a microdensitometer and then to convert the measured photographic densities to energies using laboratory calibration curves. Thereafter the coronal temperature may be evaluated by two methods: (a) The analysis of measured radial intensity profiles of the coronal limb brightening, and (b) the determination of the ratio of energy fluxes measured through pairs of broadband filters. In the second case a model spectrum (Tucker and Koren 1971) is required to interpret the data. The emission measure  $\int N_e^2 dl$  of the coronal plasma and hence its density  $N_e$  may only be determined by the use of the model spectrum.

In order to estimate the vertical distribution of the X-ray emitting material seen on November 24, 1970 radial microdensitometer scans were performed through the limb of the image shown in Fig. 1. Fig 4 shows the results of radial scans passing through the hole at the limb (at an angle of  $195^\circ$  clockwise from the vertical) and through a typical area of limb brightening (at  $356^\circ$  clockwise) which was assumed to be a closed region according to the discussion of Van Speybroeck, et al. (1970).



Beyond the limb the data are well fitted by a simple exponential function of the form:

$$I(h) = I(0) \exp (-h/h_I) \quad (1)$$

where  $I$  is the X-ray energy deposited on the film per unit area and unit time,  $h$  is the height above the limb,  $I(0)$  is the energy deposited at height  $h = 0$ , and  $h_I$  is an intensity scale height.

The closed structure selected was one of five, four of which had scale heights lying in the range  $6.62 \times 10^4 < h_I < 8.24 \times 10^4$  km. It is apparent that the intensity scale height,  $h_I = (3.27 \pm 0.12) \times 10^4$  km, in the hole is approximately half that in the typical closed structures.

In general, after corrections have been made for the scattering function of the telescope, the energy deposited on the film at any point by a plasma at temperature  $T$  is given by

$$I(h) = C \int N^2(h) \, ds \int_{\lambda_1}^{\lambda_2} E(\lambda, T) \, \eta(\lambda) \, d\lambda = C \cdot F(T) \int N^2(h) \, ds \quad (2)$$

where  $C$ , a constant, is a function of the telescope geometry,  $E(\lambda, T)$  is the specific emission per unit emission measure at wavelength  $\lambda$ ,  $F(T) = \int_{\lambda_1}^{\lambda_2} E(\lambda, T) \, \eta(\lambda) \, d\lambda$  and depends only on temperature for any given filter type, and  $\eta(\lambda)$  is the wavelength sensitivity function of the telescope, filter, film combination whose passband is  $\lambda_1$  to  $\lambda_2$ .

If we interpret intensity distributions at the limb, which are represented by equation (1), as radiation from an isothermal atmosphere with spherical symmetry about the limb and density  $N(h) = N_0 \exp(-h/H)$  where  $H$  is the density scale height,  $N_0$  is the density at the base of the corona ( $h=0$ ), and the radial variation of the gravitational potential has been neglected, then the emission measure along the line of sight at height,  $h$ , above the

limb is given by the expression

$$\int N^2(h) ds = 2 N^2(h) \frac{H}{2} \sqrt{\frac{\pi(R_0 + h)}{H}} \quad (3)$$

At the heights considered in this study, this may be combined with equation (2) to give

$$I(h) = C N_0^2 \sqrt{\pi R_0 H} \left( \exp \frac{(-2h)}{H} \right) \left( 1 + \frac{h}{2R_0} \right) F(T) \quad (4)$$

Thus, to a good approximation, we may take

$$h_I = \frac{H}{2} \quad (5)$$

Hence the density scale height in the hole is equal to  $6.54 \times 10^4$  km, and is approximately half the value in the closed regions.

In the case of a radial line of sight through an exponential, isothermal atmosphere, equation (2) becomes

$$I = C F(T) N_0^2 \frac{H}{2} = C F(T) N_0^2 h_I \quad (6)$$

The temperatures of the hole and of the closed structure can be derived from the measured scale heights if we assume that the plasma is in hydrostatic equilibrium under the influence of gravity only. In this case, the density scale height

$$H = \frac{kT}{\mu m g_0} \quad (7)$$

where  $\mu$  is the mean molecular weight (0.62) and  $g_0$  is the acceleration of gravity at the solar surface. Numerical evaluation of equation (7) using the results of equations (1) and (5) leads to a temperature of  $1.3 \times 10^6$  K in the hole and  $3.1 \times 10^6$  K in the typical structure.

The hole coronal base temperature of  $1.3 \times 10^6$  K is consistent with the temperature derived from the EUV observations of Munro and Withbroe (1972). However, this value should be regarded as a lower limit since any coronal expansion would reduce the scale height at a given temperature relative to that in a static atmosphere (Parker, 1963).

The X-ray image shown in Figure 1 was taken through a 0.85 micron thick Parylene N\* +2500 Å aluminum filter, the resulting passband being approximately 3-35 Å and 44-51 Å ( $\geq 1\%$  level). The longest exposures through thin Beryllium filters (passband 3-18 Å) taken during the same flight showed only faint traces of the closed structures. When this fact is interpreted in terms of the model spectrum, it implies that the temperature of this plasma was lower than that generally associated with active regions ( $2-3 \times 10^6$  K). Thus the 'temperature' derived for the typical closed structure from the scale height is inconsistent with our other determination of general coronal temperatures.

The discrepancy may be taken as proof of the closed nature of the structures, since it may be predicted from consideration of the forces on a plasma element in a closed field configuration.

The presence of the magnetic field will modify the radial density distribution of the plasma, and the assumption of pure gravitational hydrostatic equilibrium will be invalid. By equating the magnetic energy of  $\frac{B^2}{8\pi}$  with the kinetic energy of the gas,  $3kNeT$ , we may obtain a rough estimate of the necessary magnitude of the constraining field. Using the results derived below, the

---

\* Parylene N is the Union Carbide tradename for unsubstituted polyxylylene.



required value of  $B$  is found to be approximately 6 gauss. This is considered to be a not unreasonable value.

Application of equations (4) and (6) to the hole and the closed structures at the base of the corona ( $h=0$ ) results in the ratios

$$\frac{I(0) \text{ hole}}{I(0) \text{ closed}} = \frac{N_o^2 \text{ (hole)}}{N_o^2 \text{ (closed)}} \sqrt{\frac{h_1 \text{ (hole)}}{h_1 \text{ (closed)}}} \frac{F(T) \text{ hole}}{F(T) \text{ closed}} \quad (8)$$

$$\text{and} \quad \frac{I(0) \text{ hole}}{I(0) \text{ closed}} = \frac{N_o^2 \text{ (hole)}}{N_o^2 \text{ (closed)}} \frac{h_1 \text{ (hole)}}{h_1 \text{ (closed)}} \frac{F(T) \text{ hole}}{F(T) \text{ closed}} \quad (9)$$

respectively.

These expressions may be used to obtain an estimate of the true temperature of the closed region if it is assumed that the coronal base density is constant and that the difference in emission from the hole region and the closed region is due both to a difference in temperature and to the effect of the transverse field. In this case, substituting the measured values of the intensity scale heights  $h_1 \text{ (closed)}$  and  $h_1 \text{ (hole)}$  measured at the limb and the disc measurement of the hole and closed region energy fluxes  $I(0)$  into equation (9), one finds that

$$F(T) \text{ hole} / F(T) \text{ closed} = 0.85^{+0.15}_{-0.25} \quad (10)$$

If we further assume that the temperature at the base of the hole is the derived barometric temperature of  $1.3 \times 10^6 \text{ K}$ , then evaluation of  $F(T)$ , using the computed X-ray spectrum (Tucker and Koren, 1971) gives  $T_{\text{closed}} = 1.5^{+0.1}_{-0.2} \times 10^6 \text{ K}$ .

An alternative interpretation of the data is possible if the temperatures in the hole and in the closed structures are taken as

equal. (This is equivalent to an assumption that the observed differences in the scale heights can be attributed entirely to the geometry of the coronal magnetic fields.) Under these conditions, assuming that the scale heights measured at the limb are valid near the center of the disc and that  $F(T)_{\text{closed}} = F(T)_{\text{hole}}$ , the ratio of the density at the base of the coronal hole to the density in the closed structures evaluated from equations (8) and (9) becomes

$$\frac{N_o(\text{hole})}{N_o(\text{closed})} = 0.91 \pm 0.14 \quad (11)$$

using the limb measurements and

$$\frac{N_o(\text{hole})}{N_o(\text{closed})} = 0.92 \pm 0.09 \quad (12)$$

using the disk measurements.

This is a lower limit to the density ratio. If the temperature at the base of the closed structure is in fact higher than the temperature at the base of the hole then (because the specific emission in the filter passband,  $F(T)$ , is an increasing function of temperature) the ratio  $N_o(\text{hole})/N_o(\text{closed})$  may increase.

Table 1 presents possible alternative models that are compatible with the X-ray observations. The densities quoted are computed from equation (5) using a value of  $1.14 \times 10^{-6}$  for the constant  $C$ .

Table 1

## Physical Conditions at the Base of Coronal Structures

	Hole	Closed
<hr/>		
Measured....		
Scale height ( $h_I$ )	$(3.27 \pm .12) \times 10^4 \text{ km}$	$(7.69 \pm .21) \times 10^4 \text{ km}$
Equatorial X-ray		
Intensity	$0.02 \pm .01 \text{ erg cm}^{-2} \text{ sec}^{-1}$	$.055 \pm .015 \text{ erg cm}^{-2} \text{ sec}^{-1}$
( $3-35 \text{ \AA}$ and $44-51 \text{ \AA}$ )		
<hr/>		
Derived....	Hydrostatic limit	
Barometric temperature	$1.3 \times 10^6 \text{ K}$	$3.1 \times 10^6 \text{ K}$
<hr/>		
Derived....	Constant temperature models:	
	$N_O(\text{hole}) = 0.91 \pm 0.14 N_O(\text{closed})$	
Temperature	$1.3 \times 10^6 \text{ K}$	$1.3 \times 10^6 \text{ K}$
Density	$2.7 \times 10^9 \text{ cm}^{-3}$	$2.9 \times 10^9 \text{ cm}^{-3}$
<hr/>		
Derived....	Constant density models:	
	$N_O(\text{hole}) = N_O(\text{closed})$	
Temperature	$1.3 \times 10^6 \text{ K}$	$1.5 \times 10^6 \text{ K}$
Density	$2.7 \times 10^9 \text{ cm}^{-3}$	$2.7 \times 10^9 \text{ cm}^{-3}$



It is apparent that the variations in the values of temperature and density at the base of the corona computed for the hole and the closed region in the two extreme cases considered are small. The substantial variation in observed X-ray intensity can be attributed almost entirely to the difference in density scale height between the hole and the closed region, which in turn is an effect of the associated coronal magnetic field configuration rather than of any significant differences in the physical conditions at the base of the corona.

The absolute value of the X-ray intensity from large scale diffuse features is critically dependent on the value calculated for the scattered background. Thus the presence of strongly emitting active regions at near equatorial latitudes introduces large systematic uncertainties into the absolute value of the intensity of the nearby diffuse structures. However, because these systematic errors effect both the hole and the closed structure in the same way, the errors incurred in the density ratio determination are substantially reduced. The specific values of density and  $T_{\text{closed}}$  which are presented are dependent on the absolute calibration of the X-ray telescope system, and the accuracy of the Tucker and Koren (1971) spectrum. Accordingly, these values are also of lesser reliability than the relative ratios of measured quantities.

### 3. Solar Wind Mapping

The fact that well defined high velocity streams are frequently seen to recur with a periodicity of about 27 days suggests a definite coupling with the solar corona. However, the values of electron temperature, proton temperature, particle density and bulk velocity measured at 1 AU all tend to be modified by stream - stream interactions in the interplanetary medium (Hundhausen, 1970). Goldstein (1971) has shown that stationary bulk velocity

variations generated near the solar surface should be substantially altered in shape, appearing at 1 AU with steepened leading edges and flattened trailing edges and with a density enhancement preceding the peaks.

These effects are essentially non-linear and hence not describable by linearized azimuthal perturbations (see Hundhausen, 1970 for a summary of linear analyses). In a study similar to Goldstein (1971), Sakurai (1971) proposed the QRH (quasi-radial hyper-velocity) approximation to describe non-linear effects. It consists of the assumption that the sonic and Alfvén Mach numbers are large and that the effects of gravitational potential and azimuthal convection may be neglected. The result is that the QRH approximation to the radial velocity  $V_r$  as a function of solar azimuth  $\phi$  is simply equal to  $V_{r0}(\phi_0)$ , the initial velocity of the stream at longitude  $\phi_0$  at some radius  $\tilde{r}$  beyond the magnetohydrodynamic critical points. To the same approximation  $\phi - \phi_0 = (\Omega \tilde{r} V_{r0}) (r - \tilde{r})$ , i.e., the plasma streamlines beyond  $\tilde{r}$  are ideal Archimedean spirals for a sidereal rotation rate  $\Omega$  along which the radial velocity is constant at the instantaneous observed velocity.

In a later study, Matsuda and Sakurai (1972) included azimuthal convection and magnetic field terms in the non-linear calculation (thus refining the QRH approximation to a simple "H", or hypervelocity approximation), and concluded that the modified azimuthal profile of  $V_r$  was "essentially the same as the case without magnetic field". The important physical role of the "H" approximation is to allow the calculated plasma density and field intensity to remain finite at a stream-stream interface.

It therefore seems plausible that the constant-velocity, ideal-spiral QRH approximation may, despite its apparent crudeness, be satisfactory for tracing the locus of solar wind plasma back to the longitude where it was "released" from the corona.

This "release zone" beyond the critical points may be many solar radii out from the sun. Matsuda and Sakurai (1972) used the estimates of Weber and Davis (1967) for the critical points and chose  $\tilde{r} = 30 R_{\odot}$ . The most probable region of deviation of the approximation is at the stream-stream interface, i.e., the brief sharp increase prior to the peak of the leading edge of a fast stream. However, the much longer remainder of the customary "saw-tooth" profile of the stream may be well represented by the QRH approximation. To support this contention, Nolte and Roelof (1972) in their study of solar wind mapping, took the streamlines calculated from the non-linear analysis of Goldstein (1971) and compared them with the constant-velocity, ideal spiral approximation. Fig 5, taken from their work, shows the calculated azimuthal profile of the radial velocity  $V_r$  at  $155 R_{\odot}$  (Figure 5d) produced by a steady azimuthal profile at  $10 R_{\odot}$  of the form  $V_{r0}(\phi_0) = 350 \text{ (km/sec)} (1 + \cos \phi_0)$  shown in Figure 5a. The constant velocity trajectories (straight lines in an  $r - \phi$  plot) derived from Figure 5d are drawn and labeled with their velocities in Figure 5c above it. Figure 5b shows Goldstein's calculated (curved) streamlines with the constant velocity trajectories redrawn for comparison.

The errors in Figure 5 between the inferred solar "source" longitude (at  $r = 0$ ) and the "actual" source longitude (at  $r = 10 R_{\odot}$ ) never exceed  $10^\circ$ . Moreover, these largest errors occur only in the fast-slow interaction during the rise of the velocity, as expected from the discussion of the previous paragraph. Figure 5 also indicates why the simple approximation works: two errors tend to compensate each other. Firstly, the solar wind accelerates monotonically as distance increases (Parker, 1965), tending to place the extrapolated source too far east on the sun; but secondly, the azimuthal plasma velocity does not become negligible until the



"release zone", tending to place the extrapolated source too far west. The "release zone" effect appears in Figure 5 in the straight line portion of the streamlines closest to the source surface, while the "acceleration" effect is shown by the streamlines increasing in slope well away from the sun.

The constant velocity approximation was used by Snyder and Neugebauer (1966) to analyze the first interplanetary measurements of the solar wind (from Mariner 2). They concluded that either the approximation was wrong or "there is no close correlation between the plage regions and the solar streams." We believe the latter alternative is correct since, as we stated in the Introduction, it is more likely that the stream sources are in open magnetic configurations away from the closed structures observed over active regions. It is perhaps because many workers chose Neugebauer and Snyder's other alternative (that the mapping was inaccurate) that the mapping (in the QRH approximation) fell into disuse.

As opposed to a purely theoretical argument, successful correlation of interplanetary observations of low energy solar particles with the appropriate solar structures using the QRH approximation offers experimental support for its validity. With the additional assumption, also made by Matsuda and Sakurai (1972), that the interplanetary field lines approximately follow the QRH characteristics, quasi-stationary low energy solar particle events have been mapped back to the sun to infer their azimuthal coronal injection profile. Roelof (1972a) argued that the delayed  $\geq 45$  keV electron event of 8-9 July 1967 mapped back to the same solar longitude from two spacecraft  $\sim 45^\circ$  apart, even though the solar wind configuration was noticeably evolving between the spacecraft. Proton and alpha particle fluxes  $\geq 0.3$  meV/nucleon from three well-separated spacecraft observed during three solar rotations in 1967 (Krimigis et al., 1971), were synthesized with interplanetary plasma and magnetic

field observations (Roelof and Krimigis, 1972). The particle profiles were mapped back to the sun in the QRH approximation (using the solar wind velocity measured in the same spacecraft), and compared directly with magnetic structures inferred from synoptic charts derived from  $H\alpha$  "filtergrams" (McIntosh, 1972). Roelof and Krimigis (1972) associated equatorial neutral line structures with changes in the 0.3 meV proton profiles on a scale  $\sim 10^\circ$ , and also associated several solar wind streams with inferred "open" coronal magnetic field configurations. In particular, the  $\geq 45$  keV electron events during this period that Lin (1970) had ascribed to an "open" cone of propagation were associated with a solar wind stream that mapped back to what appeared to be an open magnetic structure in the corona.

In Fig 6 QRH velocity maps are constructed from the Vela satellite preliminary solar wind velocities published in the NOAA ERL Reports of Solar-Geophysical Data (No. 316, Part 1) and from the data from the MIT plasma experiment on Pioneer VI generously provided by Dr. A. J. Lazarus. The constant-velocity approximation consists of assuming the field lines follow the locus of successive elements of plasma moving radially outward from the 'release zone' above their solar source longitude. On a map of the interplanetary medium in 'cylindrical coordinates' the locus of a plasma element will be a straight line with slope

$$\frac{dr}{d\phi} = \frac{V}{\Omega_{SID}}$$

where  $V$  is the solar wind velocity and  $\Omega_{SID}$  the angular velocity of the sun's siderial rotation. The trajectory of a satellite will be (to a good approximation) a line at constant  $r$  decreasing in  $\phi$  at a rate  $d\phi/dt = -\Omega_{SYN}$  which is the sun's apparent synoptic angular velocity as observed from the satellite. Inspection of Figure 6 reveals the similarity of the two sets of

observations even though the difference in time between the observation of a given feature at the two spacecrafts was over three days. Thus we conclude that the solar wind structure was nearly stationary. The period studied is dominated by a high velocity stream which can be seen in both sets of observations. Pioneer VI and Vela data also show the proton density to be below average during the passage of the stream. The inferred solar positions of the maxima of the stream in the Vela and Pioneer VI data, poorly defined because of incomplete coverage, differ by no more than 10 degrees, reflecting either some slight temporal variation in the source or merely the error in the approximation.

#### 4. Comparison of Solar Wind and X-Ray Data

In order to compare the longitudinal dependence of the solar wind structure with that of the diffuse X-ray emission, a swath 4 arc minutes wide was taken across the image shown in Figure 1 along the line of the Vela and Pioneer VI tracks. The resulting value of average X-ray energy flux plotted as a function of solar longitude is shown, together with the combined Vela and Pioneer VI velocity values in Fig 7. A striking agreement is seen between the position of the coronal hole and the peak of the high velocity stream. If we assume that the peak of the stream is actually located somewhere between the positions extrapolated from the Vela and Pioneer data, then the maximum of the stream lies slightly east of center of the hole. Agreement also exists between the magnetic polarity of the hole, inferred from the November 25, 1970, magnetograph (see Figure 2) and the polarity of the corresponding sector structure measured in the solar wind (Wilcox, private communication).

The significance of this result can be further tested by investigating the time history on previous rotations of both the



high velocity stream and the photospheric magnetic field distribution associated with the hole. Fig 8 shows the 'transit time' of the solar wind,  $\Delta t = (1 \text{ AU}) / V$ , plotted as a function of the date of measurement by the Vela spacecraft near Earth. Data from two Pioneer spacecraft, widely separated from Earth (Pioneer VI and VII, 50 degrees and 145 degrees east of Earth, respectively), are also plotted at the extrapolated date when the stream (assumed non-evolving) corotated past the Earth. Estimated corotation times are published with the solar wind data in the NOAA ERL Reports of Solar-Geophysical Data. The decay of solar wind streams is identifiable in a transit-time plot as a nearly linear increase in  $\Delta t$  with time after an initial rapid drop (corresponding to the sharp velocity rise of the stream). The stream is clearly seen as the dominant stationary feature (a minimum in  $\Delta t$  with approximately a 27 day recurrence throughout the three month period October-December 1970. The CMP time of the source (inferred from the intersection of the straight lines in Figure 8 with the time axis) falls near Carrington longitude 280 degrees on all three rotations. During December Vela coverage was too sparse to allow detection of the stream, although there is some evidence of it in the Ames Research Center Pioneer VI data published in Solar-Geophysical Data for that month. The signature of the stream is, however, seen in both January and February, 1971.

Since visual recognition of the typical underlying photospheric magnetic field configuration is difficult, the potential field approximation (Altschuler and Newkirk, 1969) was used by Altschuler and Trotter (private communication) to compute the coronal field configuration for three rotations centered about the period of the X-ray observations. The results of the computation, showing the recurrent open structure near Carrington longitude

270 degrees are shown in Figure 9.

Thus there is evidence that both the photospheric magnetic feature and the high velocity stream were long-lived and stable. A temporal correlation between the instants of appearance and disappearance of both features would lead to a positive proof of this correlation and, further, to an estimate of the lag between them. Unfortunately, this is not available because solar wind features can only be observed when the feature passes the spacecraft.

### Discussion

In the previous sections, it has been shown that the coronal hole, photographed on the ASE experiment on November 24, 1970, had many of the properties required for the production of a high velocity solar wind stream. The coronal magnetic maps for that solar rotation showed the basic magnetic configuration within the feature to be divergent, a result supported by visual inspection of the shape of the diffuse structure surrounding the hole. Within the hole the photospheric field strength was very low and the plasma appeared to be distributed in hydrostatic equilibrium, under the influence of gravity only, with a temperature, which in the absence of expansion, could have been as low as  $1.3 \times 10^6$  K. The density scale height within the height range observed ( $h \leq 0.2R_{\odot}$ ) was a factor of two lower in the hole than in the surrounding closed structures, in agreement with Pneuman's (1972) predictions.

When the solar wind bulk velocity for the period was extrapolated back to the sun, using the method of instantaneous ideal spirals, it was found that the peak of a conspicuous high velocity stream originated within the hole. Experimental and theoretical treatments of the extrapolation technique used indicate that it is probably accurate to  $\pm 10^\circ$  in longitude. Thus, within the limits of error of the method, the coronal hole is judged to have been the source of the stream. Evidence of the recurrence of both the

hole and the stream adds further weight to the argument.

The dependence of wind velocity on the coronal magnetic field configuration found in the analysis may help to explain the changes in the wind pattern seen during the period 1962 - 1970. An investigation by Gosling et al. (1971) on the distribution of solar wind bulk velocities during this period revealed that there was no consistent tendency for the yearly average solar wind speed to increase with increasing solar activity, implying that coronal temperature had little effect on the magnitude of the bulk velocity. Furthermore the frequency of occurrence of high wind speeds was higher near solar minimum than near solar maximum. The frequency of long duration, high velocity streams similar to the November 24, 1970 feature was investigated by Roelof (1972b). Thirty nine streams of duration longer than two days were identified in the Vela data between July 1965 and September 1967. Included in this set were two recurrent series in 1966, one clearly identifiable over three consecutive rotations and the other over five. Streams longer than two days were rare in the Mariner 2 data (1962) and in the period after 1967, the stream series shown in Figure 8 being the only one found in the Pioneer VI and VII data through 1970.

The possible cause of these variations in wind pattern becomes apparent when the associated variations in magnetic field are considered. A photospheric 'sector diagram' of longitudinal field between  $+8^{\circ}$  and  $-8^{\circ}$  latitude, including both magnitude and polarity (in contours of  $\pm 1, 2, 4, 8$  and  $16$  gauss) is shown in Fig 10 (Stenflo, 1972). The magnetic field structure during solar minimum (1962 - 1966) is seen to be either large scale, periodic and long-lived (1962 - 1963) or of extremely low magnitude (1964 - 1967). It should be noted that while smoothed sunspot numbers, six-month averages of  $10.7$  cm radio flux and K-corona radiance had all increased significantly by early 1966 (Gosling et al., 1971),



the longitudinal fields near the equator were still typical of the earlier part of the cycle until late 1967. Thus, during solar minimum the very large scale, regular nature of the photospheric magnetic fields would result in open (equatorial) coronal field configurations, thus favoring the formation of holes and hence of long-duration, high velocity wind streams. The characteristic stream duration and tendency toward recurrence of these streams thus appear to be a direct consequence of the large separations of the magnetic sources and their long lifetimes. From late 1967, however, the near equatorial magnetic field became more complex and variable implying an increase in the number of interconnecting structures in the vicinity of the equator and more rapid time variation in the form of these transverse field configurations. Thus high velocity streams which might 'leak out' from between these structures would tend to be both shorter in duration and would have less chance of recurrence than those formed earlier in the cycle.

We realize the limitations of comparing equatorial longitudinal photospheric magnetic fields configurations with yearly solar wind, bulk velocity distributions. Neither can show the relation between individual stream and field configurations. Our hypothesis should be tested by detailed comparison between individual solar wind streams, properly mapped back to the release zone, and coronal magnetic field configurations, for a time period comparable to that of the solar cycle.

### Figure Captions

- Figure 1 A photograph of the sun in 3-35 Å and 44-51 Å wave bands obtained on November 24, 1970 (258° CMP). East is toward the left, heliographic North is 3.4° CW of the top of the page.
- Figure 2 The appearance of the coronal hole and surrounding structure in (a) 3-35 Å and 44-51 Å X-rays; (b) photospheric magnetic field on November 25, 1970, with the approximate position of the November 24th disc marked (Courtesy of Kitt Peak National Observatory); (c) CaK spectroheliogram (Courtesy of Sacramento Peak Observatory); (d) H  $\alpha$  spectroheliogram (Courtesy of Sacramento Peak Observatory).
- Figure 3 Coronal magnetic map for November 24, 1970, 270° CMP (Courtesy of M. D. Altschuler). \*The photospheric magnetic field data used for the coronal field calculations were obtained by R. Howard of the Hale Observatories with the support of the Office of Naval Research.
- Figure 4 Graph of X-ray intensity as a function of radial position for the coronal hole and for a typical closed region. (November 24, 1970, 3-35 Å and 44-51 Å bandpass). The error brackets on the points represent the measurement errors, the data being quantized at the lowest levels. For each plot the intensity scale height,  $h_1$ , is determined from at least squares fit to the data.

- Figure 5 Comparison of calculations of Goldstein (1971) with QRH (quasi-radial hyper-velocity) approximation for solar wind streamlines (Sakurai 1971): (a) steady azimuthal profile of radial velocity at  $10 R_{\odot}$ ; (b) calculated streamlines and QRH approximations (straight lines); (c) QRH lines inferred from (d); (d) calculated profile of radial velocity at  $155 R_{\odot}$  (from Nolte and Roelof, 1972).
- Figure 6 Velocity and flux measures plotted as functions of connection longitude for Pioneer VI and Vela solar wind observations. (Pioneer VI data courtesy of A. J. Lazarus, Vela data from the NOAA, ERL Reports of Solar-Geophysical Data No. 316, Part I, 1970.)
- Figure 7 Comparison of (a) the intensity in the wavebands  $3-35 \text{ \AA}$  and  $44-51 \text{ \AA}$  emitted from an equatorial swath extending 4 arc min in latitude and with a 4 arc sec longitudinal sampling interval, and (b) the solar wind bulk velocity measured from Pioneer VI and Vela. (Pioneer VI data courtesy of A. J. Lazarus, Vela data from the NOAA, ERL Reports of Solar-Geophysical Data, No. 316, Part 1, 1970).
- Figure 8 The approximate transit time  $\Delta t$  of the solar wind (assuming constant radial velocity from the sun to the spacecraft) plotted as a function of date of measurement at the earth. In addition to data from Vela spacecraft, transit times of solar wind measured at Pioneer VI and Pioneer VII are also plotted at the time the solar wind streams measured by them would corotate past the earth if no evolution of the structure occurred.



Figure 9      Coronal magnetic field maps for  $270^\circ$  CMP on (a) 27 October 1970, (b) 24 November 1970 and (c) 21 December 1970 (courtesy of M. D. Altschuler). The photospheric magnetic field data used for the coronal field calculations were obtained by R. Howard of the Hale Observatories with the support of the Office of Naval Research.

Figure 10     Sector diagram of the photospheric magnetic field close to the equator (between latitudes  $+8^\circ$  and  $-8^\circ$ ). The contour levels correspond to  $\pm 1, 2, 4, 8$  and 16 gauss (Stenflo, 1972).

## 7. Acknowledgements

The authors would like to thank A. Lazarus of M. I. T. and M. Altschuler and D. Trotter of the High Altitude Observatory for providing data prior to their publication. At AS&E, L. Van-Speybroeck and G. Vaiana participated in the sounding rocket flight which produced the X-ray photograph used in this analysis. J. Davis provided numerous helpful comments in discussion. T. Barrett, R. Haggerty and D. Webb contributed to the data reduction and analysis. At U. N. H., J. Nolte participated in the solar wind analysis. This work was supported in part by NASA under contracts NASW-2240 and NASW-2346.

## REFERENCES

- Altschuler, M. D. and Newkirk, G., Jr.: 1969, *Solar Phys.* 9, 131.
- Altschuler, M. D. and Perry, R. M.: 1972, *Solar Phys.* 23, 410.
- Altschuler, M. D., Trotter, D. E. and Orrall, F. Q.: 1972, 'Coronal Holes', submitted to *Solar Phys.*, abstract in *Solar Phys.* 25, 257, 1972.
- Billings, D. E. and Roberts, W. O.: 1964, *Astrophys. Norveg.* 9, 147.
- Couturier, P. and Leblanc, Y.: 1970, *Astron. and Astrophys.* 7, 254.
- Davis, L.: 1965, in R. Lust (ed.), *Stellar and Solar Magnetic Fields*, North Holland Publishing Co., Amsterdam, 204.
- Goldstein, B. E.: 1971, 'Nonlinear Corotating Solar Wind Structure', MIT preprint CSR-P-71-63.
- Gosling, J. T., Hansen, R. T. and Bame, S. J.: 1971, *J. Geophys. Res.* 76, 1811.
- Gosling, J. T., Hundhausen, A. J., Pizzo, V. and Asbridge, J. R.: 1972, *J. Geophys. Res.*, 77, 5442.
- Hundhausen, A. J.: 1970, *Rev. Geophys. and Sp. Phys.* 8, 729.
- Krieger, A. S., Vaiana, G. S. and Van Speybroeck, L. P.: 1970, in R. Howard (ed.) *'Solar Magnetic Fields'*, IAU Symp. 43, 397.
- Krimigis, S. M., Roelof, E. C., Armstrong, T. P. and Van Allen, J. A.: 1971, *J. Geophys. Res.* 76, 5921.
- Lin, R. P.: 1970, *Solar Phys.* 15, 453.
- Matsuda, T. and Sakurai, T.: 1972, *Cosmic Electrodyn* 3, 97.
- McIntosh, P. S.: 1972, *Rev. Geophys. and Space Science* 10, 837.



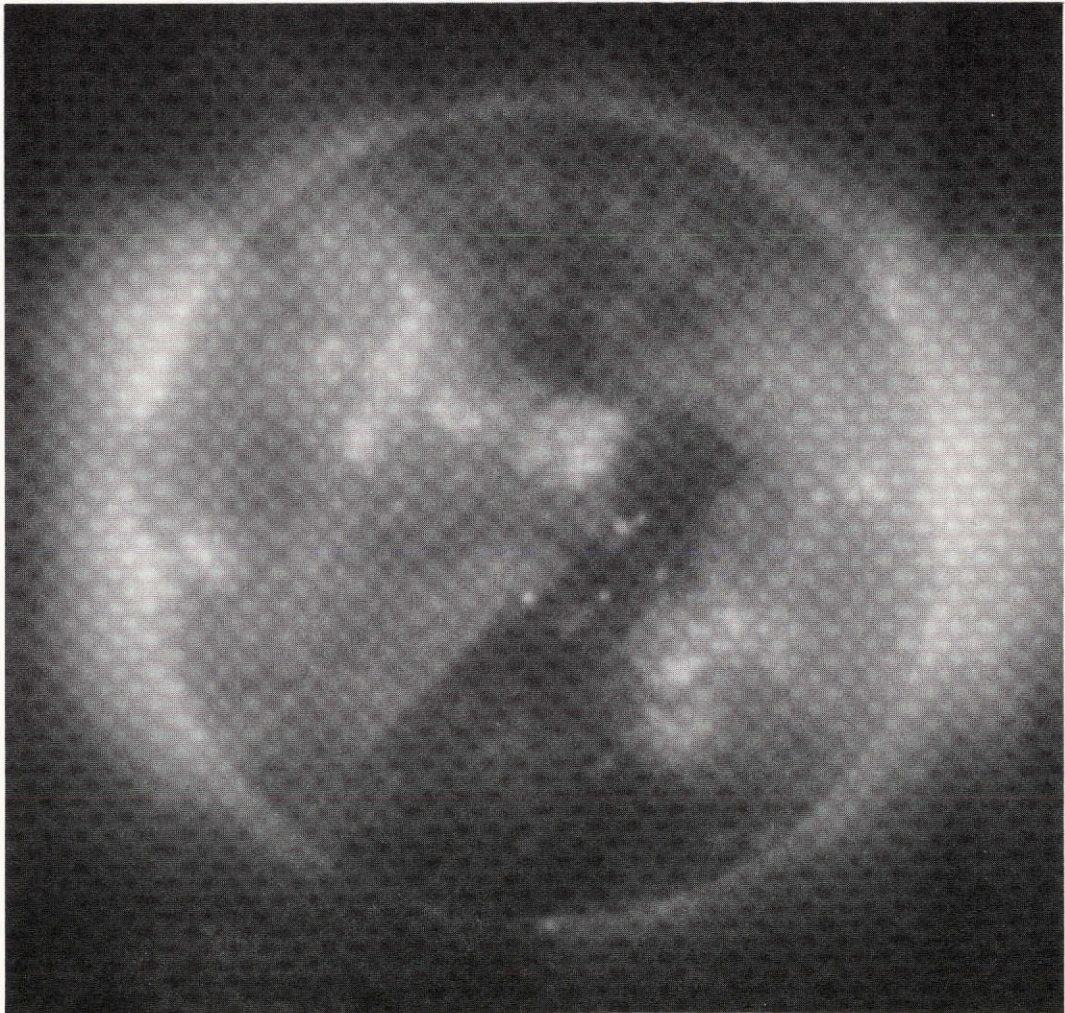
- Munro, R. H. and Withbroe, G. L.: 1972, 'Properties of a Coronal Hole from EUV Observations', Harvard College Observatory TR-31.
- Newkirk, G., Jr. and Lacey, L.: 1970, Nature 226, 1098.
- Nolte, J. T. and Roelof, E. C.: 1972, 'Mapping of the Large Scale Interplanetary Field from Multispacecraft Solar Wind Data' (abstract), EOS 53, 506, manuscript in preparation.
- Parker, E. N.: 1963, Interplanetary Dynamical Processes, Interscience, New York.
- Parker, E. N.: 1965, Space Sci. Rev. 4, 666.
- Pathak, P. N.: 1971, Solar Phys. 20, 462.
- Pneumann, G. W.: 1972, 'The Solar Wind and the Temperature-Density Structure of the Solar Corona', submitted to Solar Phys.
- Pneuman, G. W. and Kopp, R. A.: 1971, Solar Phys. 18, 258.
- Roelof, E. C.: 1972a, in C. Sonett, P. Coleman and J. Wilcox (ed.), 'Solar Wind', NASA SP-308, Washington D. C., 140.
- Roelof, E. C. and Krimigis, S. M.: 1972, 'Analysis and Synthesis of Solar and Interplanetary Energetic Particles, Plasma and Magnetic Field Observations over Three Solar Rotations', submitted to J. Geophys. Res. (preprint, Applied Physics Laboratory, The Johns Hopkins University).
- Roelof, E. C.: 1972b, 'Isolated Coronal Sources of Enhanced Solar Wind Velocity' (abstract), EOS 53, 506, manuscript in preparation.
- Sakurai, T.: 1971, Cosmic Electrodyn 1, 460.
- Stenflo, J. O.: 1972, Solar Phys. 23, 307.
- Snyder, W. C. and Neugebauer, M.: 1966, in R. J. Mackin (ed.), 'The Solar Wind', Pergamon Press.
- Tucker, W. H. and Koren, M.: 1971, Astrophys. J. 168, 283.

Vaiana, G. S.: 1970, 'Methods of Imaging X-ray Astronomy and the X-ray Spectroheliograph on ATM, ASE-2595.

Van Speybroeck, L. P., Krieger, A. S. and Vaiana, G. S.: 1970, Nature 227, 818.

Weber, E. J. and Davis, L., Jr.: 1967, Astrophys. J. 148, 217.

Wilcox, J. M.: 1968, Space Sci. Rev. 8, 258.

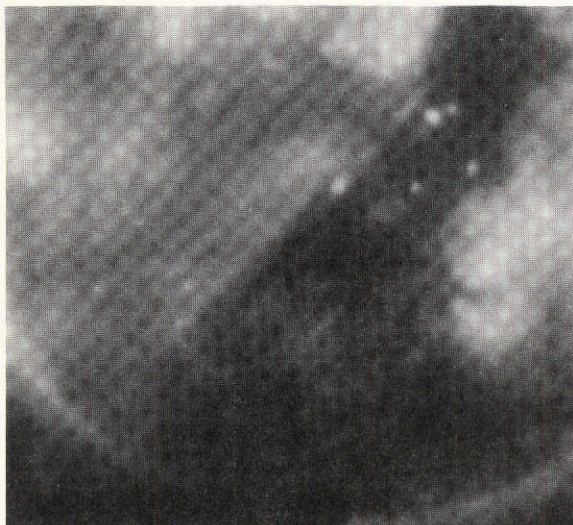


ER-011

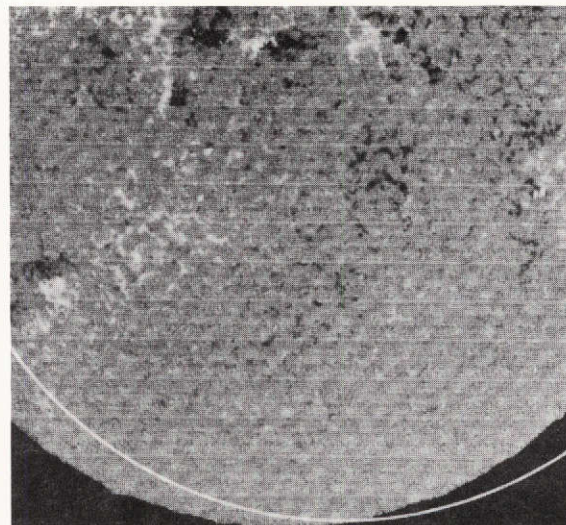
Figure 1

REPRODUCIBILITY OF THE  
ORIGINAL PAGE IS POOR

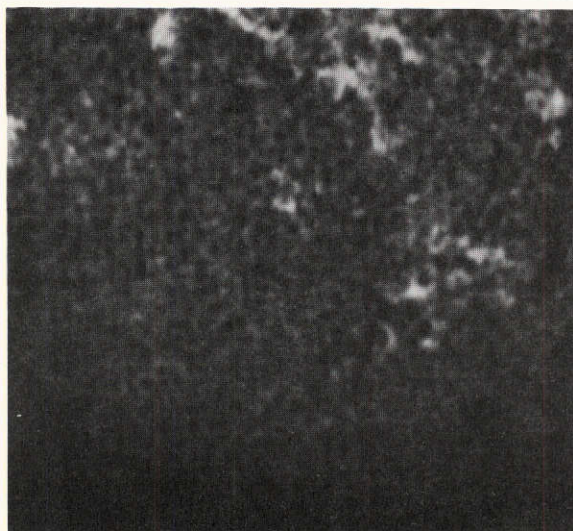




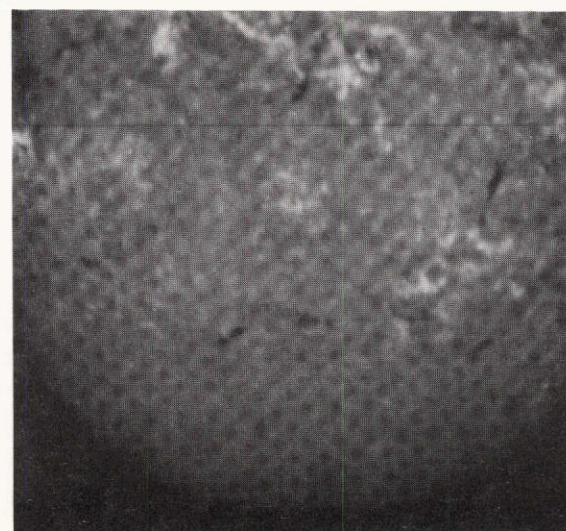
a



b



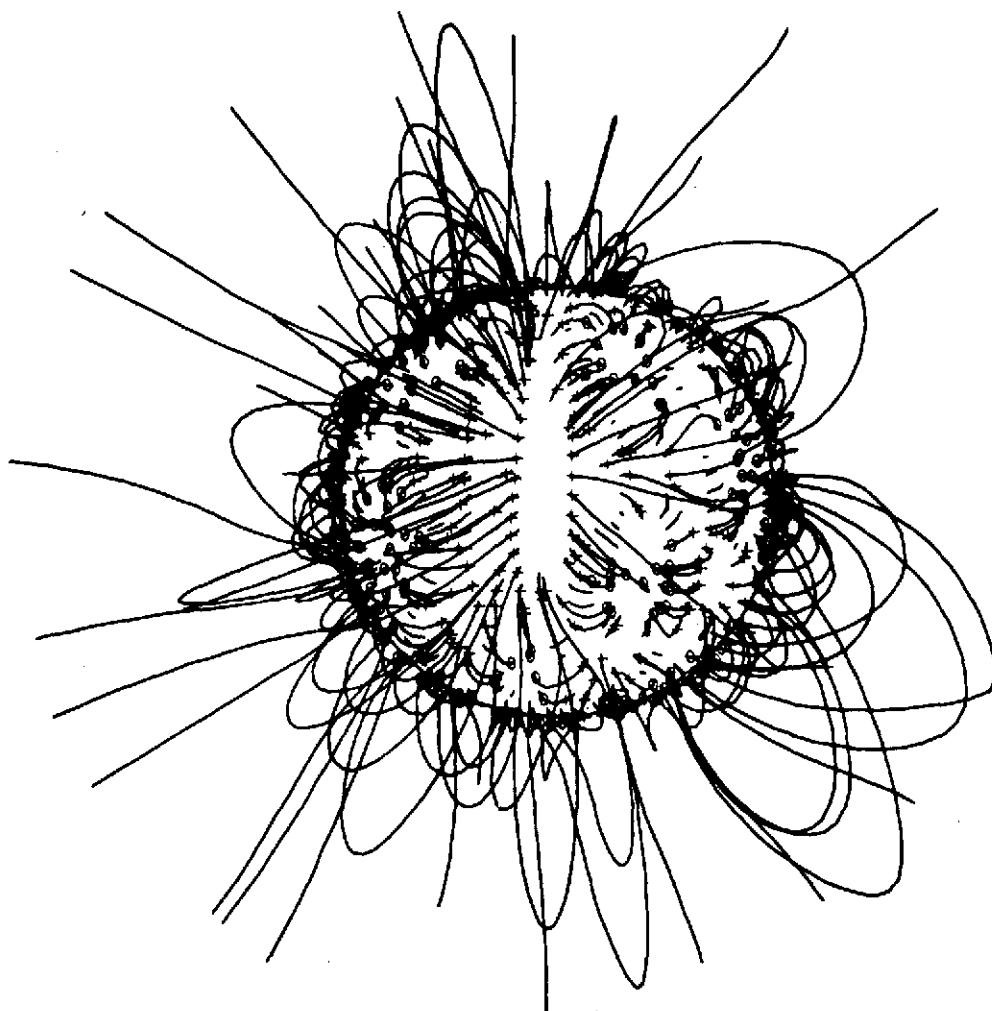
c



d

ER-031

Figure 2



**LONGITUDE OF DISK CENTER = 270 DEGREES**  
**DATE = 1970 DECEMBER -6.0    CENTRAL DAY = 1    ROT. 1568**

Figure 3

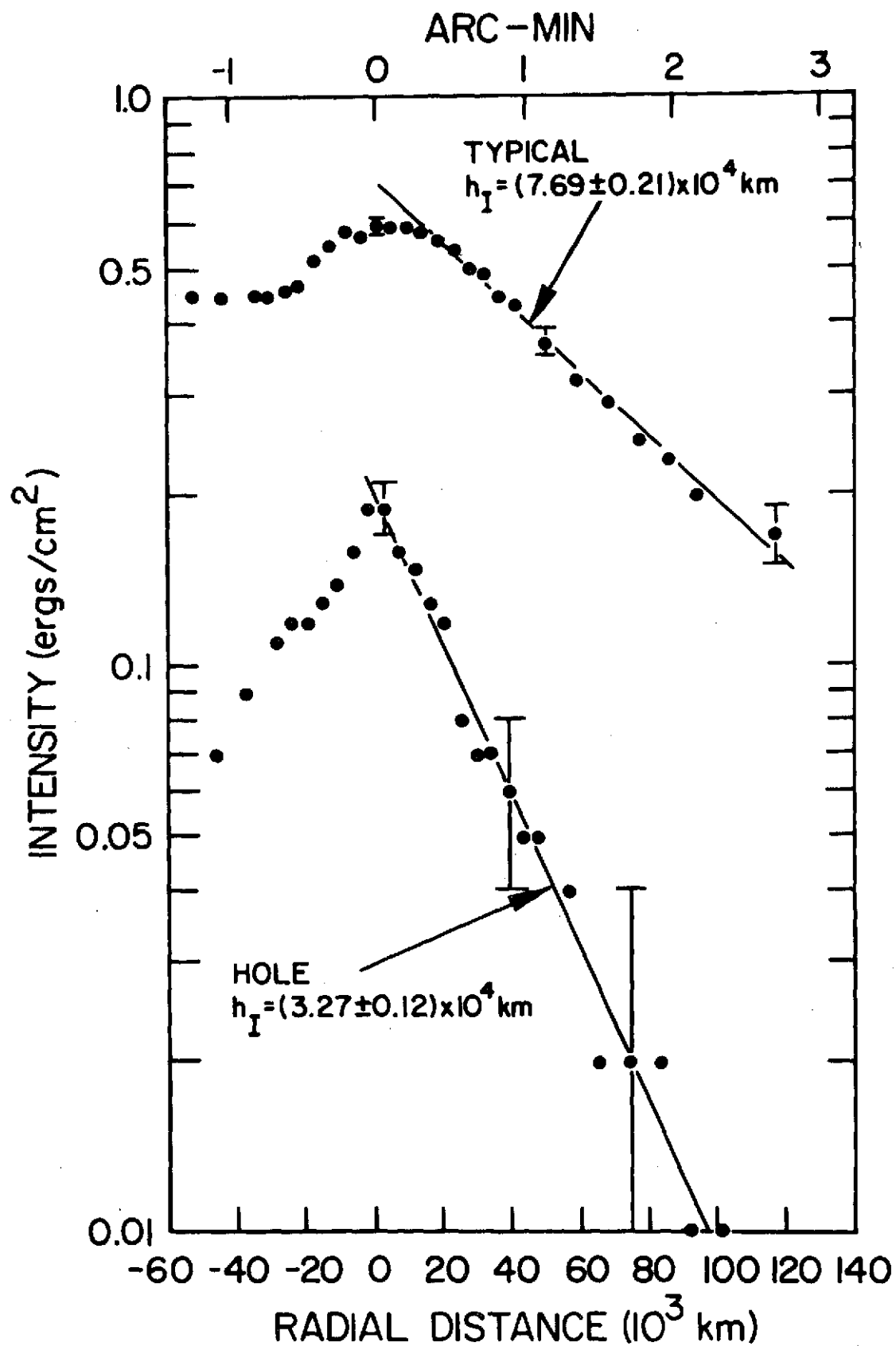


Figure 4



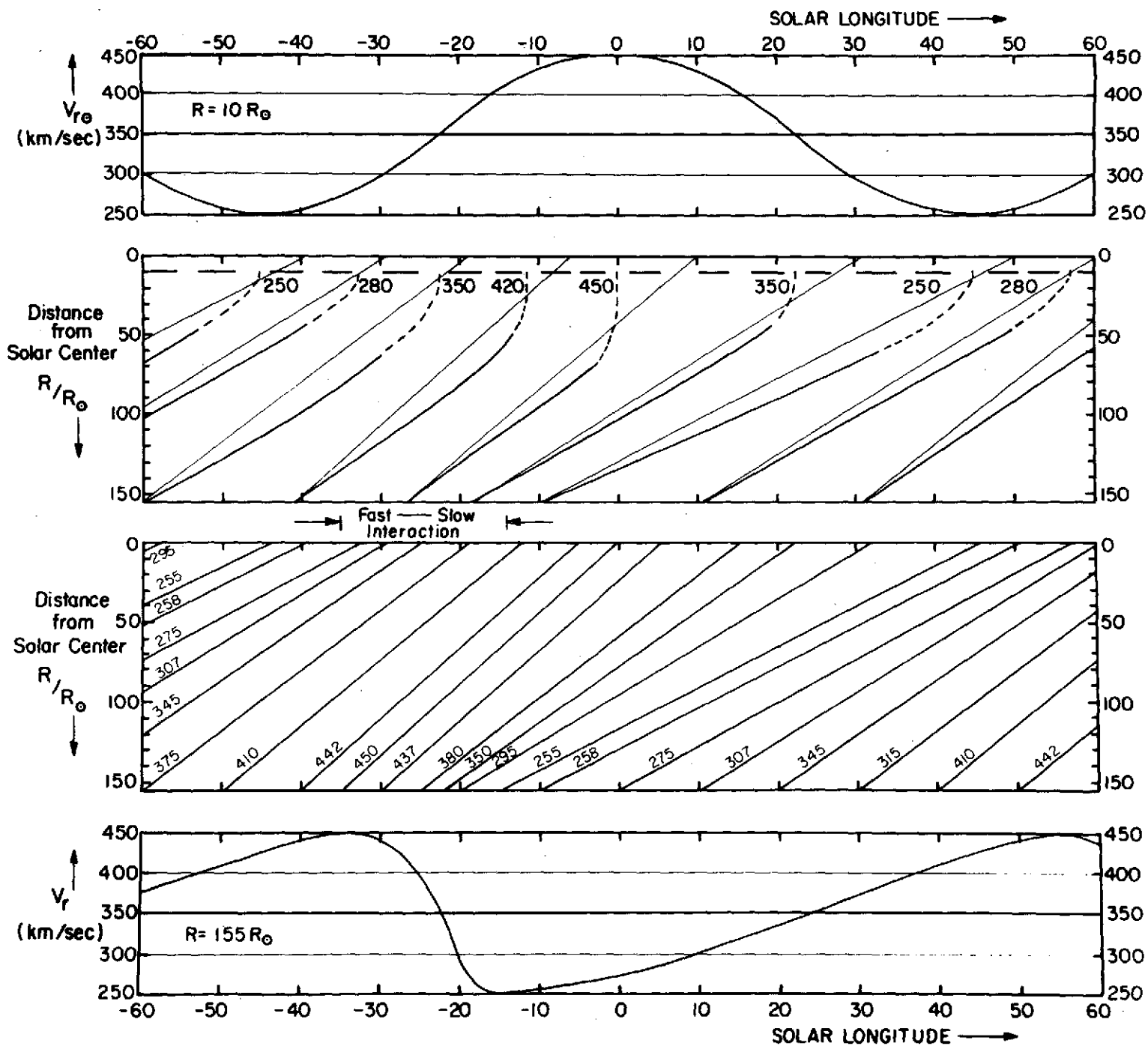
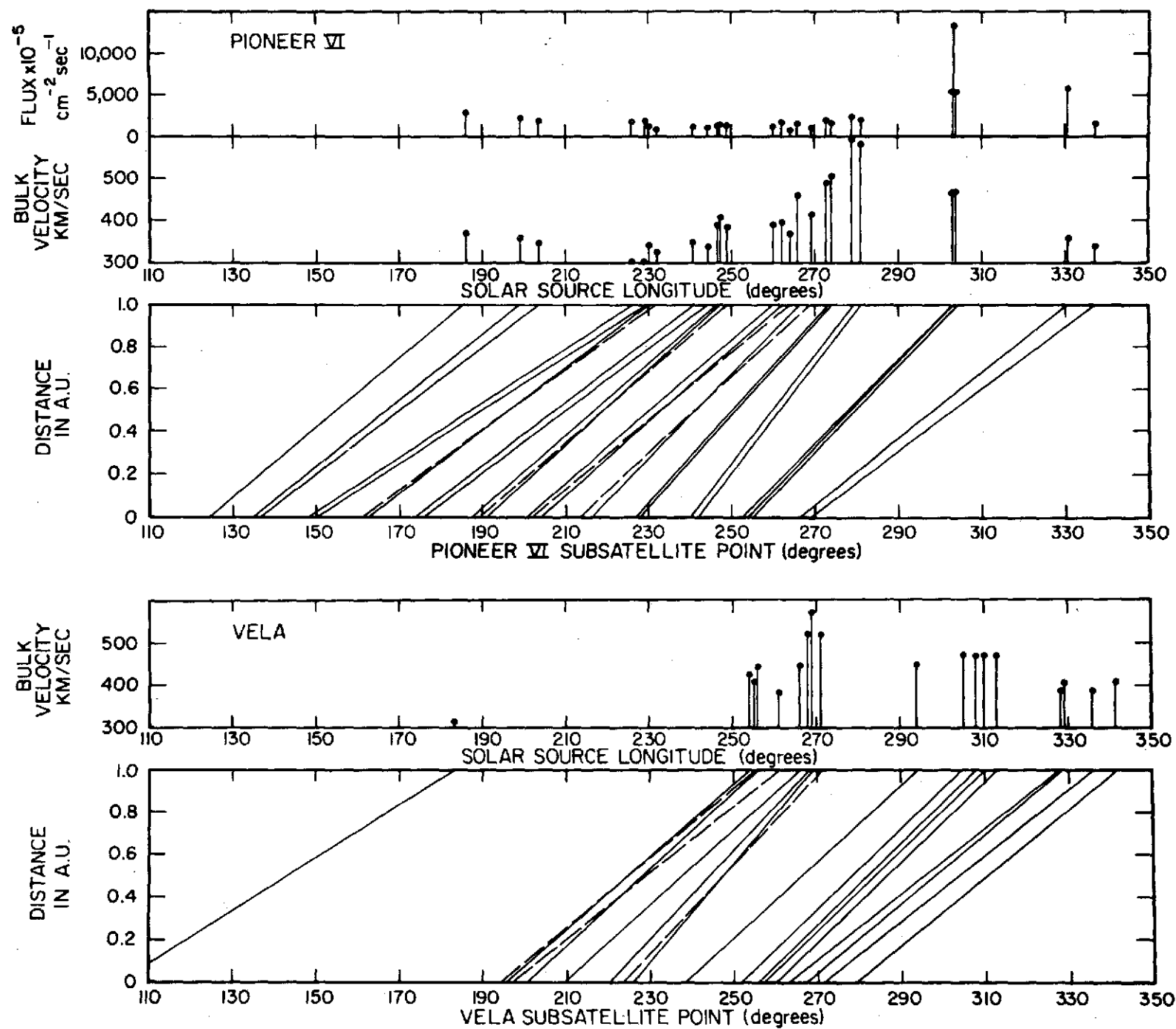


Figure 5

Figure 6



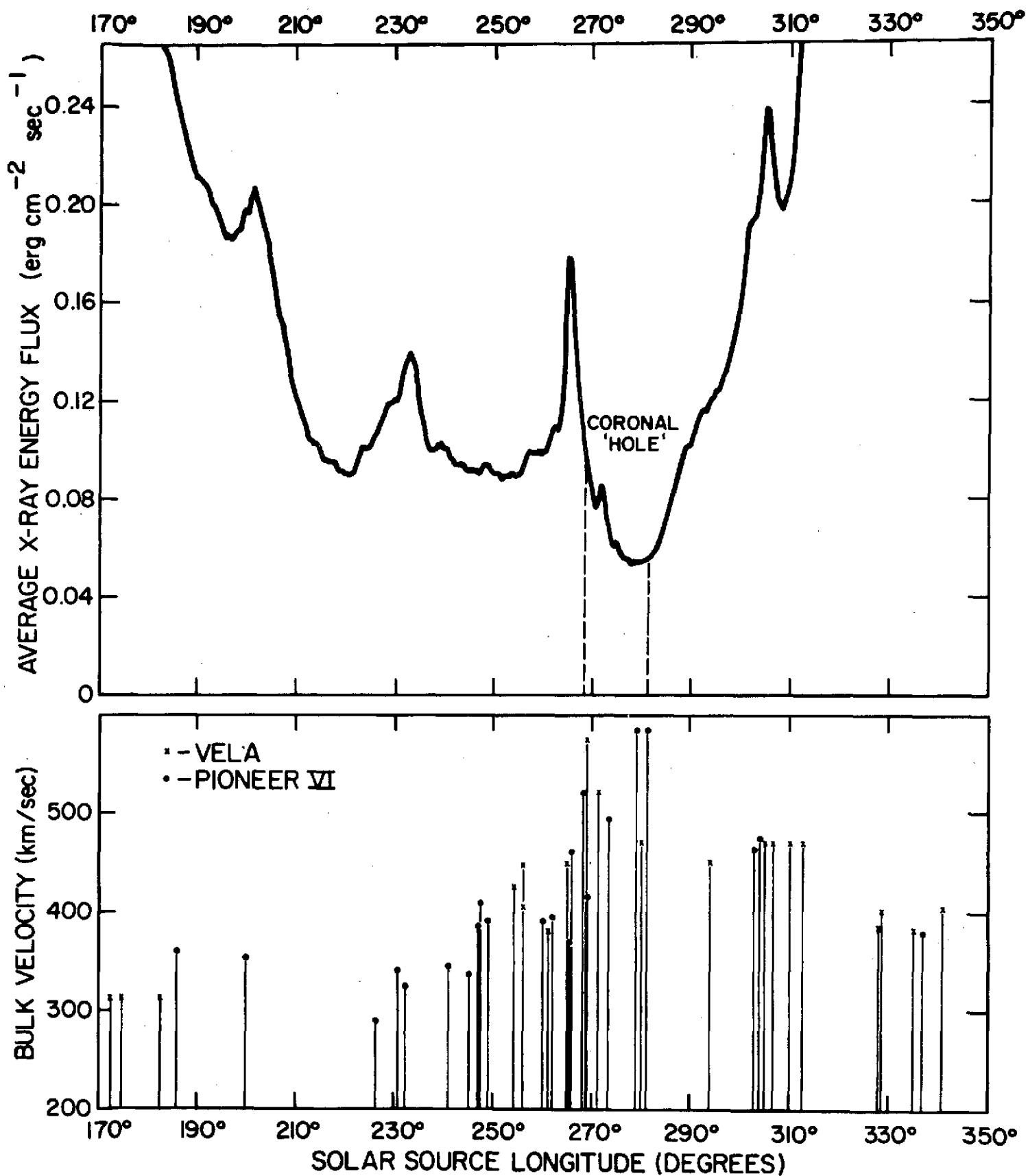


Figure 7



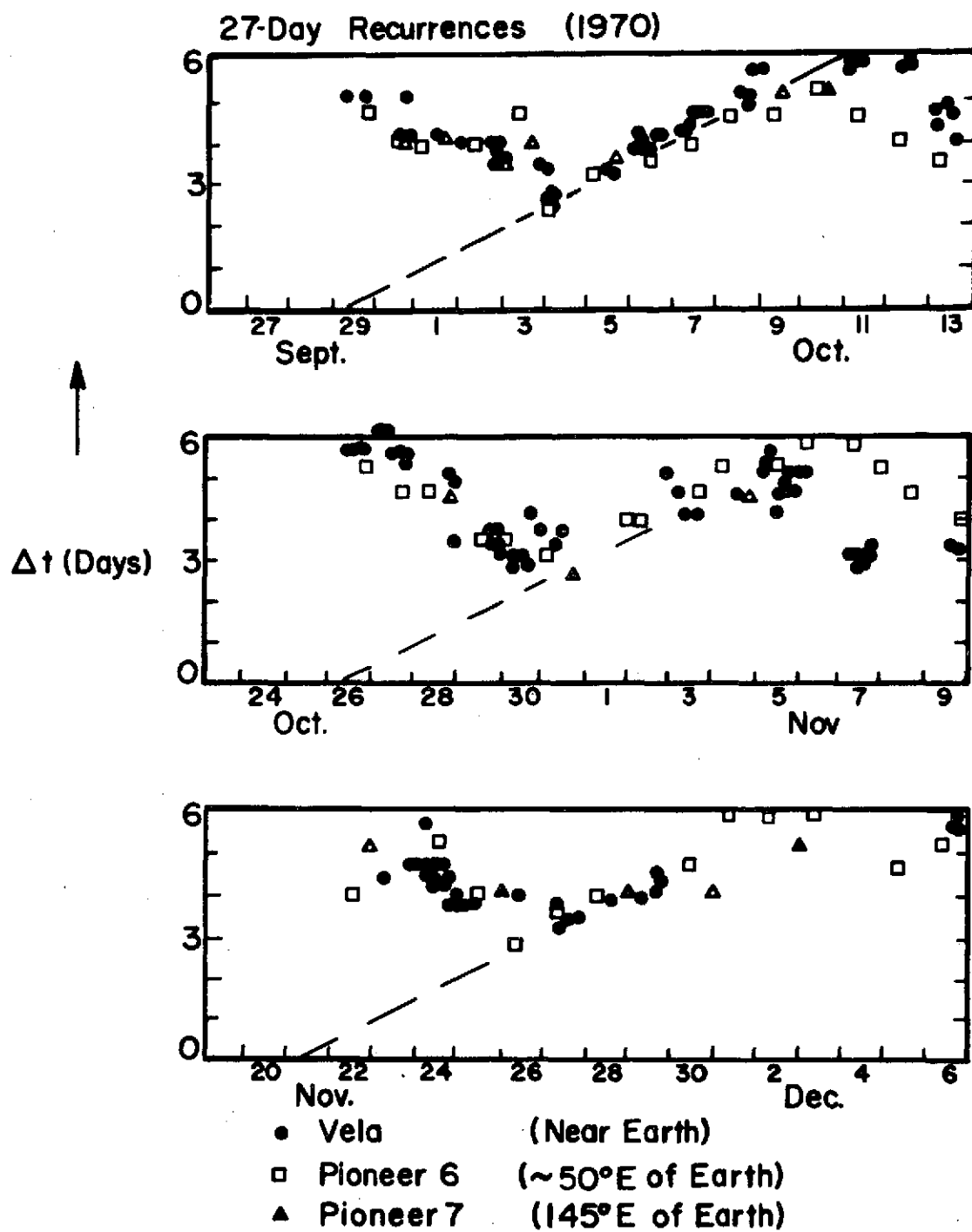
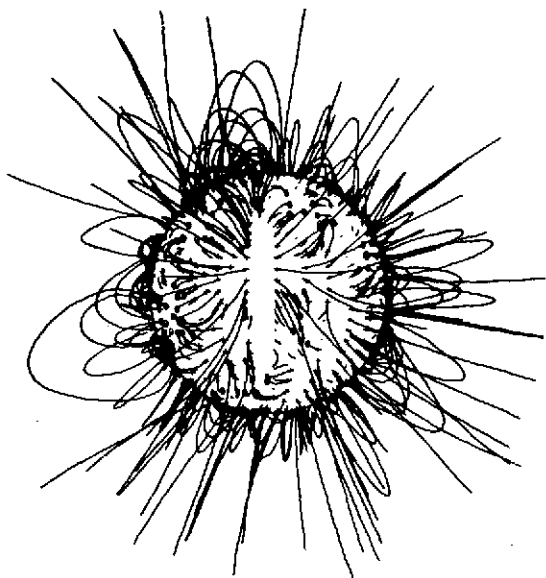
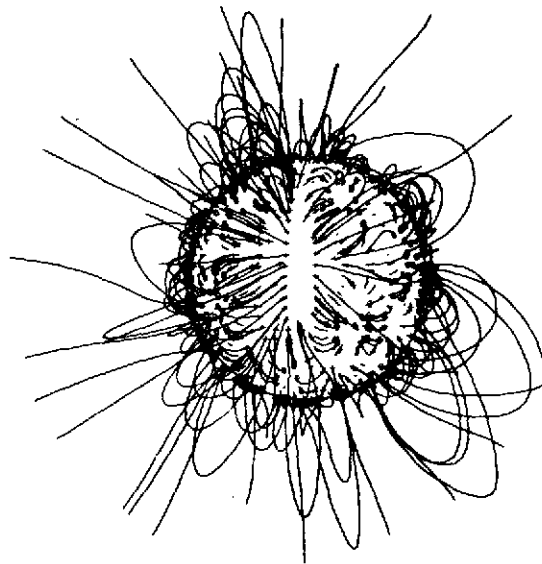


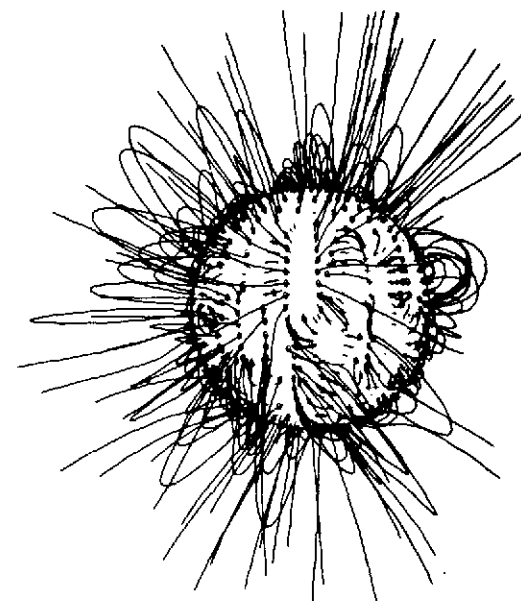
Figure 8



LONGITUDE OF DISK CENTER = 270 DEGREES  
DATE = 1970 NOVEMBER -3.3 CENTRAL DAY = 4 ROT. 1567



LONGITUDE OF DISK CENTER = 270 DEGREES  
DATE = 1970 DECEMBER -6.0 CENTRAL DAY = 1 ROT. 1568



LONGITUDE OF DISK CENTER = 270 DEGREES  
DATE = 1970 DECEMBER 21.3 CENTRAL DAY = 28 ROT. 1569

Figure 9

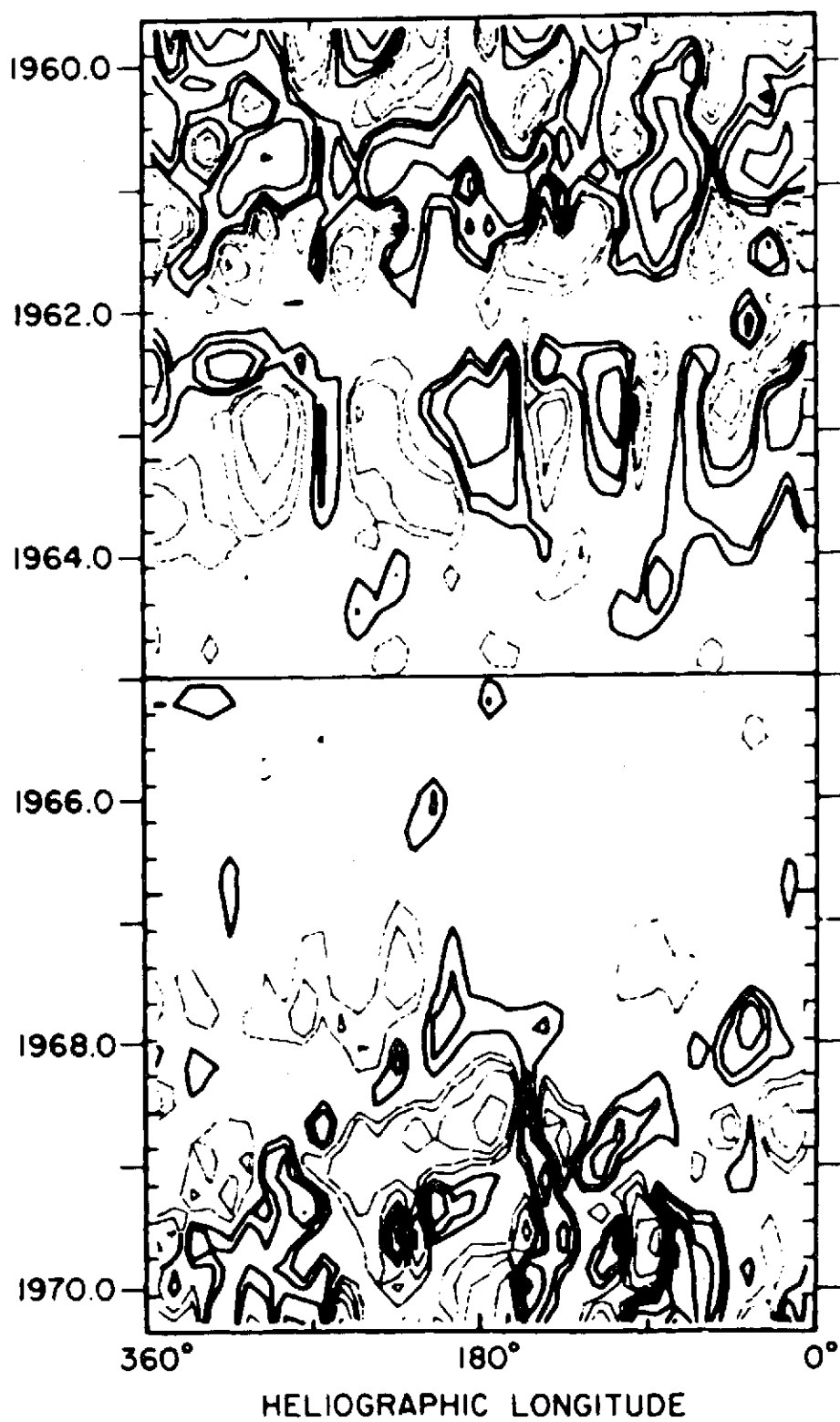


Figure 10